

CRACK IDENTIFICATION IN SLOW ROTATING MACHINERY
USING ON-LINE VIBRATION MEASUREMENTS
AND 3D FINITE ELEMENT ANALYSIS

by

HENNING KEINER

Dipl.-Ing., University of Siegen, Germany, 1997

A THESIS IN PARTIAL FULFILLMENT OF
THE REQUIREMENTS FOR THE DEGREE OF

DOCTOR OF PHILOSOPHY

in

THE FACULTY OF GRADUATE STUDIES

(Department of Mechanical Engineering)

We accept this thesis as conforming
to the required standard

THE UNIVERSITY OF BRITISH COLUMBIA

November 2002

© Henning Keiner, 2002

In presenting this thesis in partial fulfilment of the requirements for an advanced degree at the University of British Columbia, I agree that the Library shall make it freely available for reference and study. I further agree that permission for extensive copying of this thesis for scholarly purposes may be granted by the head of my department or by his or her representatives. It is understood that copying or publication of this thesis for financial gain shall not be allowed without my written permission.

Department of Mechanical Engineering

The University of British Columbia
Vancouver, Canada

Date Dec 6, 2002

ABSTRACT

Vibration monitoring and with it the possibility of on-line machine fault detection and diagnostics have been the focus of maintenance engineering in recent years. In particular, the on-line identification of rotor cracks in turbines, pumps or other rotating machinery holds the potential of great economic benefit due to reduced down-time and loss in production. This work investigates aspects in the development of a crack identification system based on inverse analysis using on-line vibration measurements and 3D Finite Element modeling.

A 3D Finite Element modeling approach, the nodal crack force approach, was developed to model the non-linear crack breathing behaviour of rotor cracks. The approach linearizes the equations of motion around the point of static deflection and solves them in a rotating frame of reference, significantly reducing the computational requirements. Results show good agreement with results from analytical methods and 3D Finite Element transient analysis. The nodal crack force approach was also shown to yield a better model of the crack face opening behaviour for larger cracks than the traditional node de-coupling method.

A scaled-down experimental setup of a pressure washer drum was developed to experimentally investigate the vibrations of a cracked rotor. The experimental setup was used to compare measured vibration signatures from three different crack implementation methods: the bolt removal method, the gap insertion method and the placement of a grown fatigue crack. Results show that the two experimental crack simulation methods yield a comparable vibration response to a grown fatigue crack at significantly lower cost. The bolt removal method was chosen to conduct an experimental parameter study of the influence of crack size and location on the vibration behaviour of the drum. Measured vibration response curves for different crack sizes were clearly distinguishable from one another, and they were matched closely by the Finite Element results, making the identification of crack size and location using an inverse analysis approach feasible.

The inverse analysis problem was solved as a non-linear constraint parameter optimization problem where the objective function consists of a weighted least squares difference between measured and modeled system response. Crack identification for a known crack location yielded results within 10 % of the true crack size. It was also shown that the identified crack size was mostly independent of the chosen weighting function and that simple, global optimization algorithms yield better results than gradient-based methods. Identification of crack size and location was performed using a multi-variable approach and by de-coupling of the optimization parameters making use of the discrete nature of the crack location parameter. While both methods yield satisfactory results, de-coupling led to improved stability and lower computational requirements for a limited number of discrete crack locations. Instead of identifying one final solution point, a confidence measure was introduced, supplying information about the objective function around the global minimum. This led to an improved solution for practical purposes.

TABLE OF CONTENTS

Abstract	ii
Table of Contents	iv
List of Tables	vii
List of Figures	viii
List of Symbols and Abbreviations	x
Acknowledgments	xii
CHAPTER 1 – Introduction	1
CHAPTER 2 – Background and literature review	7
2.1 Modeling the vibration of a cracked shaft	7
2.2 Cracked shaft indicators	11
2.3 Experimental studies	12
2.4 Cracked shaft incidents in the field	16
2.5 The inverse problem of crack identification in solids	19
CHAPTER 3 – Vibration modeling of a cracked rotor	22
3.1 Analytical solution	23
3.2 3D transient FE analysis	24
3.3 3D nodal crack force approach	26
3.3.1 Linearization of the 3D FE equations	26
3.3.2 Solving the FE equations in a rotating coordinate system	29
3.4 Verification of the nodal crack force approach	32
3.4.1 Example 1 - Short cantilever shaft	33
3.4.2 Example 2 - Laval rotor	37
CHAPTER 4 – 3D Finite Element model of a cracked drum	41
4.1 3D FE model of a scaled-down pressure washer drum	41
4.2 FE analysis procedure	45

4.2.1	FE analysis using the nodal crack force approach	45
4.2.2	FE analysis with crack breathing controlled by nominal stress distribution	48
4.2.3	FE analysis using contact elements at the crack faces	48
4.3	FE results	49
CHAPTER 5 – Experiment		55
5.1	Experimental setup	55
5.1.1	Scaled-down pressure washer drum test specimen	55
5.1.2	Vibration sensors, signal conditioning and data acquisition	57
5.1.3	Experimental data analysis program	61
5.2	Experimental crack modeling	63
5.2.1	Bolt removal method	63
5.2.2	Gap insertion method	66
5.2.3	Real fatigue crack	66
5.3	Experimental procedure	70
5.4	Results and discussion	71
CHAPTER 6 – Crack identification using inverse analysis		83
6.1	The inverse problem of crack identification	83
6.2	Identification of crack size for a known crack location	84
6.3	Identification of crack size and location	93
6.3.1	Multi-variable optimization	93
6.3.2	De-coupling of crack size and location	97
CHAPTER 7 – Conclusions		101
7.1	Summary of results	101
7.2	Outlook	106
BIBLIOGRAPHY		108

APPENDIX	118
A Properties of the FE drum model	119
A.1 Element and material properties	119
A.2 Measured and modeled bearing stiffness	120
A.3 Simulated crack breathing using contact elements	121
B Experiment	125
B.1 Technical drawings of experimental setup	125
B.2 Similarity analysis for the scaled-down pressure washer drum	134
B.3 Specifications of sensors and DAQ equipment	135
B.4 Technical drawing of gap insertion specimen	136
B.5 Technical drawings of fatigue crack specimen	137
B.6 Recorded vibration signatures for crack locations 1-5	139
C Inverse analysis	144
C.1 Matlab function Powell1D	144
C.2 Inverse analysis results for a known crack location	146
C.3 Matlab function Powell2D	151
C.4 Multi-variable inverse analysis results	153

LIST OF TABLES

Table 3.1	Comparison of analytical and FE results - example 1	34
Table 3.2	Comparison of analytical and FE results - example 2	38
Table 4.1	Comparison of natural frequency and static deflection between the 3D FE drum model and experimental measurements	44
Table 5.1	Investigated crack sizes using the bolt removal method	65
Table 5.2	Measured peak to peak horizontal and maximum vertical deflection	72
Table 6.1	Objective function weighting factors	86
Table 6.2	Performance comparison of single-variable optimization techniques	88
Table 6.3	Performance comparison of multi-variable optimization techniques	94

LIST OF FIGURES

Figure 1.1	Schematic view of a crack identification system using on-line vibration measurements	5
Figure 3.1	Varying cracked shaft stiffness	22
Figure 3.2	2 DOF model of a cracked shaft	24
Figure 3.3	3D FE model of a cracked shaft segment	25
Figure 3.4	Superposition principle of the nodal crack force approach	27
Figure 3.5	Kinematics of a lumped mass point in a rotating frame of reference	29
Figure 3.6	3D FE model of a cracked cantilever shaft	33
Figure 3.7	Quasi-static vibration of a cracked cantilever shaft	35
Figure 3.8	Orbit of a cracked cantilever shaft	36
Figure 3.9	FE model of a cracked Laval rotor	37
Figure 3.10	Quasi-static vibration of a cracked Laval rotor	39
Figure 3.11	Vibration amplitude of a cracked Laval rotor	39
Figure 3.12	Orbit of a cracked Laval rotor	40
Figure 4.1	3D FE model of a pressure washer drum	42
Figure 4.2	Applied concentrated nodal forces on the drum shell	43
Figure 4.3	Spring element configuration at bearing centerline	43
Figure 4.4	Crack parameters L and α for 3D FE drum model	45
Figure 4.5	Nodal crack force approach flow chart	46
Figure 4.6	Nodal coupling and nodal crack forces along the crack face	47
Figure 4.7	Shift of neutral axis for 3D FE model using contact elements	49
Figure 4.8	Simulated vibration results using the nodal crack force approach	51
Figure 4.9	Simulated vibration results using contact elements	52
Figure 4.10	Simulated vibration results using nodal de-coupling approach	53
Figure 4.11	Simulated crack opening using contact elements	54

Figure 5.1	Experimental test specimen	56
Figure 5.2	Flow chart of data acquisition process	60
Figure 5.3	Flow chart of experimental data analysis program	62
Figure 5.4	Crack at inner hub using the bolt removal method	64
Figure 5.5	Definition of crack parameters using the bolt removal method	65
Figure 5.6	Investigated crack sizes using the gap insertion method	66
Figure 5.7	Growing a fatigue crack into the inner hub specimen	68
Figure 5.8	Fatigue crack sizes at the inner hub	69
Figure 5.9	Fastening plate used to establish reference measurements	70
Figure 5.10	Mean values of vibration signals using the bolt removal method	73
Figure 5.11	Mean values of vibration signals using the gap insertion method	74
Figure 5.12	Mean values of vibration signals using a real fatigue crack	75
Figure 5.13	Measured Fourier coefficients using the bolt removal method	79
Figure 5.14	Measured Fourier coefficients using the gap insertion method	80
Figure 5.15	Measured Fourier coefficients using a real fatigue crack	81
Figure 5.16	Comparison of 1 st and 2 nd Fourier coefficients for different crack simulation methods	82
Figure 6.1	Flow chart of optimization procedure	87
Figure 6.2	Inverse analysis results for the identification of the crack size at a known crack location	89
Figure 6.3	Comparison of experimental and identified vibration signatures	90
Figure 6.4	Objective function for various true crack sizes	91
Figure 6.5	Influence of weighting functions on inverse analysis results	92
Figure 6.6	2D objective function for specific crack parameters	95
Figure 6.7	Inverse analysis results using multi-variable optimization techniques	96
Figure 6.8	Inverse analysis results using crack parameter de-coupling approach	99
Figure 7.1	Comparison of FE and experimental results	104

LIST OF SYMBOLS AND ABBREVIATIONS

C	damping matrix
<i>c</i>	damping constant
<i>D</i>	diameter
<i>E</i>	modulus of elasticity
<i>I</i>	second moment of area
<i>F</i>	force
<i>F_C</i>	nodal crack force
<i>F_N</i>	nodal coupling force
<i>j, k</i>	indices
K	stiffness matrix
<i>k_r</i>	radial stiffness
<i>k_φ, k_ψ</i>	angular stiffness
<i>k_{xx}, k_{yy}</i>	directional stiffness components
<i>k_{xy}, k_{yx}</i>	cross-coupling stiffness components
<i>L</i>	crack location parameter
<i>L_{true}</i>	true crack location parameter
<i>l</i>	rotor length
M	mass matrix
<i>m</i>	point mass
<i>N_f</i>	number of function evaluations
<i>n</i>	node number
<i>p</i>	number of considered Fourier coefficients
<i>r, r₀</i>	location vector, original location vector
<i>t</i>	time
<i>u, u_x, u_y</i>	displacement vector, directional components
<i>X</i>	horizontal deflection Fourier coefficient
<i>Y</i>	vertical deflection Fourier coefficient
<i>x, y, z</i>	Cartesian coordinates
<i>x₀</i>	start point in optimization procedure
Δx	differential horizontal deflection
Δy	differential vertical deflection
α	crack size angle

α_{true}	true crack size angle
ε	displacement in rotating coordinates
ϕ	objective function
λ	confidence value
ν	Poisson's ratio
Ω	rotational velocity
Ωt	angle of rotation
ω_n	natural frequency
ψ	objective function
ξ, η, z	rotating coordinates
ζ	modal damping factor
BEM	Boundary Element Method
BRM	bolt removal method
CBM	condition based maintenance
CE	contact element approach
DAQ	data acquisition
DOF	degree of freedom
EDA	experimental data analysis
FC	fatigue crack
FE	Finite Element
FEA	Finite Element analysis
FEM	Finite Element Method
GIM	gap insertion method
GSS	golden section search algorithm
LSQ	least squares trust region algorithm
MTS	material testing system
NCF	nodal crack force approach
NDC	node de-coupling approach
SIF	stress intensity factor
SQP	sequential programming algorithm

ACKNOWLEDGMENTS

A Ph.D. thesis is never the result of just one person but a product of the input of many.

My sincerest gratitude goes to my supervisor, Dr. Mohamed S. Gadala, for his academic, financial and personal support. His invaluable guidance and encouragement have been a corner stone of my experience at UBC.

Many thanks to Dr. Gary S. Schajer for the insightful discussions, the lending of research equipment and for his invaluable advice in particular in the practical matters of engineering.

Thanks to Trevor Tang for his help in conducting the Finite Element simulation, experimental work and the development of the data acquisition program.

Thanks to Mareike Rassing for proofreading and to Willem Atsma for helping whenever help was needed.

Special thanks also to the staff and technicians of the Department of Mechanical Engineering without whose help there would not have been an experimental setup or testing equipment.

The work was supported in part by Tristar Industries in Delta, British Columbia.

*Alas, of high Philosophy,
Law's Mystery, and Medicine,
And, to my grief, Theology,
I've toiled the mastery to win –
And now, poor fool, for all my lore,
I stand no wiser than before.*

Goethe's Faust

CHAPTER 1

INTRODUCTION

Today, much of the installed large-scale machinery in industry has been in operation for more than 25-30 years and is reaching the end of its design life. At the same time, production facilities are competing to become more and more efficient and the pressure for critical machinery to be available twenty-four hours a day, seven days a week and to reduce mean time between failure has increased dramatically. Thus, as the procurement cost for systems and equipment has increased, it is often eclipsed by operating and support cost in part due to failures and the necessary subsequent repairs but even more by the resulting loss in production. A major cause for downtime and repairs on large rotating machinery, such as turbines, generators, drums and rolls, are mechanical faults, especially unbalance, misalignment, shaft bow, bearing faults and cracks [1]. Cracks, in particular, occur often at welds or in areas of stress concentrations. If they remain undetected, they can develop into large cracks that can lead to severe damage of machine components or even catastrophic failure. High cycle fatigue is the predominant crack growth mechanism in rotating machinery due to the cyclic nature of the applied stresses. For instance, rotors operating at a comparably low rotational speed of 20 rpm will easily see ten million load cycles per year, if they are operated continuously. Most high speed rotating machinery operates at rotational speeds above 1000 rpm, experiencing many times that load. Other influences contributing to crack growth in rotating machinery are thermal stresses and stress corrosion cracking for rotors operating in corrosive environments [2,3].

All this has led to an increased interest in maintenance technology and automated machine condition monitoring. Maintenance programs in industry and other organizations range from a "run to failure" philosophy over preventive maintenance to condition-based and predictive maintenance [4-6]. Effective and efficient maintenance programs usually include all approaches and the optimal choice is highly application specific. While the "run to failure" philosophy is common and sufficient for many inexpensive, non-critical and easy to replace components, it is clearly unsuitable for mission-critical systems and

components that are essential to safety, expensive, cannot be replaced easily, or where replacement requires significant downtime.

Preventive maintenance programs consist of regularly scheduled service and repair intervals conducted by the machine operator or maintenance personnel. The key feature is that the machine's condition is actually not evaluated, but maintenance is conducted regardless in order to prevent any deterioration of the machine's condition. This type of maintenance program is most suited for inexpensive, easy to do maintenance tasks that do not significantly interrupt machine operation and where service intervals are highly regular and well established. Predictive maintenance, often referred to as condition based maintenance (CBM) or machine health monitoring, has received the most attention in recent years. It has been shown that CBM can be used to extend the safe life of older machinery significantly [7,8]. The market for machine condition monitoring has been growing by more than 20 % over the last five years and is expected to grow even stronger in the near future [9-11]. CBM is based on off- or on-line monitoring of a machine's condition and scheduling of maintenance and repair intervals as needed. Clearly, the goal of predictive maintenance is to minimize the effect on the machine's operation, hence it is particularly suited for mission-critical machinery with high cost in downtime.

CBM can be achieved by inspection and expertise of maintenance personnel, probabilistic feature-based fault detection systems, and fault detection systems based on physical modeling [12]. In probabilistic feature-based fault detection systems sensory data from healthy and faulty machinery is collected and statistically analyzed for fault indicators. The identification of a certain statistical measure indicating a machine fault is called "feature extraction". Subsequently, recorded data of monitored machines is analyzed for these features in order to detect a fault. Feature extraction has been used successfully in many industrial applications, particularly in the early detection of developing faults [7,13,14]. However, because of the statistical and empirical nature of the method, it is difficult to draw conclusions regarding fault parameters or fault prediction from its results. Furthermore, it requires an extensive amount of

experimentally collected data for the feature extraction process and is difficult to extend to different types of machinery due to the lack of physical modeling.

CBM systems based on physical modeling predict the response of a damaged machine component under service load. If such a response is detected in the sensory data, the modeled fault is assumed to exist. In general, this approach supplies a better understanding of the exact cause of the problem compared to the previous condition monitoring methods. If a sufficiently accurate model is available, it is generally easier to identify fault parameters and estimate the severity and remaining safe life of the damaged component. However, application dependent, physical modeling can be difficult and sometimes does not yield the required accuracy, or results are significantly influenced by ambient noise.

Some of the technologies used in CBM systems to detect cracks and other faults in rotating machinery are visual inspection, dye-penetrant, ultrasound and x-ray [15]. These methods are considered off-line techniques in that it is generally necessary to stop operation for condition assessment to occur. The main advantage of these methods is that they are well established and reliable. In contrast, on-line techniques, such as vibration monitoring, acoustic emission, eddy-current monitoring, infrared photography and lubricant analysis, attempt to assess a machine's condition while the machine is in operation. This approach significantly reduces the number of scheduled maintenance intervals and resulting downtime. Among these technologies, vibration monitoring and analysis has been a preferred method due to its general applicability to a wide range of machinery [1,16]. The principles of vibration monitoring are straight forward. An increase in overall vibration levels almost always accompanies deterioration in running conditions [17]. Dominating vibration frequencies are often used to determine the cause of the vibration [18].

Common industry practices in vibration monitoring are route based systems in which maintenance technicians will take sample vibration readings from handheld or permanently installed vibration sensors for analysis in computerized handheld or desktop

style vibration analysis systems. There is a range of vibration analysis equipment on the market offering a variety of analysis techniques [19,20]. However, the difficult part lies in interpreting the signal and drawing the correct conclusion with regard to the type and severity of a possible present or future malfunction. Therefore, for more expensive, mission-critical machine systems, the trend goes towards permanently installed, multi-sensor, continuous monitoring systems with diagnostic capability, interpreting recorded vibration signals and providing machine operators directly with information about developing machine faults [21,22]. Such machine health monitoring and diagnostics systems are often based on hierarchical control systems using a knowledge base or expert system approach. A top level controller may determine the type of fault while a specialized subsystem will investigate the severity in more detail. However, with respect to the detection of rotor cracks, current systems are simply warning to the presence of a crack without providing additional information about its size and location. Furthermore, most work has been confined to specific applications and no general approach to on-line identification of crack size and location and subsequent monitoring has been developed.

A system which, in principle, is capable of identifying a crack in a rotor by size and location based on vibration measurements is shown in Figure 1.1. Vibration transducers measure the vibration of a rotor and the signal is recorded over an appropriate period of time. The vibration signal is then analyzed and averaged to remove random noise. Simultaneously, an analytical or numerical model is used to predict the vibration of the rotor. As long as the measured vibration matches the predicted vibration from the model, no flaw is assumed to exist in the structure. If a discrepancy between measured and predicted vibration is discovered, a crack of assumed size and location is introduced into the model. The vibration of the rotor due to the crack is analyzed and compared to the measured vibration. By use of optimization algorithms the crack parameters are altered until the predicted vibration matches the measured vibration. At this stage, a crack, defined by location and size through the current crack parameters, is assumed to exist. Subsequently, the crack growth can be monitored by re-evaluating the crack parameters throughout continuous operation of the rotor.

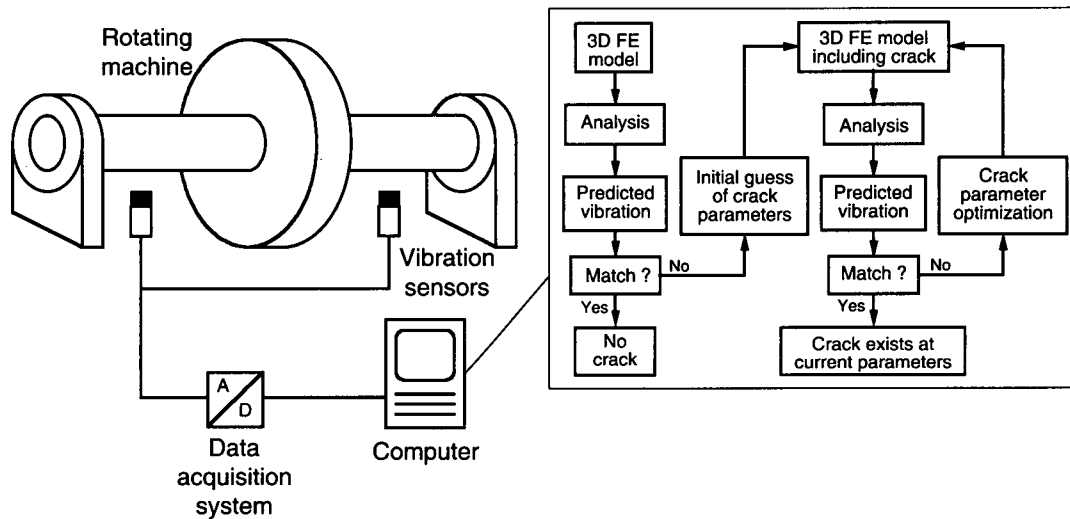


Figure 1.1: Schematic view of a crack identification system using on-line vibration measurements.

Ideally, the system should provide the operator with the following information and benefits:

- It should identify a crack, i.e., specify its approximate location and size.
- It should provide information on the time required for the crack to reach a critical size. This may lead to extension of the time between scheduled off-line inspections.
- It should be part of a general machine condition monitoring system and provide the machine operator with continuous information about the machine's condition. Specifically, it should be able to distinguish a crack from other sources of malfunctioning.
- It should be applicable to a variety of types of machinery, not just to one specific application.

In this research three aspects necessary for the development of the described crack identification and monitoring systems will be investigated.

1. The importance of an accurate model to predict the vibration of a rotor, particularly the vibration due to a crack, is obvious. In practice, often a vibration signature of the uncracked rotor is recorded and then subtracted from all subsequent measurements,

isolating the effect of a developing crack [2]. Much work has been done to study the vibration of a rotor with a cracked shaft. Until now, however, no general approach suitable for modeling the vibration of a cracked structure of arbitrary geometry has been developed. Therefore, a first step is the extension of existing methods to model the vibration of a cracked rotor to an approach which will be generally applicable to three-dimensional (3D) structures and does not underlie the common assumption of a thin rotor with distributed lumped masses along its axis.

2. To verify the developed model, an experimental study will be conducted. The experiment should provide feedback and improvement to the quality of the developed model. For this, the experiment must be designed using specimens which do not resemble the commonly used Laval rotor (thin massless shaft with a heavy disk at mid span) but rather the dynamic characteristics of a true, possible application. Furthermore, the influence of not just the presence but also location and size of a crack, is to be investigated. This should yield a better understanding to which dynamic quantities will be of importance when identifying and monitoring a crack in a rotating machine.
3. Finally, the results of the modeling process and the experiments will be tied together in the attempt to identify a crack in a specimen, i.e., determining its approximate size and location. Here the main task is finding an optimal approach to solve this inverse problem and answering the question if crack identification using vibration measurement is feasible for real applications.

CHAPTER 2

BACKGROUND AND LITERATURE REVIEW

2.1 Modeling the vibration of a cracked shaft

The behaviour of a rotating shaft containing a transverse crack was first investigated in the late 1960s by Dimarogonas [23] and Pafelias [24] as a large steam turbine at General Electric was in suspicion of containing such a crack. A result of these efforts was the introduction of the bending stiffness description of a cracked rotor. They determined the reduced stiffness in bending through compliance measurements and developed a supervisory instrument designed to give an early crack warning based on vibration measurements. Gasch [25] and Henry and Okah-Avae [26] described the non-linear equations of motion for a Laval rotor in a body-fixed coordinate system. They modeled the non-linear mechanism as a change in natural frequency of the rotor and solved the equations using an analogue computer. They also showed that the equations of motion can be greatly simplified for heavy rotors operating below their critical speed and where the dynamic response depends largely on the effects of gravity. Utilizing these assumptions Mayes and Davies [27,28] transferred the equations of motion to a stationary coordinate system and replaced the non-linear behaviour of the crack by a system of linear differential equations with time-varying coefficients. Assuming that even for large cracks the change in stiffness is small and sufficient damping to prevent instability exists, they expanded the time-varying term into a harmonic power series and, neglecting second order terms, transformed the non-linear problem into a linear vibration problem with harmonic excitation.

Different models were developed by several researchers in order to describe the crack breathing mechanism and the reduced bending stiffness of a cracked shaft.

Grabowski [29] suggested to model the reduced stiffness by a slot of equal depth and length along the shaft axis. The shaft stiffness in this region was replaced by the stiffness of the remaining cross-section plus the part of the cracked cross-section which remained above the centerline of the crack to simulate the crack breathing mechanism. Mayes and

Davies [27] used a similar approach but determined the length of the reduced cross-section using Green's function and experimental results from static compliance measurements of a circular beam containing a saw cut. They simulated the crack breathing effect by a control function. Gasch et al. [30] compared the models by Mayes and Davies, a simple hinge model and their own model for a hollow shaft. They concluded that the hinge model yields good approximations for small crack depths (crack opening angle $< 30^\circ$). For larger cracks the smooth control function of Mayes and Davies yielded better results.

Dimarogonas and Papadopolous [31] developed an analytical solution for the reduced bending stiffness utilizing the Griffith energy principle. They applied the solution of a stress intensity factor for an edge crack in two dimensions and integrated it over the width of the shaft at the crack line. With this method they were able to compute the additional crack compliance of a beam for six degrees of freedom (DOF) yielding a full additional compliance matrix for a cracked shaft segment. Together with other researchers [32-37], Dimarogonas studied the dynamic response and identified vibration coupling effects for longitudinal and bending vibration as well as bending and torsional vibration. Furthermore, they investigated the frequency spectrum associated with a cracked rotor and reported regions of instability at harmonics of the rotational speed ($3/2\text{rev.}$, $5/2\text{rev.}$, $7/2\text{rev.}$, etc.) beyond the known instabilities from the solution of the linearized equations ($1/\text{rev.}$, $2/\text{rev.}$, $3/\text{rev.}$, etc.) This was confirmed by Changhe et al. [38].

Bently and Muszynska [2,39,40] suggested the monitoring of amplitude and phase angle as a means to crack detection. They specifically refer to a change in $1/\text{rev.}$ amplitude coupled with an increase of $2/\text{rev.}$ amplitude as an indicator for a crack in a rotor system. They developed a crack detection system gathering data from coast down as well as on-line operation using displacement eddy-current proximity probes. Imam et al. [41] developed a crack detection system based on an analytical model predicting a strong increase in $2/\text{rev.}$ vibration response. They derived a special beam element based on the reduced bending stiffness of the cracked region of the shaft by modeling the cracked

segment using static 3D solid Finite Element analysis (FEA). Then, utilizing a beam Finite Element (FE) code, they computed the vibration response of a thin circular shaft and compared it with the measured response of a cracked test specimen. Liao and Gasch [42] analyzed the 1/rev., 2/rev., and 3/rev. vibration response, breaking it up into its forward and backward components. They were particularly interested in the change of the 1/rev. backward component as the clearest indicator for a crack. Gasch [43] and Gasch et al. [30] further investigated the stability of a cracked Laval rotor and a hollow shaft using a smooth breathing crack model and the linearization method by Mayes and Davies [27,28]. In particular, Gasch computed the shape of shaft orbits for subcritical rotational speeds.

Other researchers [44-50] have utilized slightly different techniques achieving similar results. It is important to note that most models used were strongly based on analytical work with FEA only contributing to local effects when determining the reduced stiffness of the cracked shaft segment. For modeling of the entire rotor response 3D beam elements were used exclusively. The most advanced FE modeling was performed by Dirr and Schmalhorst [51-54]. They computed the reduced stiffness of a cracked beam element by 3D FEA at various angles of rotation and compared it to the analytical models of Dimarogonas [31] and Grabowski [29]. They concluded that Grabowski's model was accurate for relatively shallow cracks only, whereas Dimarogonas' model proved too flexible over the entire range of crack sizes. Schmalhorst [52] verified his observations through extensive compliance measurements showing good agreement with the FE results and also investigated the beachmarks during crack propagation on a cylindrical shaft. He computed the non-linear vibration response of a 48 DOF FE beam model in a transient analysis using direct time-integration and showed good agreement with his experimental results. Similar observations have been made by Keiner and Gadala [55] based on crack compliance measurements by Bush [56].

More recent studies have focused on the modal characteristics and stability regions of cracked rotors [57-63]. Hamidi et al. [55] calculated the mode shapes and natural frequencies as a function of crack depth and location. They reported that change in the

second natural frequency was most sensitive to the crack depth, whereas change in the third natural frequency could be attributed to the crack location. Ishida and Hirokawa [58] computed the resonance curves of a cracked Laval rotor and confirmed the results experimentally. In particular, they confirmed the existence of second and third order harmonic resonances. Ishida et al. [59] also studied the change in resonance due to a change in the unbalance phase angle, and Meng and Gasch [60], Nelson and Nataraj [47] and Wu and Huang [62] included the bearing influence on the stability of a cracked rotor.

The shape of the orbit of a cracked rotor has been computed by Meng and Hahn [64], Schmied and Krämer [44], and Chan and Lai [65] using the analytical Laval rotor model. Tsai and Wang [66,67] and Keiner and Gadala [68] computed orbits using the transfer matrix method and 3D FEA, respectively. Qualitative results for orbit shapes of all studies show good agreement. All studies concluded that the shape of the orbit is highly influenced by the presence of a crack and hence serves as an excellent tool to crack detection, an opinion also stated by Bently and Muszynska [2]. Lee et al. [69] derived the necessary conditions for opening and closing of a crack from the non-linear equations of motion and the associated bending moment.

Several researchers have studied coupling of longitudinal and lateral vibration in a cracked shaft. Papadopoulos and Dimarogonas [35] have formulated the coupling terms of the crack compliance matrix and computed the free and forced vibration response. Gounaris and Papadopoulos [61] have used these results for crack detection purposes by exciting a cracked shaft in the axial direction while observing the lateral response. Similar methods were employed by Darpe et al. [81] and Takahashi [61]. Investigations into the non-linearity resulting from the crack breathing mechanism have been performed by Lee et al. [69] and Zheng et al. [71] who analyzed the fully non-linear equations focusing on the behaviour of bifurcation and chaos.

Studies of a shaft containing more than one crack were performed by Tsai and Wang [66] and Sekhar [72] who investigated the influence of one crack over the other on natural

frequencies and mode shapes. Sekhar and Balaji Prasad [73,74] and Ichimonji and Watanabe [75] investigated the dynamics of a rotor considering a slant crack. Nink and Stölben [76] researched the vibration of vertically oriented shaft containing a crack. Mohiuddin and Khulief [77] studied the modal characteristics in cracked conical rotors, and Parhi and Behera [78] performed a vibration analysis of a cracked shaft in viscous media. Finally, extensive reviews of the literature on cracked shafts have been provided by Wauer [79] and Dimarogonas [80].

2.2 Cracked shaft indicators

Results from vibration analysis studies on cracked shafts have lead to various approaches for the detection and identification of rotor cracks. Several researchers suggested a slight decrease and splitting of the first natural frequency to be an indicator for the reduced stiffness due to a fatigue crack [2,40,64,81,82]. Another indicator is an additional response peak at half the natural frequency, thus Sekhar and Prabhu [83] propose to monitor the response at these frequencies during start-up. Other authors suggest monitoring of 1/rev., 2/rev. and 3/rev. vibration amplitude [39-41,58,62,76,84-88]. Here, the 2/rev. amplitude in particular is regarded by many authors as a key indicator for a shaft crack. Imam et al. [41] developed a data recording scheme which averages the measured data at equal points in angle of rotation over many revolutions. The method proved particularly useful to eliminate noise from the vibration signal and enhance key vibration components. Bently and Muszynska [2,39,89] also suggest to monitor orbit shapes, polar plots and spectrum cascade plots for irregularities. In particular a strongly elliptical orbit for running speeds close to the first natural frequency and a double loop orbit for rotational speeds close to half of the first natural frequency are considered indicators for a crack. Additionally, they suggest to monitor the phase change in the vibration signal, which has also been suggested by other researchers [27,84]. All of these methods, however, are relying on the comparison of vibration components to an initial reference vibration signature which must be previously obtained from the undamaged rotor. At the very least, the analyzed data is taken from trend readings, in which not the absolute vibration reading is analyzed but rather the change over time [2,41,76,85,87].

Various studies have focused on using the difference in mode shape to identify a crack in a structure [48,90-92]. Dimarogonas and Papadopoulos [34] and Lees and Friswell [81] suggest the detection of cracks through the cross-coupling phenomena and through external excitation, respectively. Seibolt and Weinert [93] have used an Extended Kalman Filter to identify shaft cracks, while Nandwana and Maiti [94,95] employed a technique evaluating the stiffness as a function of the crack parameters and measured natural frequencies. A similar technique has been employed by Wu and Huang [62]. Bispectral analysis, a higher order statistical measure, to be used for crack detection in a beam was investigated by Rivola and White [96]. However, all these methods have only been analyzed theoretically and in conjunction with very simple beam models.

2.3 Experimental studies

Experimental investigations of cracked rotors in the literature are not as common as theoretical work in this area. The main reason appears to be the great effort involved in placing a fatigue crack of known size at a specific location. However, some experimental studies have been reported and various valuable conclusions can be drawn from them. Mayes and Davies [27,28] were the first to perform experiments using a cracked rotor to complement their analytical work in this area. They used a flexible shaft with a massive disk at mid span (Laval rotor) running in rigid bearings. Accelerometers were mounted on the bearings and inductive proximity transducers were located at rotor mid span. They took vibration measurements during rundown from supercritical operation. Initially, compliance and vibration of the uncracked shaft were recorded. A crack was introduced by placing a saw cut (1 mm) close to the shaft mid span and a fatigue crack was propagated in a three point bending fatigue testing machine. The crack propagation rate was verified using electrical resistance measurements across the crack faces. The vibration of the cracked shaft was measured for a balanced, unbalanced in-phase and unbalanced out-of-phase rotor. The exact crack front throughout the experiment was later verified by failing the shaft and observing the beachmarks. Mayes and Davies primarily investigated the amplitude of first and second harmonic and the influence of the unbalance phase angle. They were able to show the double peak in the first harmonic as a result of the anisotropic shaft stiffness due to the crack. They also showed an increase in

amplitude of the second harmonic for increasing crack depth. Vibration levels were generally higher when the unbalance was in phase with the crack. They also noted that it was difficult to completely balance the rotor and that it needed re-balancing after every crack extension. Similar studies have been performed by other researchers yielding comparable results [32,53,62,69].

Fonte and Freitas [97] investigated the crack front shape for a shaft under reverse bending with steady state torsion. Imam et al. [41] conducted experiments to validate their developed crack detection approach using a unique four-bearing-three-disks test system which simulated a typical power generating turbine setup. Proximity probes and accelerometers were used to measure lateral and longitudinal vibration, and a 1/rev. reference signal was taken by an optical sensor. As detection criterion, Imam et al. developed the Histogram Signature Analysis Approach which essentially averages the vibration data in the time domain and subtracts the averaged "baseline signature" of the uncracked shaft. Subsequently, the data is analyzed in the frequency domain. The result is a very high peak for the second harmonic indicating the presence of a crack. With this technique, Imam et al. reported the detection of cracks as small as 1 to 2 % of the shaft diameter.

Dirr et al. [87] and Rothkegel [85] fatigued a shaft from a small starter notch and plotted the increase in 1/rev., 2/rev. and 3/rev. vibration components versus the total number of revolutions. They showed that while absolute levels of vibration will indicate the existence of a crack of approximately 15 % of the diameter, trending the data, i.e., subtraction of a previously established reference baseline, will yield a much clearer picture and allows crack identification as early as 5 % of the shaft diameter. Therefore, Dirr et al. emphasize the advantages of the method by Imam [41] for crack detection. Muszynska et al. [98] measured the torsional vibration associated with a rotor of dissimilar moments of inertia and discovered that very high, very sharp peaks of vibration occur at harmonics of the rotational speed even though no varying torque was applied to the shaft. This led to the conclusion that combined monitoring of lateral and torsional

vibration could yield an improved diagnostic tool for cracked shafts which show a similar behaviour as a shaft with dissimilar moments of inertia.

From these studies it becomes clear that growing a crack of specific size at a predetermined location in a structure can pose great difficulties in an experimental setup. Saw cuts as starter notches have been used by several researchers [69,84,87,93,97]. Other researchers [53,85,91] used electro-erosive techniques in order to minimize the notch width. An alternative technique was described by Lee [69] who placed a 1 mm notch into a shaft of 13 mm in diameter, grew the crack in a fatigue testing rig and subsequently machined the shaft to a diameter of 10 mm, removing the original starter notch.

The second great difficulty lies in determining the exact size of the propagating crack at the time of the test. For this, a variety of techniques have been reported in the literature. Imam et al. [41] used dye-penetrant and ultrasonic inspection to confirm the existence and the size of a crack in their rotor. Schmalhorst [52] used electric potential drop measurements over the cracked surface. He concluded crack size and shape of the crack front from previous calibration measurements using slotted specimens. A similar method was employed by Mayes and Davies [28]. A common approach used by many researchers [52,53,85,93] is the comparison of beachmarks on the failed cross-section with the load cycle history. In this approach, a beachmark pattern is produced along the current crack front during fatigue crack propagation by altering the applied stress significantly for a limited number of cycles. Usually the applied stress intensity is reduced, such that crack propagation occurs more slowly than during regular applied load, and the changed crack propagation mechanism creates a visually distinct region along the crack front. Later, when the specimen has completely failed, a comparison with the load cycle history provides information about the exact location of the crack front at specific times during the test. However, beachmarking requires a good understanding about the applied stress intensity factor along the crack front and the fatigue crack propagation mechanism of the material. In addition many materials do not create beachmark patterns throughout fatigue crack propagation [99].

Mühlenfeld [84] reported the use of fiber optic sensors to determine the size of a crack in a shaft. Strands of fibers carrying an optical signal were glued on the outside shaft surface. The propagating crack would rupture the fiber and interrupt the signal, thus yielding information on how far the crack had propagated at the shaft surface. A simpler approach had been employed by Fonte and Freitas [97] who observed the growing crack length at the shaft surface using an optical microscope. Alternatively, Lee et al. [69] simply failed every specimen after each test and observed the front line of the fatigue crack.

While each of these methods has its individual advantages and disadvantages, they all share the fact that growing a fatigue crack of certain size at a specific location is generally a lengthy and expensive process and requires extensive testing equipment. Additionally, the methods of evaluating the crack size are sometimes unreliable. Dirr et al. [87] reported that cracks occurred in some specimens at other locations than the implemented starter notches. Furthermore, a specimen that had been tested once was usually failed after a test and therefore could not be tested again. All this makes a parameter study including cracks of different sizes at various locations extremely elaborate and costly. Therefore, most researchers performed only a very limited number of tests using small test rotors and usually investigating a single crack location only.

In light of these obvious disadvantages Tamura et al. [100,101] proposed an alternative experimental crack model that would eliminate the need to grow a crack but allow the placement of an "imitation crack" of variable depth at a defined position. They placed a hollow cylinder between two flanges of a thin, solid rotor. The cylinder was mounted by 24 bolts. Tamura et al. proposed that by simply removing some bolts on either side of the cylinder, a crack of variable depth could be simulated. This would yield a much simplified and less expensive method to study the vibration of a cracked rotor. The crack size was approximated by the ratio of the cross-section that was still connected through the bolts to the part that was free to gap. Tamura et al. measured the vibration response over a range of rotational speeds and found that additional resonances existed at $1/2$, $1/3$, $1/4$, and $1/5$ of the critical speed, as they do for a cracked shaft. Furthermore, they

observed unstable vibration occurring at $2/3$ of the critical speed for large cracks, a point of instability which is predicted using non-linear analysis [33], but not with the linearized model. The same approach was used by Liao and Gasch [42] with a heavy disk instead of a cylinder. They compared their measurements to the analytical hinge model and achieved good agreement. Both, Tamura et al. and Liao and Gasch, concluded that the method represents a valid and effective approach to the experimental investigation of a cracked rotor. Their argument is that even though the local stress distribution in the case of the removed bolts is quite different from that of a true crack, the overall reduction in the shaft compliance is similar, resulting in a similar vibration pattern. Additionally, the non-linearity of the bending stiffness, i.e., reduced stiffness in tension and full stiffness in compression, is conserved. However, a major shortcoming of the studies was that neither provided quantitative comparison measurements between the bolt removal method and an experiment involving a grown fatigue crack.

A second alternative for a less elaborate crack model is the placement of a narrow slot at the location of the proposed crack and then filling the slot with an insertion. This method has been employed by Ishida et al. [59] and Ishida and Hirokawa [58]. The filler material must provide comparable material properties as the base material of the shaft. Also, the insertion must be manufactured to fit snug into the cut to provide compressive stiffness without affecting the tensile stiffness of the slotted shaft. This aspect obviously represents the greatest difficulty in employing the method while at the same time the manufactured slot will not provide the sharp crack tip of a real fatigue crack. Ishida et al. investigated the forward and backward whirl response curves for changing rotor speeds and verified the resonances for the $1/2$, $1/3$ and $2/3$ of the critical speed. Ishida and Hirokawa concluded that the qualitative vibration results were comparable to that of a cracked shaft, but they also did not provide comparison measurements from a shaft with a real fatigue crack.

2.4 Cracked shaft incidents in the field

Apart from designed experimental studies, there are several incidents of vibration measurement on cracked rotating machinery in operation prior to failure or shutdown.

Dimarogonas and Papadopoulos [34] investigated increased vibration levels on a 300 MW turbine at the Lavion power plant in Greece. In particular, the rotor exhibited increased 2/rev. and 3/rev. vibration amplitudes and resonance at half the critical speed. Upon machine inspection a transverse crack was found covering approximately 120° of the shaft cross-section. They also noted that the vibration measurements had picked up cross-coupling to longitudinal and torsional vibration, but that the levels were quite small for a crack of that size.

A similar incident was reported by Sanderson [102] as a 935 MW turbine generator operated by Ontario Hydro developed a crack at its shaft. The unit was equipped with a vibration monitoring system. A crack was suspected due to an increase in first and second harmonic amplitude and later confirmed during coast down. The period of time in which the propagating crack influenced the vibration of the turbine generator was confined to four days prior to shut down, during which the crack had propagated to 25 % of the rotor cross-section.

Lindley [103] reported on a crack in a generator rotor shaft that had initiated at a gas passage spline. A subsequent fractographic analysis enabled the association of beachmarks with the load history resulting in a good estimate of the crack propagation rate. It was established that the crack had grown halfway through the cross-section in about 800 hours of operation at a rotational speed of 3000 rpm. Bicego et al. [104] describe the discovery of a fatigue crack in a 370 MW generator rotor based on increased levels of vibration. The unit had been in service for 15 years and approximately 400 start-ups. Further analysis showed the crack had propagated through 55 % of the rotor cross-section and Bicego et al. particularly credit vibration monitoring with the prevention of catastrophic failure. By contrast, catastrophic failure occurred when a disk with blades sheared of the main shaft of a 10 MW turbo-generator [105]. Fractographic analysis revealed that the cause of the failure was a fatigue crack that had initiated at a rivet hole.

While turbo-generators used in the power industry represent a major occurrence for fatigue cracks in rotors, there are other applications where shaft cracks appear frequently.

Mahmoud and Kiefa [106] reported on welded steel drums with cracks initiating in the weld toes. Failure occurred after less than three months in operation. Gadala and Keiner [107] described extensive experimental and FEA studies on a pressure washer drum exhibiting fatigue cracks in the welded hub region. The cracks were due to the residual stresses and poor design of the drum component leading to frequent service shutdowns for repairs and significant loss in production. Cracks in vertically oriented pumps have been reported by Franklin et al. [89] and Nink and Stölben [76]. In both cases inspection revealed that cracks had propagated up to 80 % and 90 % of the shaft cross-section, respectively. Analysis by Nink and Stölben lead to the conclusion that an advanced vibration monitoring system could have detected cracks as small as 30 % of the cross-section.

Other examples of reported shaft crack occurrences in the field include the repeated cracking of brass rotor bars used in electric motors [108], cracks in a recirculation pump in a nuclear power plant [109,110], fatigue cracks in valve shafts initiating in the split ring groove [111] and fatigue cracks in the low pressure stage of a turbine shaft at the disc shrink-fit intersection [103]. Tjernberg [112] noted that fatigue cracks for hardened shafts can also initiate beneath the hardened layer.

The following is a summary of observations on machine vibrations made by researchers investigating the field incidents described previously:

- increased first harmonic response through rotor's first and second critical speed [34,89,102,104],
- slight reduction of critical speeds ($\approx 3\%$) [102,104],
- large second harmonic response at half the first and second critical speed [34,89,102,104],
- split peak at rotor's first critical speed [102],
- cross-coupling between lateral and longitudinal and lateral and torsional vibration components [34],
- change in phase lag [89],

- increased static deflection [104], and
- change in structural stiffness verified by modal analysis from impact test [104].

It is particularly encouraging to note that all of these indicators match the theoretical predictions described in sections 2.1 and 2.2.

2.5 The inverse problem of crack identification in solids

In the literature the inverse problem of crack identification in solids is commonly treated by transferring it to an optimization problem, minimizing the difference between obtained measurements and parameterized model. Kubo [113] gives a good theoretical overview over the area and introduces various solution techniques. In particular, Kubo notes that encountered difficulties in inverse problems are that they are often ill-posed, may have a non-unique solution or a solution may not exist at all. At the engineering side, Brandon [114] gives several examples where structural non-linearities were used for fault detection and points out important issues in this area of research.

A more detailed analysis of the problem for static and dynamic loading has been given by Stavroulakis [115] who mainly used the Boundary Element Method (BEM) to obtain the forward solution of the problem. He noted that the BEM is preferred to the Finite Element Method (FEM) due to the numerous required solutions of the forward problem and the associated extensive computational requirements when using the FEM. Stavroulakis also investigated various techniques to solve the non-linear optimization problem, such as non-linear programming, genetic algorithms and neural networks. He notes that the optimization problem is generally non-convex, thus global optimization algorithms, genetic algorithms and neural network methods seem more beneficial than local algorithms in the attempt to avoid local minima. Stavroulakis et al. [117,116] also suggested to break down the multi-variable inverse problem into separate sub-problems and investigated the feasibility when using a neural network approach.

Hsieh and Mura [118] introduced an algorithm for determining the shape and location in a cavity using the BEM. The cavity was defined by five DOF in a two-dimensional domain. A non-linear least-squares optimization algorithm was used which converged

independent of the initial conditions and proved insensitive to the number of known boundary conditions. Similar studies have been performed by Hwu and Liang [119] identifying a crack in a 2D elasticity problem using the BEM and an optimization algorithm based on the strain values, and by Liu and Chen [120] identifying a 3D penny-shaped crack in a cylinder. The BEM was also used by Ulrich et al. [121]. To improve the initial guess for the optimization algorithm they suggested the introduction of a boundary difference function. This function evaluates the difference between the measured displacements of the flawed structure and the initial displacements for the unflawed case. An improved initial guess can be obtained, which will improve the convergence time significantly.

Schnur and Zabras [122,123] developed a method to identify an inclusion of different material properties in a two dimensional domain using the FEM. The Levenberg-Marquardt algorithm was used to solve the optimization problem, and regularization techniques were used to stabilize the minimization process by imposing various degrees of smoothness on the solution. The same technique has been employed by Keat et al. [124,125] for 3D subsurface crack identification based on holographic interferometry measurements of the surface displacement of pressurized cubes.

McCullough and Gadala [126] performed a study identifying a through thickness crack by location, size, and orientation in a rectangular plate. Substructuring of the region around the crack was used in order to significantly lessen the computational requirements of the repeated FEA. They pointed out the importance of an accurate initial guess in achieving the global minimum. The FEM in conjunction with regularization of the optimization problem has also been used by Maniatty et al. [127].

Genetic algorithms for crack identification have been used by Stavroulakis [115], Doyle [82], Ruotolo and Surace [91] and Burczynski and Beluch [128] who also investigated the feasibility of multi-crack identification. The feasibility of a neural network approach has been investigated by Stavroulakis [115-116] and Mahmoud and Abu Kiefa [106]. Suh and Shim [129] employed a hybrid neural network and genetic

algorithm approach for crack identification based on the dynamic analysis of beams using beam FEA and natural frequency measurements. Also, the numerous contributions by Gladwell, who investigated the mathematical reconstruction of the complete stiffness and mass matrices based on the knowledge of modal quantities, must be noted [130-134].

Only few attempts have been made in the literature to solve the inverse problem of identifying size and location of a crack in a rotor. Ratan et al. [48], Nandwana and Maiti [94,95], and Tsai and Wang [67] tried to locate a crack by utilizing assumptions of discontinuous slope and change in natural frequency. However, all approaches were based on one-dimensional beam models containing very few elements and requiring knowledge of the solution over virtually the entire boundary. For this reason, the approaches seem only of limited usefulness for practical purposes.

Seibold and Weinert [93,135] used an Extended Kalman Filter approach for crack detection in a Laval rotor and were able to identify the crack size for a known crack location. He et al. [136,137] have used a genetic algorithm in conjunction with the FEM to detect a crack in a rotor bearing system. They conclude that the genetic algorithm is more suited for this kind of problem than common local optimization techniques. However, they also mention the very high computational requirements, greater than ten hours, even for a genetic search with relatively low population.

Keiner and Gadala [138] investigated the feasibility of using on-line vibration measurements and 3D FE modeling for crack detection in a slow rotating drum. They concluded that measured vibration signatures were distinct enough to identify different crack sizes and showed good agreement between experimental and FE results. Scheibel et al. [21] and Carlson et al. [139] developed an expert system for fault diagnosis based on the work by Imam et al. [41]. The system was implemented on a steam turbine at a power plant in Lauderdale, Florida. They concluded that the knowledge-based system is suitable for evaluating multiple-fault symptoms (vibration response, shaft position, etc.) and distinguishing cracking from other faults such as misalignment and unbalance. No attempt was made trying to quantify crack size and location.

CHAPTER 3

VIBRATION MODELING OF A CRACKED ROTOR

The vibration of a rotor with a cracked shaft under gravity is caused by the varying bending stiffness of the shaft depending on whether the crack is open or closed.

Figure 3.1 shows a simple Laval rotor under gravity load. When the crack is on the top side of the shaft, the crack faces will be in compression and the shaft stiffness is equal to the stiffness of the uncracked shaft. As the shaft rotates, the cracked section will move into the tensile stress region. The crack opens up and the shaft stiffness will decrease causing a greater vertical deflection. The shaft stiffness will reach its minimum as the crack center reaches the bottom of the shaft and the crack faces are fully open. Further rotation closes the crack again, thus the deflection is restored to the uncracked case. In addition to the increased vertical deflection, the rotor will also deflect horizontally due to the asymmetry of the cracked cross-section with respect to the direction of the load. The mechanism of periodic crack opening and closing is called crack breathing. The following is a description of three different methods to determine the vibration of such a system.

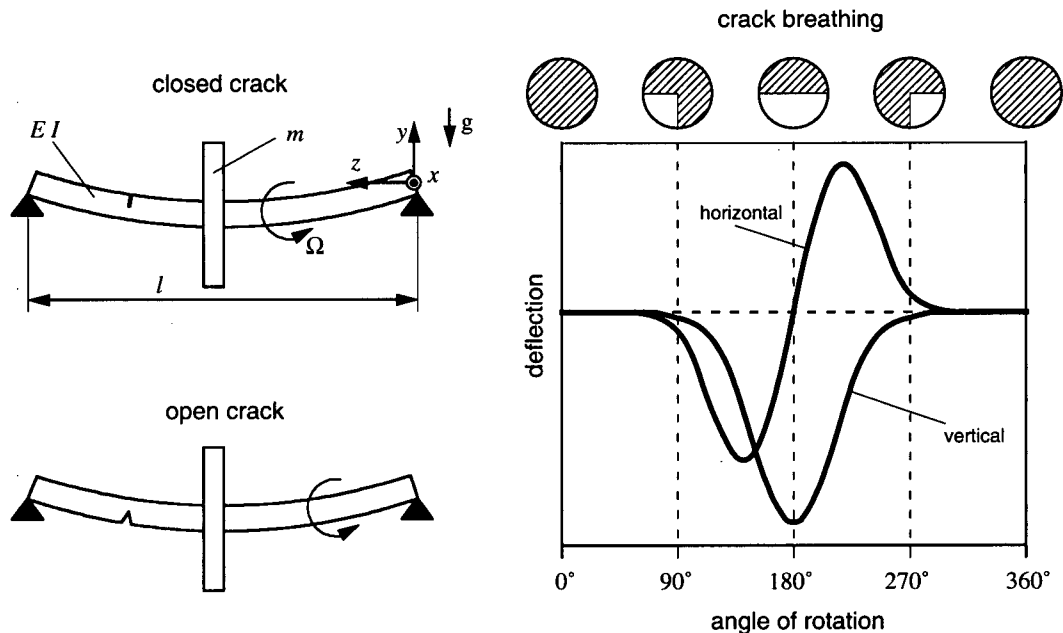


Figure 3.1: Vibration of a cracked rotor.

3.1 Analytical solution

The analytical approach is based on the simplified two DOF model shown in Figure 3.2.

The equations of motion for this model may be written as

$$\mathbf{M}\ddot{\mathbf{u}} + \mathbf{C}\dot{\mathbf{u}} + \mathbf{K}\mathbf{u} = \mathbf{F} \quad (3.1)$$

where: $\mathbf{M} = \begin{bmatrix} m & 0 \\ 0 & m \end{bmatrix}$, $\mathbf{C} = \begin{bmatrix} c & 0 \\ 0 & c \end{bmatrix}$, $\mathbf{K}(u, \Omega t) = \begin{bmatrix} k_{xx}(u, \Omega t) & k_{xy}(u, \Omega t) \\ k_{yx}(u, \Omega t) & k_{yy}(u, \Omega t) \end{bmatrix}$,

$$\mathbf{F} = \begin{bmatrix} 0 \\ -mg \end{bmatrix}, \quad \mathbf{u} = \begin{bmatrix} u_x \\ u_y \end{bmatrix} \text{ and } \Omega = \text{rotational velocity.}$$

In general, equation 3.1 is a non-linear second order differential equation for which there is no unique, closed form solution available. However, equation 3.1 may be linearized based on the assumption that the static deflection of the rotor is dominant over the vibration, thus the shaft stiffness may be expressed in terms of the angle of rotation only, i.e., $\mathbf{K} = \mathbf{K}(\Omega t)$. \mathbf{K} may be determined analytically using the method by Dimarogonas [33]. The shaft stiffness is decomposed into a constant component of the uncracked shaft, \mathbf{K}_0 , and a variable component due to crack breathing, $\Delta\mathbf{K}(\Omega t)$.

$$\mathbf{M}\ddot{\mathbf{u}} + \mathbf{C}\dot{\mathbf{u}} + (\mathbf{K}_0 - \Delta\mathbf{K}(\Omega t)) (\mathbf{u}_{static} + \Delta\mathbf{u}) = \mathbf{F} \quad (3.2)$$

where: u_{static} = static deflection of the uncracked shaft.

$$\Rightarrow \mathbf{M}\ddot{\mathbf{u}} + \mathbf{C}\dot{\mathbf{u}} + \mathbf{K}_0\mathbf{u} = \mathbf{F} + \Delta\mathbf{K}(\Omega t) \mathbf{u}_{static} \quad (+ \Delta\mathbf{K}(\Omega t) \Delta\mathbf{u}) \quad (3.3)$$

Neglecting the second order term results in a linear differential equation with constant coefficients which may be solved using linear dynamic analysis. The term $\Delta\mathbf{K}(\Omega t) \mathbf{u}_{static}$ is called the crack force [42] and may be Fourier transformed into harmonics of the rotational speed.

$$\Rightarrow \mathbf{M}\ddot{\mathbf{u}} + \mathbf{C}\dot{\mathbf{u}} + \mathbf{K}_0\mathbf{u} = \mathbf{F} + \sum_{k=0}^{\infty} A_k \cos(k\Omega t) + B_k \sin(k\Omega t) \quad (3.4)$$

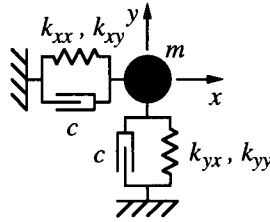


Figure 3.2: Two DOF model of a cracked rotor.

The method represents a very efficient way in approximating the vibration of a cracked rotor. Alternatively, equation (3.1) may be solved directly through numerical time-integration from initial conditions.

3.2 3D transient FE analysis

To avoid the above made assumptions regarding shaft and crack geometry, local crack compliance, crack breathing mechanism and dominant static deflection, the only viable alternative is a transient analysis using 3D solid finite elements. Figure 3.3 shows a FE model of a cracked shaft segment using eight-noded, linear brick elements. The crack face surfaces are modeled using double nodes which are identical in location but topologically belong either to the right or the left crack face. When all crack face nodes are coupled, the model is identical to the uncracked shaft and the depicted nodal coupling forces represent the load transfer across the crack faces. Therefore, the closed crack is modeled by coupling the double nodes, giving the rotor compressive stiffness over the crack faces, while the open crack is modeled by removing the coupling bonds, allowing the crack faces to gap. It is obvious that this form of crack modeling allows an easy adaptation to a more complicated rotor geometry and crack shape. The analysis is performed through time-integration from initial conditions, e.g., nominal rotational velocity and static deflection of the shaft with the crack being fully closed in the compressive region. As part of the crack faces are rotated into the tensile region, these double nodes are uncoupled and the crack begins to open. When the crack faces lie completely in the tensile region, the crack is fully open and all double nodes are

uncoupled. As the crack front reaches the compressive region again, the double nodes are re-coupled and the crack begins to close.

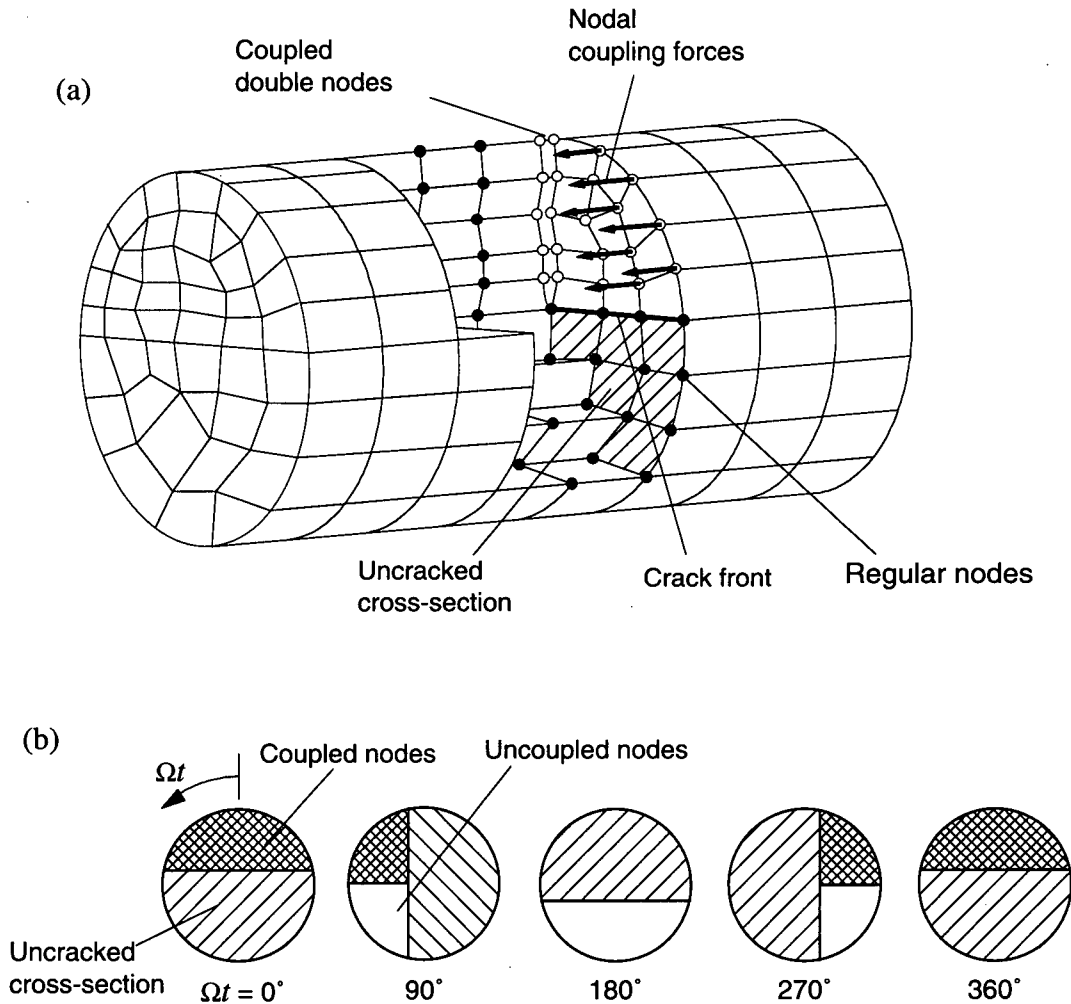


Figure 3.3: 3D FE model of a cracked shaft segment. (a) Double nodes are used to model the crack faces. The nodes are coupled when the crack is closed, uncoupled when it is open. The nodal coupling forces represent the load transfer across the crack faces.

(b) Uncoupling and re-coupling of nodes is used to simulate crack breathing over one revolution.

There are several direct integration methods available in the literature to perform the time-integration from initial conditions, e.g., the Newmark method which has been implemented in the commercial FE code ANSYS [140]. Here, the FE equilibrium equations are solved at discrete time steps $t+\Delta t$.

$$\mathbf{M} \text{}^{t+\Delta t}\ddot{\mathbf{U}} + \mathbf{C} \text{}^{t+\Delta t}\dot{\mathbf{U}} + \mathbf{K} \text{}^{t+\Delta t}\mathbf{U} = \text{}^{t+\Delta t}\mathbf{R} \quad (3.5)$$

Under the assumption that acceleration and velocity at $t+\Delta t$ can be expressed by

$$\text{}^{t+\Delta t}\ddot{\mathbf{U}} = \frac{1}{\gamma} \left[\frac{1}{\Delta t^2} \text{}^{t+\Delta t}\mathbf{U} - \text{}^t\mathbf{U} - \dot{\mathbf{U}}\Delta t - (0.5 - \gamma) \text{}^t\ddot{\mathbf{U}} \right] \quad (3.6)$$

$$\text{}^{t+\Delta t}\dot{\mathbf{U}} = \text{}^t\dot{\mathbf{U}} + [(1 - \delta) \text{}^t\dot{\mathbf{U}} + \delta \text{}^{t+\Delta t}\dot{\mathbf{U}}] \quad (3.7)$$

where γ and δ are parameters that may be determined to obtain integration accuracy and stability. For $\gamma = 0.25$ and $\delta = 0.5$ the method results in the constant average acceleration method which is unconditionally stable [141].

3.3 3D nodal crack force approach

3.3.1 Linearization of the 3D FE equations

In order to combine the advantages of the simple solution scheme of the analytical crack force approach with the versatility in rotor and crack geometry of the 3D transient analysis, a new approach is introduced labeled the 3D nodal crack force approach. In this approach, the same FE model is used as in the transient analysis, see Figure 3.3, containing the coupled double nodes at the crack faces. However, analogue to the analytical crack force method, the crack breathing mechanism is approximated by nodal crack forces under the assumption of dominant static deflection. When all crack face nodes are coupled, the model is identical to the uncracked rotor, and the depicted nodal coupling forces represent the load transfer across the crack faces. The uncracked rotor, i.e., all coupling bonds remain intact, is now analyzed under steady state conditions for the applied load at various angles of rotation and the resulting nodal coupling forces are

recorded. It must be noted that for the solution of the FE equations it is irrelevant if the crack face nodes are indeed coupled or if the coupling forces are known a priori and then applied as external nodal forces on the uncoupled crack face nodes. The resulting displacements will be identical since the same linear system of equations is solved for. Therefore, it may be concluded that the steady state solution of the uncracked shaft is identical with the steady state solution of a cracked shaft that has the nodal coupling forces applied as external loading.

For the breathing crack, the coupled nodal forces exist when the crack is closed and the crack faces are in compression, but they are missing when the crack is open and the crack faces are in tension. This effect may be achieved by adding a time-dependent nodal crack force as applied external load to the crack face nodes, which will be of equal magnitude but opposite direction of any tensile nodal coupling force, while being zero at times when the nodal coupling force is compressive; see Figure 3.4. Superposition of these two load cases results in a breathing crack mechanism which only transfers compressive load over the crack faces. Superposition is valid because the FE model is always the cracked model and the nodes are never coupled throughout the analysis procedure, thus the stiffness matrix remains constant. In essence, the approach is the three-dimensional equivalent to the analytical nodal crack force method by Mayes and Davies [27] described in section 3.1.

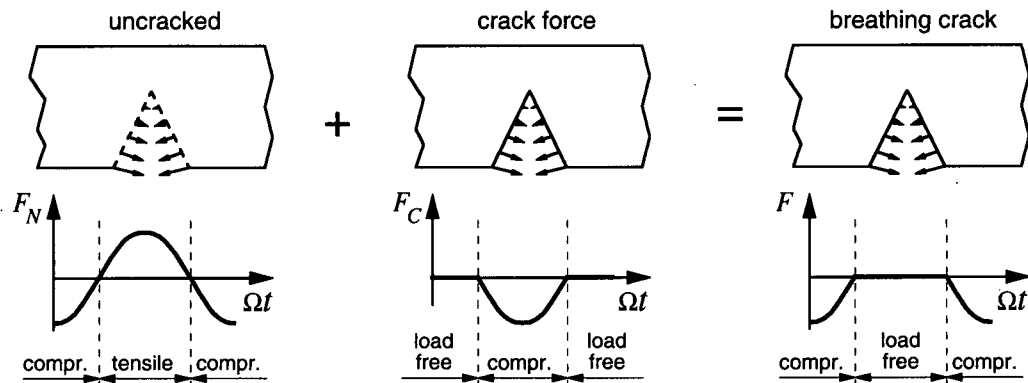


Figure 3.4: Superposition of the nodal crack forces used to simulate crack breathing.

Practically the FE model with all nodes coupled is analyzed in a steady state analysis at discrete points of angle of rotation under the applied load of the rotor, e.g., gravity. The nodal coupling forces are recorded as discrete function of the angle of rotation, i.e., $F_N^n = F_N^n(\Omega t)$, and the nodal crack forces are computed by

$$F_C^n(\Omega t) = \begin{cases} -F_N^n(\Omega t) & ; F_N^n(\Omega t) \geq 0 \\ 0 & ; F_N^n(\Omega t) < 0 \end{cases} \quad (3.8)$$

where F_N^n is the recorded nodal coupling force, F_C^n the nodal crack force, Ωt the angle of rotation and n the node number of the crack face node.

The dynamic FE equations to be solved result in

$$\mathbf{M}\ddot{\mathbf{u}} + \mathbf{C}\dot{\mathbf{u}} + \mathbf{K}\mathbf{u} = \mathbf{F} + \mathbf{F}_N + \mathbf{F}_C \quad (3.9)$$

where: \mathbf{M} , \mathbf{C} and \mathbf{K} = mass, damping and stiffness matrix of the cracked rotor,
 \mathbf{F} = applied external loading (e.g., gravity),
 \mathbf{F}_N = coupling forces acting on crack face nodes,
 \mathbf{F}_C = crack forces acting on crack face nodes.

Note that the partial solution u_1 , where: $u_1 + u_2 = u$, of equation

$$\mathbf{M}\ddot{\mathbf{u}}_1 + \mathbf{C}\dot{\mathbf{u}}_1 + \mathbf{K}\mathbf{u}_1 = \mathbf{F} + \mathbf{F}_N \quad (3.10)$$

is the solution to the uncracked rotor problem which has already been solved for when obtaining the nodal coupling forces, thus only the partial solution u_2 of equation

$$\mathbf{M}\ddot{\mathbf{u}}_2 + \mathbf{C}\dot{\mathbf{u}}_2 + \mathbf{K}\mathbf{u}_2 = \mathbf{F}_C \quad (3.11)$$

needs to be solved for to find the combined solution u .

3.3.2 Solving the FE equations in a rotating coordinate system

The stiffness matrix \mathbf{K} in equation (3.11) is described in stationary coordinates and therefore still depends on the angle of rotation Ωt . To avoid this, equation (3.11) must be transferred into a body-fixed, rotating coordinate system.

Figure 3.5 shows the lumped nodal mass m located at r_0 described in the stationary coordinate system (x,y,z) and a rotating coordinate system (ξ,η,z) revolving about the z -axis with angular velocity Ω . The point m^* represents the location of m after a certain time t were m to move with the rotating coordinate system (ξ,η,z) . Vectors ζ and ε are described in the rotating coordinate system, thus the relationship between r and ζ is given by:

$$r(\Omega t) = \mathbf{R}\zeta, \quad \text{where:} \quad \mathbf{R} = \begin{bmatrix} \cos \Omega t & -\sin \Omega t & 0 \\ \sin \Omega t & \cos \Omega t & 0 \\ 0 & 0 & 1 \end{bmatrix}. \quad (3.12)$$

The displacement u from m to m' may be expressed in rotating coordinates as

$$u = \mathbf{R}\varepsilon + (\mathbf{R} - \mathbf{I})r_0 \quad (3.13)$$

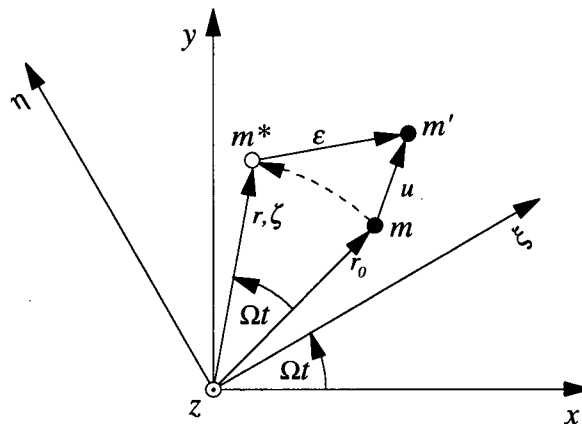


Figure 3.5: Displacement of a point mass m rotating about z in stationary and rotating coordinates; m^* denotes the unperturbed position of m at time t .

where \mathbf{I} is the identity matrix. The equations of motion for the nodal mass m rotating about the origin described in the stationary coordinate system (x,y,z) are given by

$$\mathbf{M}\ddot{u} + \mathbf{C}\dot{u} + \mathbf{K}(u + (\mathbf{I} - \mathbf{R})r_0) = F . \quad (3.14)$$

Replacing u with the expression from equation (3.13) results in

$$\dot{u} = \dot{\mathbf{R}}\boldsymbol{\varepsilon} + \mathbf{R}\dot{\boldsymbol{\varepsilon}} + \dot{\mathbf{R}}r_0 , \quad \ddot{u} = \mathbf{R}\ddot{\boldsymbol{\varepsilon}} + 2\dot{\mathbf{R}}\dot{\boldsymbol{\varepsilon}} + \ddot{\mathbf{R}}\boldsymbol{\varepsilon} + \ddot{\mathbf{R}}r_0 , \quad (3.15)$$

$$\dot{\mathbf{R}} = \begin{bmatrix} -\sin \Omega t & -\cos \Omega t & 0 \\ \cos \Omega t & -\sin \Omega t & 0 \\ 0 & 0 & 0 \end{bmatrix} , \quad \ddot{\mathbf{R}} = -\Omega^2 \begin{bmatrix} \cos \Omega t & -\sin \Omega t & 0 \\ \sin \Omega t & \cos \Omega t & 0 \\ 0 & 0 & 0 \end{bmatrix} = -\Omega^2 \tilde{\mathbf{R}} , \quad (3.16)$$

and finally:

$$\mathbf{M}\mathbf{R}\ddot{\boldsymbol{\varepsilon}} + (2\mathbf{M}\dot{\mathbf{R}} + \mathbf{C}\mathbf{R})\dot{\boldsymbol{\varepsilon}} + (\mathbf{K}\mathbf{R} - \Omega^2\mathbf{M}\tilde{\mathbf{R}} + \mathbf{C}\dot{\mathbf{R}})\boldsymbol{\varepsilon} = F + \Omega^2\mathbf{M}\tilde{\mathbf{R}}r_0 - \mathbf{C}\dot{\mathbf{R}}r_0 \quad (3.17)$$

Pre-multiplying equation (3.17) with \mathbf{R}^T yields

$$\begin{aligned} & \mathbf{R}^T\mathbf{M}\mathbf{R}\ddot{\boldsymbol{\varepsilon}} + (2\mathbf{R}^T\mathbf{M}\dot{\mathbf{R}} + \mathbf{R}^T\mathbf{C}\mathbf{R})\dot{\boldsymbol{\varepsilon}} + (\mathbf{R}^T\mathbf{K}\mathbf{R} - \Omega^2\mathbf{R}^T\mathbf{M}\tilde{\mathbf{R}} + \mathbf{R}^T\mathbf{C}\dot{\mathbf{R}})\boldsymbol{\varepsilon} \\ & = \mathbf{R}^TF + \Omega^2\mathbf{R}^T\mathbf{M}\tilde{\mathbf{R}}r_0 - \mathbf{R}^T\mathbf{C}\dot{\mathbf{R}}r_0 \end{aligned} \quad (3.18)$$

Under the assumption that mass and damping matrix are diagonal matrices of equal members, i.e., $\mathbf{M} = \text{diag}(m,m,m)$ and $\mathbf{C} = \text{diag}(c,c,c)$, equation (3.18) may be written as

$$\mathbf{M}\ddot{\boldsymbol{\varepsilon}} + (2\Omega\mathbf{M}\mathbf{G} + \mathbf{C})\dot{\boldsymbol{\varepsilon}} + (\mathbf{K}' - \Omega^2\tilde{\mathbf{M}} + \Omega\mathbf{C}\mathbf{G})\boldsymbol{\varepsilon} = \mathbf{R}^TF + \Omega^2\tilde{\mathbf{M}}r_0 - \Omega\mathbf{C}\mathbf{G}r_0 \quad (3.19)$$

where: $\mathbf{K}' = \mathbf{R}^T\mathbf{K}\mathbf{R}$, $\tilde{\mathbf{M}} = \text{diag}(m,m,0)$ and $\mathbf{G} = \mathbf{R}^T\dot{\mathbf{R}} = \begin{bmatrix} 0 & -1 & 0 \\ 1 & 0 & 0 \\ 0 & 0 & 0 \end{bmatrix}$.

\mathbf{K}' represents the stiffness matrix of the rotor in rotating coordinates and does not depend on Ωt , thus equation (3.19) may now be solved as a linear dynamic problem. The terms $\Omega^2 \tilde{\mathbf{M}} \boldsymbol{\varepsilon}$ and $\Omega^2 \tilde{\mathbf{M}} r_0$ represent centrifugal forces, $2\Omega \mathbf{M} \mathbf{G} \dot{\boldsymbol{\varepsilon}}$ the Coriolis force, and $\Omega \mathbf{C} \mathbf{G} \boldsymbol{\varepsilon}$ and $\Omega \mathbf{C} \mathbf{G} r_0$ additional forces due to damping described in the rotating coordinate system. These terms must be added to the FE model as additional damping and stiffness elements and applied forces. This may be achieved by adding user-defined elements and forces to every node of the FE model. Note that this does not increase the size of the problem since it will only increase the number of elements in the model but not the number of nodes or DOF.

The solution process of equation (3.19) is done by linear harmonic response analysis. The discrete set of nodal crack forces $F_C(\Omega t)$ is placed into rotating coordinates, transformed by Fourier analysis and the first $p+1$ terms are considered:

$$\mathbf{R}^T F_C(\Omega t) = \sum_{k=0}^p A_k \cos(k\Omega t) + B_k \sin(k\Omega t) \quad (3.20)$$

Replacing the applied load $\mathbf{R}^T F$ in equation (3.19) with $\mathbf{R}^T F_C$ yields:

$$\begin{aligned} \mathbf{M} \ddot{\boldsymbol{\varepsilon}} + (2\Omega \mathbf{M} \mathbf{G} + \mathbf{C}) \dot{\boldsymbol{\varepsilon}} + (\mathbf{K}' - \Omega^2 \tilde{\mathbf{M}} + \Omega \mathbf{C} \mathbf{G}) \boldsymbol{\varepsilon} \\ = \Omega^2 \tilde{\mathbf{M}} r_0 - \Omega \mathbf{C} \mathbf{G} r_0 + A_0 \\ + A_1 \cos(\Omega t) + B_1 \sin(\Omega t) \\ + A_2 \cos(2\Omega t) + B_2 \sin(2\Omega t) \\ + \dots \\ + A_p \cos(p\Omega t) + B_p \sin(p\Omega t) \end{aligned} \quad (3.21)$$

The problem may now be solved in $p+1$ linear harmonic response analyses and the solutions are superimposed:

$$\boldsymbol{\varepsilon} = \boldsymbol{\varepsilon}_0 + \boldsymbol{\varepsilon}_1 + \dots + \boldsymbol{\varepsilon}_p \quad (3.22)$$

ϵ is then transformed back to stationary coordinates and superimposed with u_1 from equation (3.10):

$$u_2 = \mathbf{R}\epsilon \quad (3.23)$$

$$u = u_1 + u_2 \quad (3.24)$$

The computational savings of the nodal crack force approach over a complete transient analysis are tremendous. For example, if the steady state solution (u_1) and the nodal coupling forces (F_N) are evaluated in a series of linear analyses at an increment of 15° over one full revolution, and the cracked vibration response is determined using the first six Fourier coefficients, the linear FE equations must be solved a total of 30 times. In comparison, a transient analysis over four revolutions with an incremental step of 5° and approximately four iterations per step results to 1152 necessary solutions of the same equations. This yields a computational savings factor of approximately 1:40 for the nodal crack force approach, much greater when symmetry can be used in determining the steady state solution. Furthermore, any re-evaluation of the cracked vibration response for a different set of parameters requires only the six dynamic linear analyses, as long as the steady state solution remains valid.

3.4 Verification of the nodal crack force approach

Two example problems were solved to compare the two DOF analytical (anal.) and 3D transient FE (tran.) methods and to verify the validity of the nodal crack force (NCF) approach.

3.4.1 Example 1 — Short cantilever shaft

Example 1 is a weightless cantilever shaft ($D = 40$ mm, $l = 100$ mm) under gravity load with a heavy mass ($m = 257$ kg) at its free end, as shown in Figure 3.6. The material properties used were those of aluminium ($E = 70$ GPa, $\nu = 0.3$). No damping was considered throughout the analysis. A transverse crack was located at mid span and the crack length to shaft diameter ratio was $a/D = 0.25$. The reduced stiffness due to the crack in the analytical model was computed using the method by Dimarogonas [33]. Crack breathing was simulated using the reduced stiffness of the fully open crack when the crack was in tension and the uncracked shaft stiffness when the crack was in compression. For the nodal crack force approach, the static deflection was calculated for one full revolution in increments of 15° , and the nodal coupling forces were recorded. The nodal crack forces and the analytical crack force were determined by Fourier analysis considering the first six terms. The transient analysis was performed using the Newark method and an incremental angle of rotation $\Delta\Omega t = 5^\circ$ resulting in a time step size $\Delta t = \Delta\Omega t/\Omega$. Initial conditions were established by applying the external gravity load and displacement boundary conditions for an initial, small time step ignoring inertia effects.

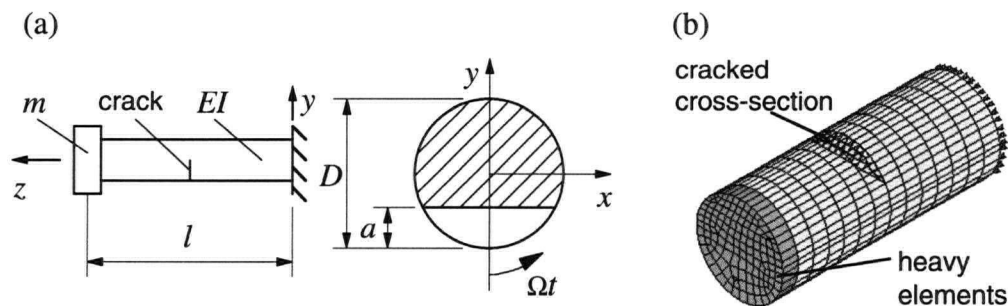


Figure 3.6: (a) Analytical and (b) 3D FE model of a cantilever shaft with a transverse crack at mid span.

The solution was computed for four revolutions and in general stabilized after two to three revolutions. All solutions for the 3D FE model were obtained using the commercial FE code ANSYS [140]. Plotted displacements were made non-dimensional by dividing through the vertical static deflection from the FE analysis.

Table 3.1 lists uncracked static deflection and natural frequency for the analytical and the FE model. The resulting horizontal and vertical deflections for the quasi-static case, i.e., $\Omega/\omega_n = 0.001$, ω_n being the lowest lateral natural frequency of the uncracked FE model, are shown in Figure 3.7. The horizontal deflection from the nodal crack force approach and the transient analysis show a slight discrepancy, while the vertical deflections are practically identical. The deflection based on the analytical model proves too flexible in both directions, which is due to the greater analytical crack compliance compared to 3D FE results [51,55].

Model	Static deflection [μm]	1 st Natural frequency [Hz]		
		uncracked	cracked	
			horizontal	vertical
Analytical	85	53.8	53.4	50.5
3D-FEA	97	52.0	51.7	49.9

Table 3.1: Comparison of static deflection and natural frequency between analytical and 3D FE model for a cantilever shaft.

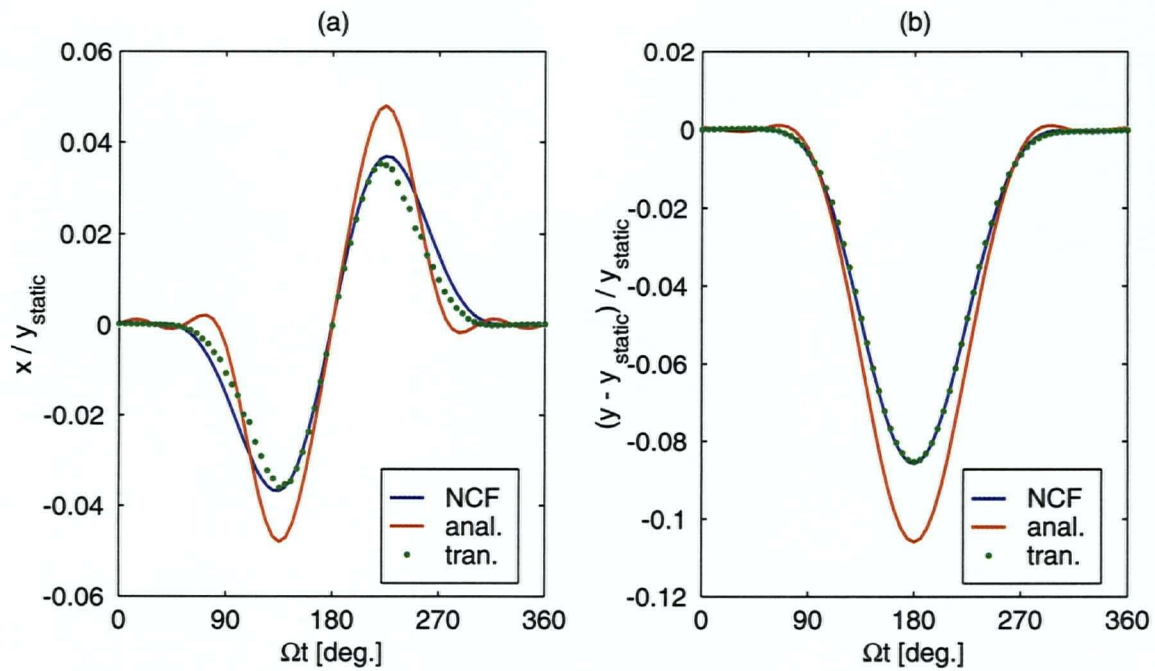


Figure 3.7: Non-dimensional, quasi-static (a) horizontal and (b) vertical displacement of a cracked cantilever shaft.

The shaft orbits for a rotational speed of $\Omega/\omega_n = 0.32, 0.45$ and 0.9 are shown in Figure 3.8. For $\Omega/\omega_n = 0.9$, the rotational speed is close to the critical speed of the shaft, thus the two orbits from the linearized solutions are dominated by a single loop due to the first harmonic excitation component of the crack forces. The transient solution shows a spiral from the initial conditions at the origin approximately to the size of the nodal crack force solution with each loop representing a full revolution of the shaft. The orbits for $\Omega/\omega_n = 0.46$ exhibit the double loop typically associated with the existence of a crack in a shaft rotating close to half its critical speed [2]. Qualitatively the orbit shapes from all methods are very similar, but quantitatively the nodal crack force approach yields a slightly better match than the analytical solution.

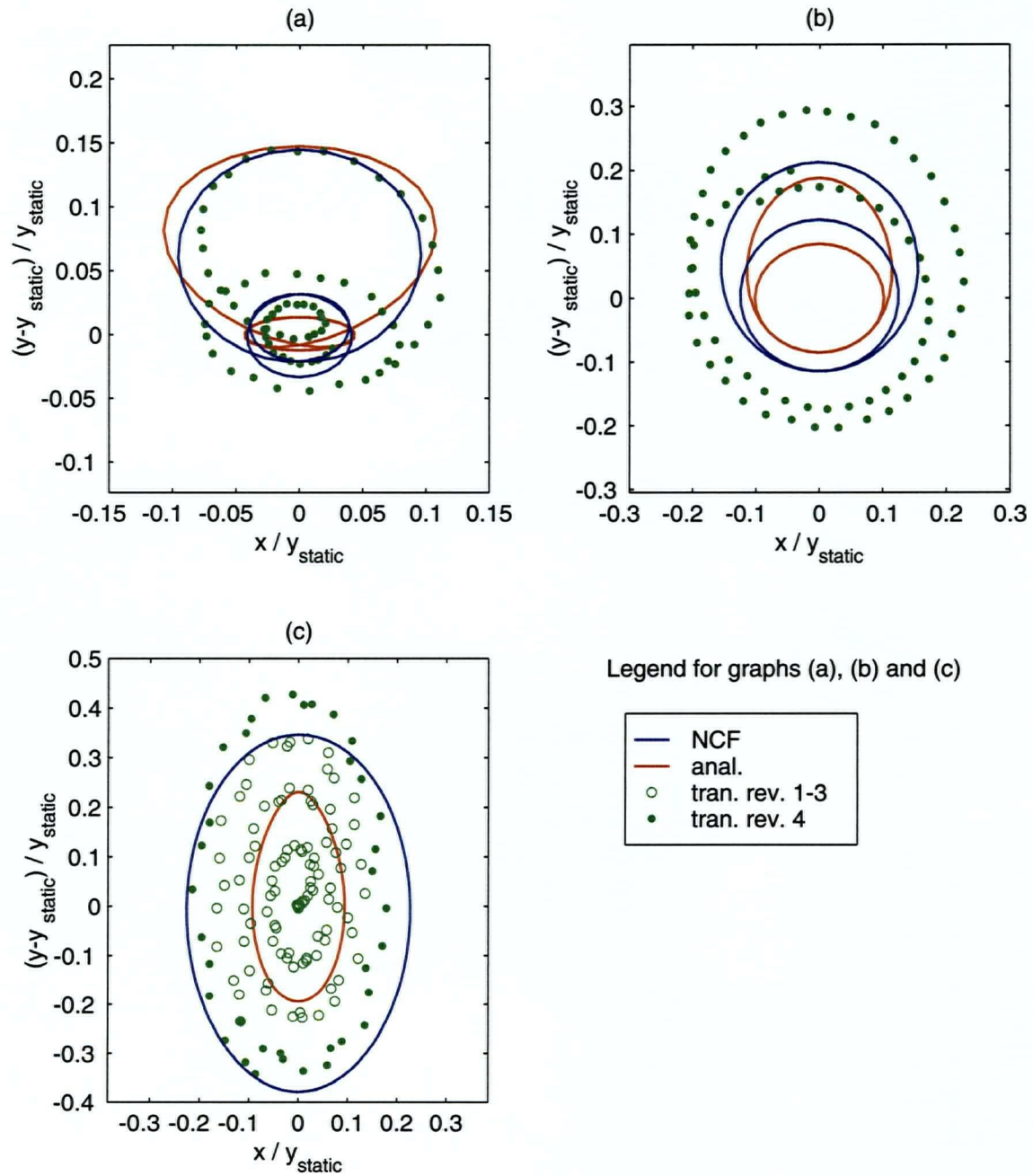


Figure 3.8: Non-dimensional orbits of a cantilever shaft for rotational speeds:

(a) $\Omega/\omega_n = 0.32$, (b) 0.45 and (c) 0.9 .

3.4.2 Example 2 — Laval rotor

In a second example, a Laval rotor ($D = 25$ mm, $l = 2000$ mm) with point mass ($m = 20$ kg) at mid span under gravity load was considered; see Figure 3.9. The shaft was modeled with simple support boundary conditions at both ends and the material properties of aluminium ($E = 70$ GPa, $\nu = 0.3$). The crack was located at quarter length with $a/D = 0.4$. In the FE model only the region around the crack was modeled using eight-noded 3D solid elements. The remainder of the shaft was modeled using two-noded Timoshenko beam elements with six DOF at each node. In the transition zone between beam and 3D solid elements, very stiff four-noded shell elements overlaid the shaft cross-section, transferring the bending moment and providing the continuity of the shaft's slope. Damping was included and the modal damping factor was set to $\zeta = 0.05$. The analysis process for both models was identical with that of the previous example.

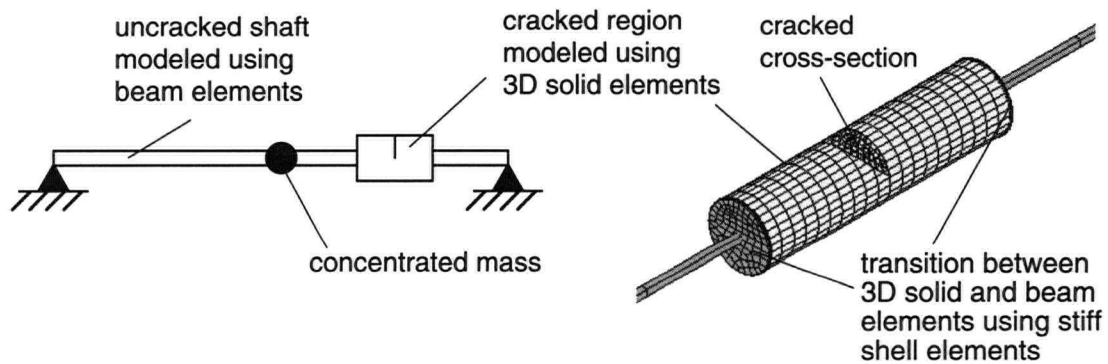


Figure 3.9: 3D FE model of a simply supported Laval rotor with a transverse crack at quarter length.

Model	Static deflection [mm]	1 st Natural frequency [Hz]		
		uncracked	cracked	
			horizontal	vertical
Analytical	1.523	12.8	12.6	12.1
3D-FEA	1.520	12.8	12.8	12.6

Table 3.2: Comparison of static deflection and natural frequency between analytical and 3D FE model for a Laval rotor.

Table 3.2 compares the natural frequency and uncracked static deflection. The good agreement proves the validity of employing the shell elements for the transition between beam and 3D solid elements. The resulting horizontal and vertical deflection for the quasi-static case, i.e., $\Omega/\omega_n = 0.001$, is shown in Figure 3.10. Again, the results from the transient analysis and the nodal crack force approach are virtually identical while the analytical solution exhibits much greater values due to the greater local crack compliance.

The vibration amplitude for various rotational speeds was computed and the results are shown in Figure 3.11. The additional peaks at 1/2 and 1/3 of the uncracked natural frequency due to the crack can be clearly identified. Overall vibration amplitudes from transient and nodal crack force analyses show good agreement while the analytical solution is significantly greater over the entire range of rotational speeds. Therefore, results from the analytical approach are ignored in the following comparison of orbits, shown in Figure 3.12. Quantitatively the orbits show good agreement and seem to match more closely than the orbits of Example 1. In particular, the transient solution seems more stable over the course of one revolution, which can be attributed to the damping and the diminishing effect of the initial conditions.

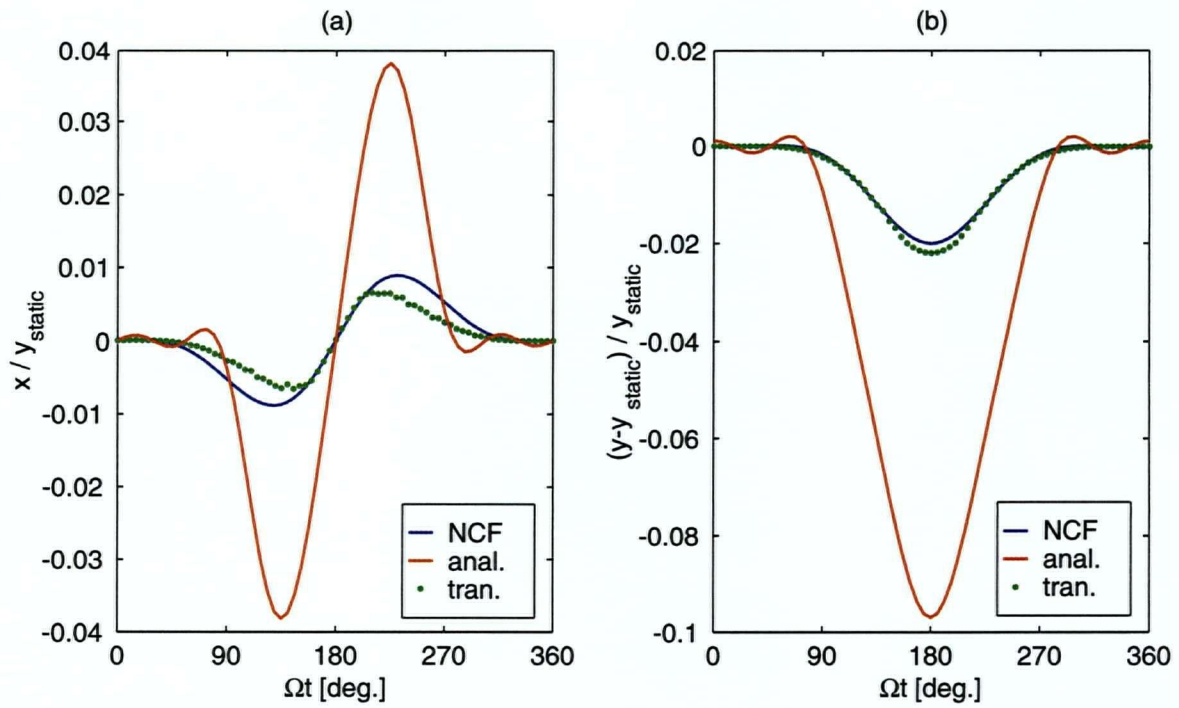


Figure 3.10: Non-dimensional quasi-static (a) horizontal and (b) vertical displacement of a cracked Laval rotor.

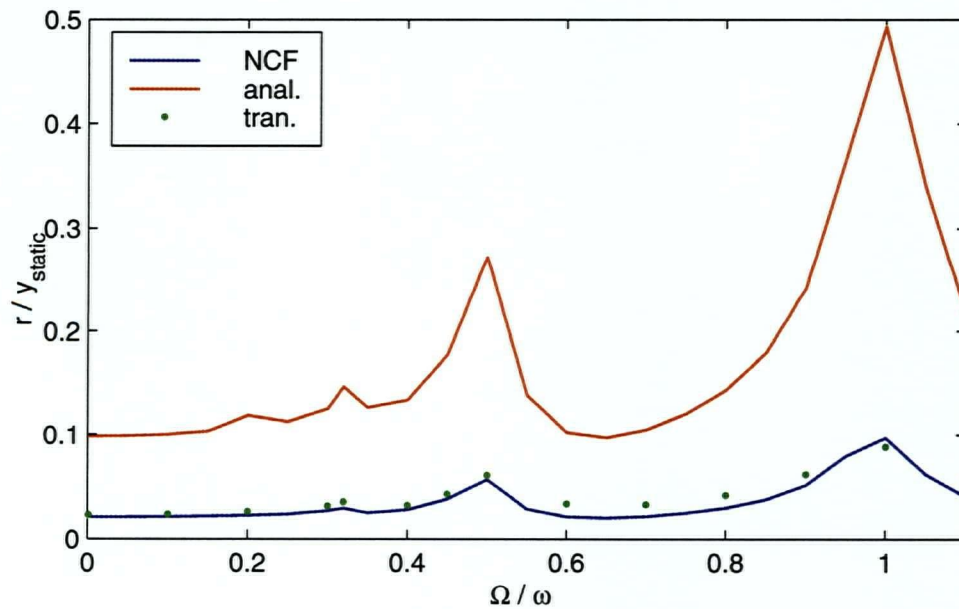


Figure 3.11: Comparison of the non-dimensional vibration amplitude r/y_{static} ,

where: $r = \sqrt{x^2 + (y - y_{static})^2}$, over the subcritical range.

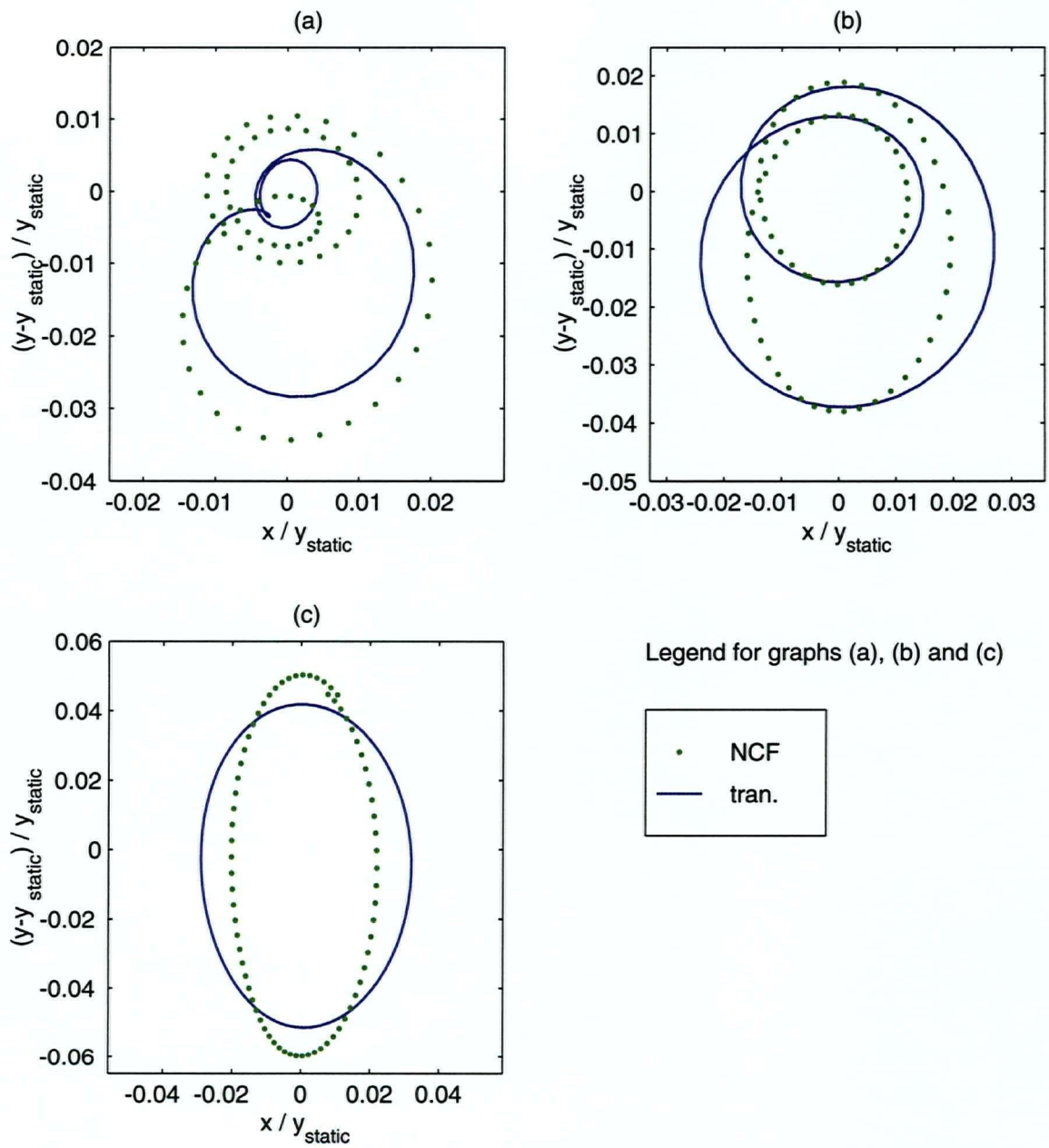


Figure 3.12: Non-dimensional orbits of a Laval rotor for rotational speeds:

(a) $\Omega/\omega_n = 0.32$, (b) 0.45 and (c) 0.9 .

CHAPTER 4

3D FINITE ELEMENT MODEL OF A CRACKED DRUM

Implementation of the inverse analysis procedure and the nodal crack force approach in a crack identification system, described in chapter 1 and section 3.3, respectively, was performed on a scaled down model of a pressure washer drum. A pressure washer drum is a large (diameter: 4-6 m, length: 6-10 m), slow rotating (1-5 rpm) drum used to separate bleaching liquor and chemicals from pulp [107,142]. In the past, drums of this type have experienced repetitive cracking in the highly stressed hub region, which lead to frequent interruptions in operation due to inspection and repair intervals. In addition, these drums represent typical machine systems operated by the pulp and paper industry as well as other heavy duty industries. Therefore, it was concluded that using the pressure washer drum as a guideline application for this study will lead to a viable crack identification solution that will be applicable to a whole range of similar industrial applications.

In order to verify the feasibility of the method, a range of crack parameters, i.e., crack size and location, must be investigated through simulation and experimental studies. At this stage in the research, this cannot be achieved by taking vibration measurements from a pressure washer drum in the field. It was concluded that the best approach would be comprised of building a scaled-down model of a pressure washer drum that may be used as an experimental model. Details of the experimental model, procedure and results are given in chapter 5 while the FE model used in the inverse analysis procedure will be described in the following sections.

4.1 3D FE model of a scaled-down pressure washer drum

A FE model of the scaled-down pressure washer drum experimental setup was built using the commercial FE code ANSYS [140]. For this purpose, the drum was divided into seven components: drum shell, two endplates, two hub and two shaft sections. A graphic display of the FE model is shown in Figure 4.1. Shaft and hub components were

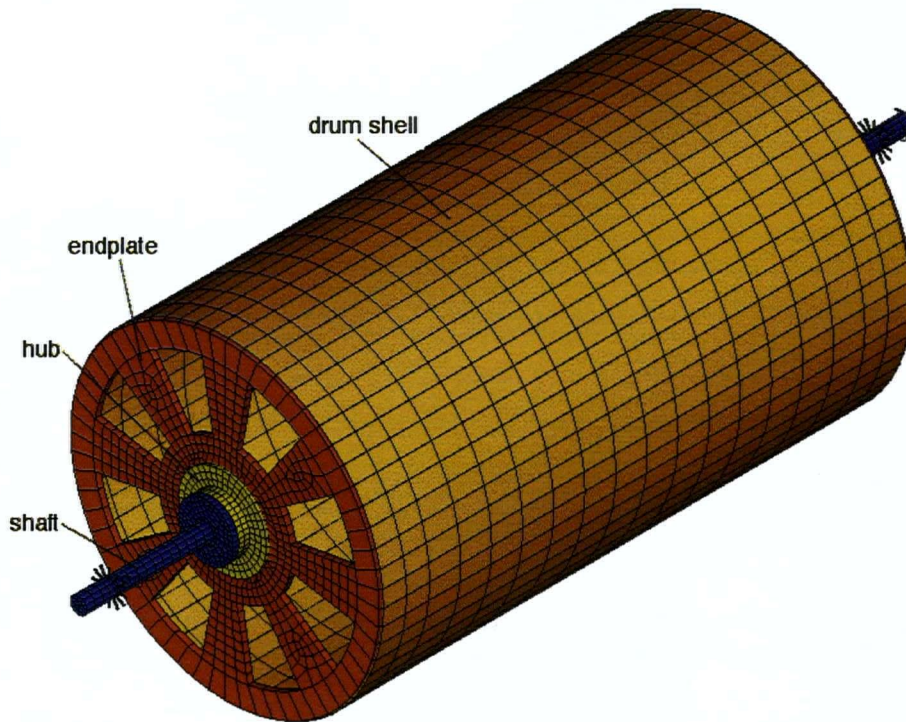


Figure 4.1: 3D FE model of the pressure washer drum.

modeled using eight-noded 3D solid brick elements while endplates and drum shell components were modeled using four-noded 3D shell elements. A detailed account of the element and material properties for each section may be found in Appendix A.1. The complete model consisted of approximately 4700 elements and 7700 nodes resulting in 28000 DOF.

The drum was subjected to gravity loading applied as acceleration body force vector. The mass of the bolts were simulated by nodal mass elements. These elements simply added the mass of a single bolt to the node at that location without adding to the FE model stiffness. Additionally, the forces applied by the loading frame were modeled as concentrated nodal forces at twelve points on the drum shell. Applied forces are listed in Figure 4.2. The support points were modeled using linear spring elements to provide stiffness in the axial and radial direction and with respect to angular bending.

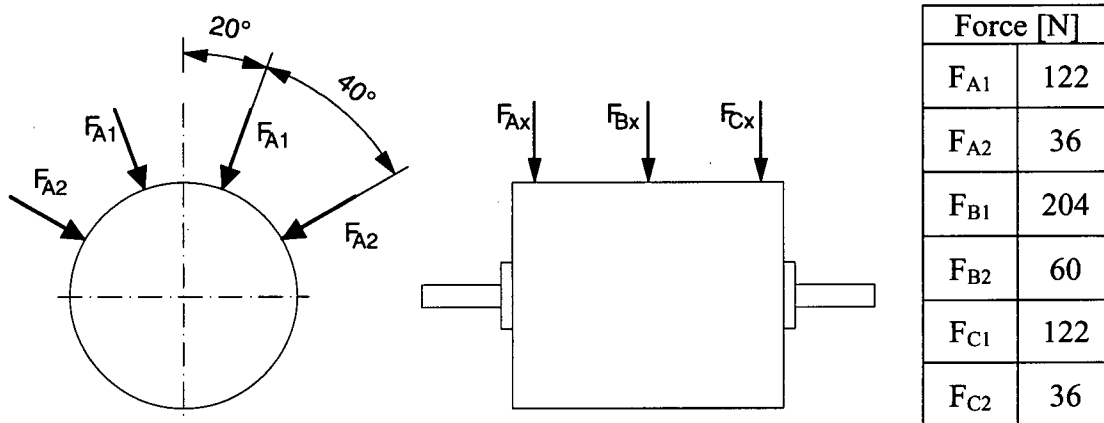


Figure 4.2: Applied nodal forces to 3D drum FE model.

The spring element configuration is shown in Figure 4.3. Spring elements were located such that they provide an equal stiffness in any radial direction. Two rotational spring elements were used to provide the angular stiffness in bending about the x and y -axis. To transfer the rotational spring stiffness onto the 3D solid shaft elements, a rigid plate, comprised of 3D shell elements, was placed into the shaft cross-section at the support application points.

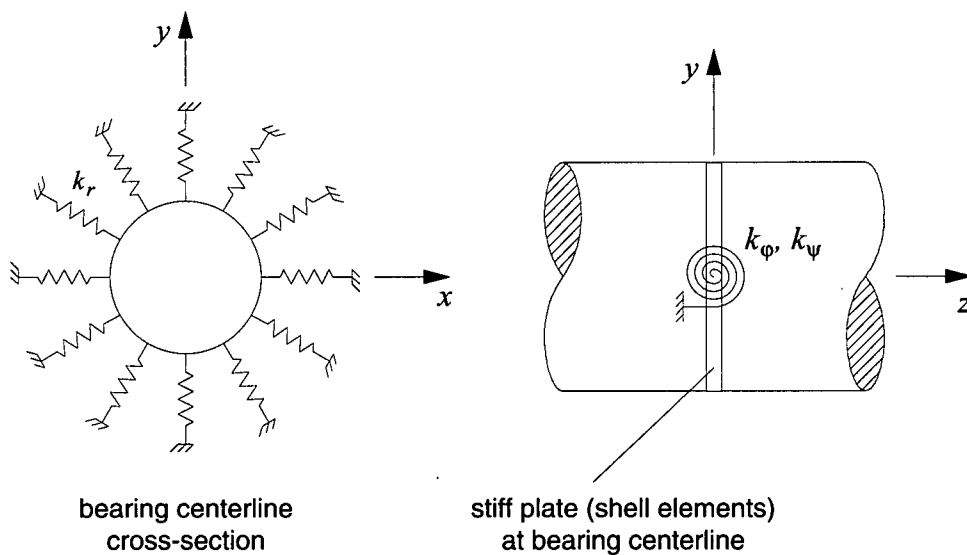


Figure 4.3: Modeling of bearing stiffness.

The spring stiffness constants, k_r , k_ϕ and k_ψ , were determined through stiffness measurements of the pillowblock bearings used in the experimental setup; see Appendix A.2. For the angular bending stiffness the resulting non-linear spring stiffness function was approximated using ANSYS' multi-linear spring elements resulting in a non-linear analysis procedure for the drum's initial static deflection.

A crack was incorporated into the model through the de-coupling of double nodes at the component interfaces, as explained in section 3.3. Components had been selected such that their interfaces matched the proposed crack locations of the experimental setup. The FE model was parameterized in such a way that a crack of arbitrary size could be placed at any of the proposed locations by specifying two parameters: crack size α , where: $0^\circ \leq \alpha < 360^\circ$, and location L , where: $L = 1, \dots, 6$; see Figure 4.4. Here, the integer parameter L refers to the proposed crack location starting from the drive side of the drum.

The 3D FE model of the scaled-down pressure washer drum was verified by comparing computed and measured values of static deflection and first lateral natural frequency for the uncracked drum model to those from the experimental setup. Results, listed in Table 4.1, show that both, static deflection and natural frequency, measured and computed values are within 15 % of each other, which proves the validity of the 3D FE model.

	3D FE model	Experimental measurements
Natural frequency (bending)	35 Hz	30 Hz
Static deflection	400 μm	440 μm

Table 4.1: Comparison of natural frequency and static deflection between 3D FE model and experimental measurements.

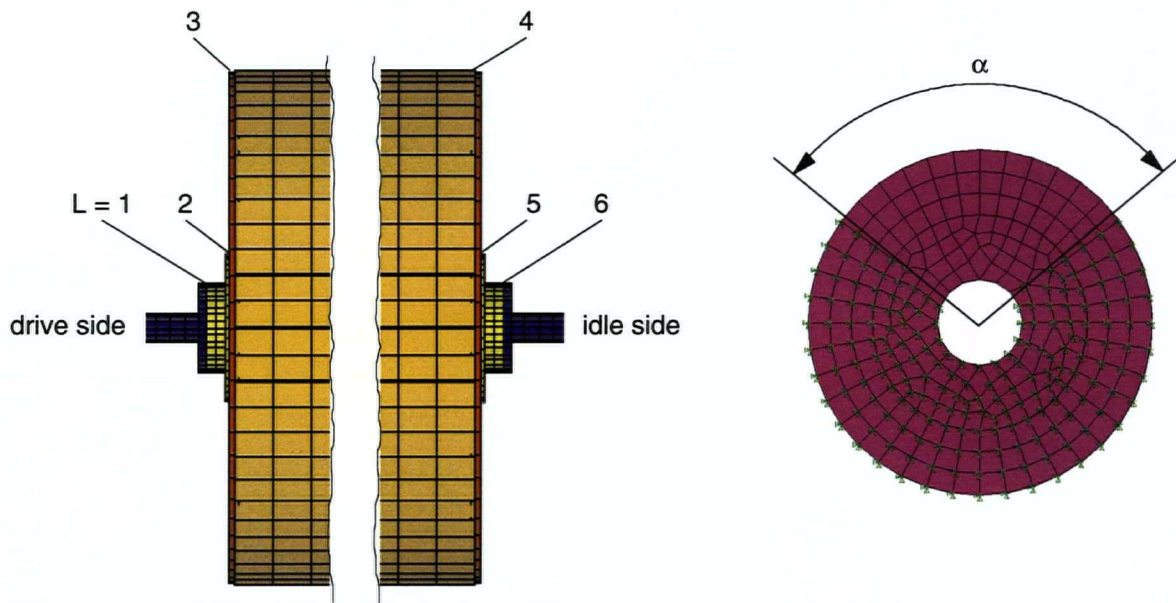


Figure 4.4: Definition of crack location parameter L and crack size parameter α .

4.2 FE analysis procedures

The vibrations of the pressure washer drum were computed using the nodal crack force approach, explained in section 3.3, and two quasi-static approaches where the crack breathing is controlled by the stress distribution of the uncracked structure and through contact elements at the crack surfaces. The two later methods serve as a comparison to the performance of the nodal crack force approach.

4.2.1 FE analysis using the nodal crack force approach

In the nodal crack force approach, the computation of the final solution was performed in three stages, as shown in Figure 4.5. In the first stage, the uncracked FE model was analyzed quasi-statically over one full revolution in increments of angle of rotation of $\Delta\Omega t = 15^\circ$. The discrete nodal coupling forces of all double nodes at the proposed crack locations were recorded at every angle of rotation. The nodal coupling forces for three exemplary nodes are shown in Figure 4.6. In stage two, the recorded nodal coupling

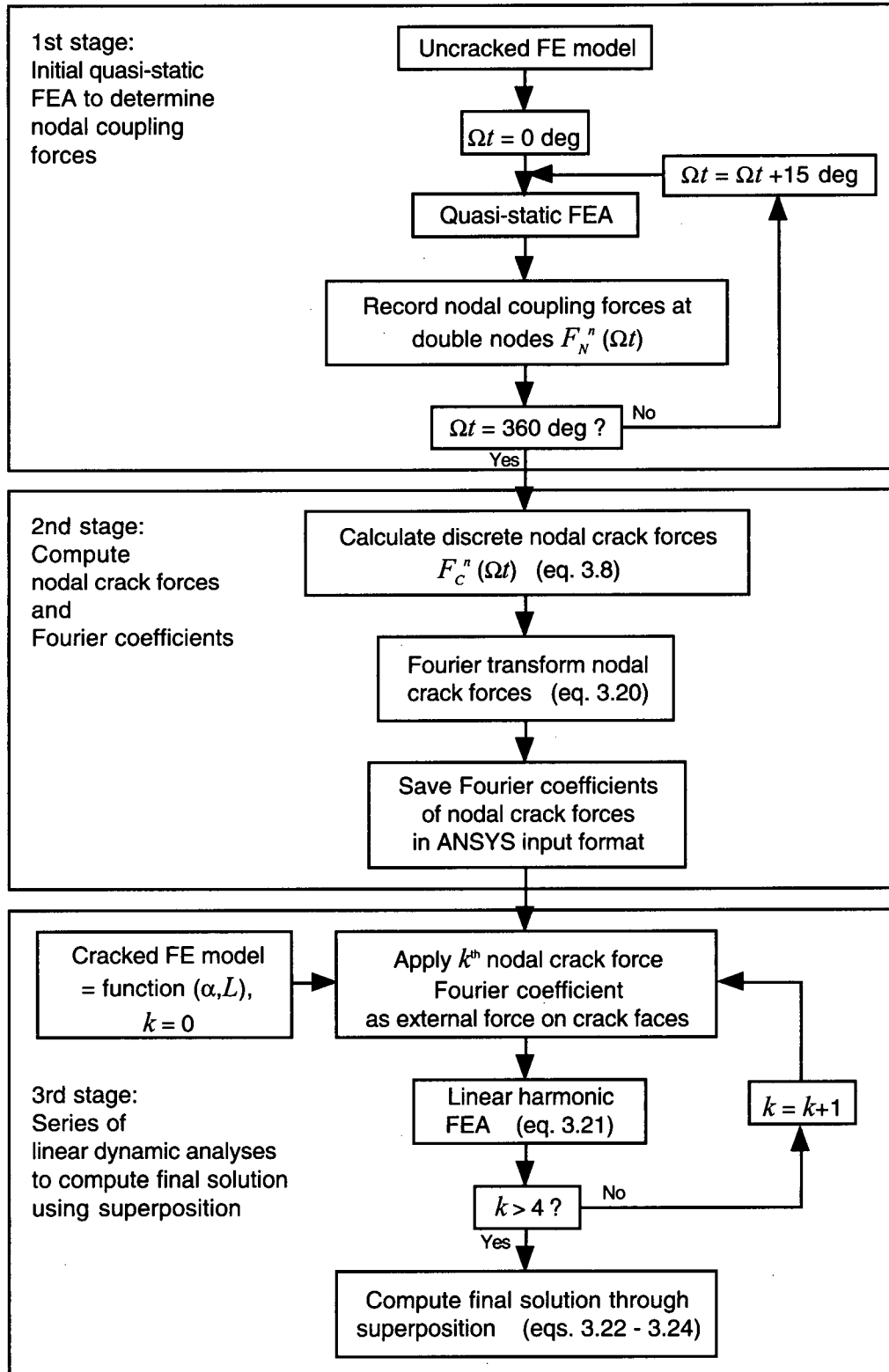


Figure 4.5: Flow chart for the nodal crack force approach.

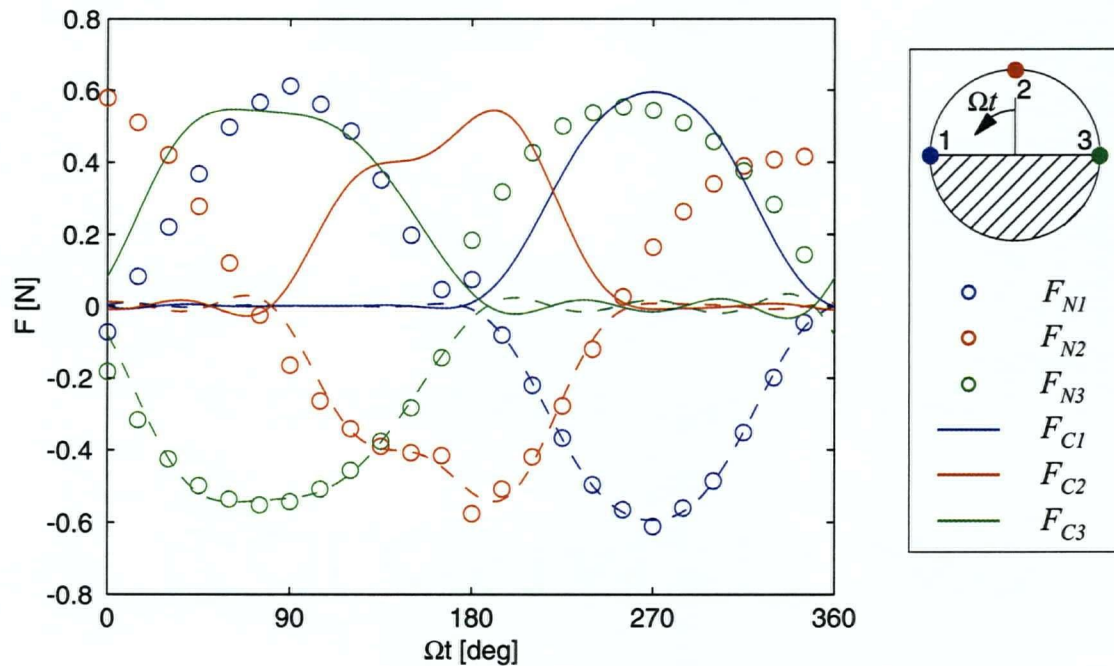


Figure 4.6: Nodal coupling forces (F_N) and Fourier transformed nodal crack forces (F_C) for three different points along the circumference.

forces were used to compute the discrete nodal crack forces using equation (3.8), which in turn were Fourier transformed. The first five Fourier terms were considered and transformed to applied loads in ANSYS format for the subsequent linear dynamic analysis. The cracked FE model used in stage three is essentially identical with the initial uncracked FE model. However, the elements of the individual components were combined to superelements [140] yielding only seven superelements to model the drum plus 32 additional spring elements to model the support bearings.

Employing superelements resulted in a significantly smaller FE model size (≈ 300 DOF), which in turn allows a much quicker solution of the FE equations. The double nodes at the component interface were coupled, analogue to the uncracked model, except at the crack face nodes where the nodal crack forces were applied instead. Which of the interface nodes is a crack face node was determined by the crack parameters α and L . A series of linear harmonic analyses in a rotating coordinate system was performed for each

of the applied Fourier coefficients and the final solution was obtained using superposition (eqs. 3.21-3.22) and transferring the displacement back to stationary coordinates (eq. 3.23).

As noted in section 3.3.2, the great advantage of the nodal crack force approach lies in the fact that for any subsequent evaluation of the vibration solution for different parameters only stage three of the analysis process must be repeated. This is true for as long as the steady state uncracked solution remains valid, i.e., the drums operating conditions such as rotational speed or applied load will not change significantly. Since stage three represents five linear harmonic analyses of the much reduced superelement drum model, the computational requirements for re-evaluating a different crack size are minimal.

4.2.2 FE analysis with crack breathing controlled by nominal stress distribution

Due to the slow rotational velocity of the drum, $\Omega/\omega_n < 1\%$, inertia effects can be safely ignored. Therefore, it is possible to obtain the cracked drum displacement through quasi-static analysis at various angles of rotation. In this approach, it is assumed that crack breathing is controlled by the dominant static deflection of the uncracked drum and the decision whether the crack will be open or closed will depend on its relative position to the nominal neutral axis. This means, crack face double nodes above the neutral axis will be coupled, while those below will be uncoupled and the crack is free to open; see Figure 3.3. Due to the non-linear spring elements for the bearing supports, the procedure results in a series of non-linear static analyses for different angles of rotation in increments of $\Delta\Omega t = 30^\circ$.

4.2.3 FE analysis using contact elements at the crack faces

When investigating the mechanics of the breathing crack mechanism, it becomes apparent that the neutral axis of the cracked cross-section is shifted upward compared to that of an uncracked cross-section. This affects the crack breathing behaviour in

particular for partially open cracks. Under pure vertical loading and when the crack centerline lies at $\Omega t = 90^\circ$ the crack will not exactly be half open and half closed. Instead, portions of the crack lying in the nominally compressive region will also open; see Figure 4.7. This phenomenon has been verified through 3D FE simulation by Schmalhorst [52] and is particularly significant for large cracks ($a/D > 0.4$).

In order to evaluate the effect of the described shift in the neutral axis, analysis of the drum model was also performed using contact elements at the crack faces determining the crack breathing behaviour. The contact elements consisted of bilinear springs connecting the crack face double nodes. The spring stiffness was very high in the compressive region to resist penetration of the crack surfaces while being very low in the tensile direction to allow the crack faces to gap. Otherwise the drum model was analyzed using the same quasi-static procedure described in the previous section.

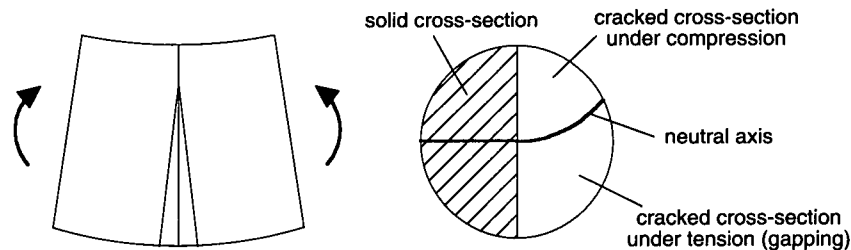


Figure 4.7: Upward shift of the neutral axis for partially open crack.

4.3 FE results

Horizontal and vertical vibration results for various crack sizes at location 6 for all three FE models are shown in Figures 4.8 to 4.10. Nodal values of displacement were taken at the shaft's centerline at vibration pick-up locations 1 and 2; see Figure 5.1. In the graphs, for instance Δx_1 refers to the horizontal vibration computed at point 1 while Δy_2 refers to the vertical vibration computed at point 2 with respect to the point of uncracked static deflection. All graphs show qualitatively the expected behaviour due to crack breathing.

The vertical deflection increases when the crack opens at $\Omega t = 90^\circ$, reaches its maximum at $\Omega t = 180^\circ$ and returns to the point of uncracked static deflection after the crack closes again at $\Omega t = 270^\circ$. Quantitatively the peak vertical deflection for the two quasi-static methods are very close. This was to be expected since in this position the crack is completely open. The 20 % greater vertical deflection from the nodal crack force approach is due to the approximation of the nodal crack forces by a Fourier series and due to the linearized spring stiffness used when modeling the support bearings.

A similar picture may be found when examining the horizontal deflection. Qualitatively all methods show the drum swinging to one side as the crack opens at $\Omega t = 90^\circ$, returning to zero at $\Omega t = 180^\circ$ and then swinging to the other side before returning back to the point of uncracked static deflection at $\Omega t = 270^\circ$. However, the quantitative analysis shows a significant difference between the nodal de-coupling method and the other two approaches. For large crack sizes the peak horizontal deflection from the nodal de-coupling method lies approximately 50 % below the results using contact elements or the nodal crack force approach. The reason for this behaviour lies in the upward shift of the neutral axis for the partially open crack, which occurs when the horizontal deflection experiences its peak values, i.e., $\Omega t = 135^\circ$ and 225° . Figure 4.11 shows how for a large crack of $\alpha = 180^\circ$ the crack faces will open early, i.e., before passing the horizontal axis, thus causing a greater horizontal deflection. On the other hand, when using the node de-coupling method, this region is assumed closed, thus its nodes are coupled, which adds a fictitious stiffness to the structure resulting in a smaller horizontal and vertical deflection. The nodal crack force approach is also based on this assumption to compute the nodal crack forces. However, in the harmonic analysis step, the stiffness of the structure is based on the fully cracked model and is therefore not adding any artificial stiffness to the problem. Hence, the results from the nodal crack force approach are comparable to those from the contact element method. It can also be seen that early crack opening does not affect smaller cracks below $\alpha \leq 90^\circ$. More detailed graphs of the crack breathing results for various crack sizes may be found in Appendix A.3.

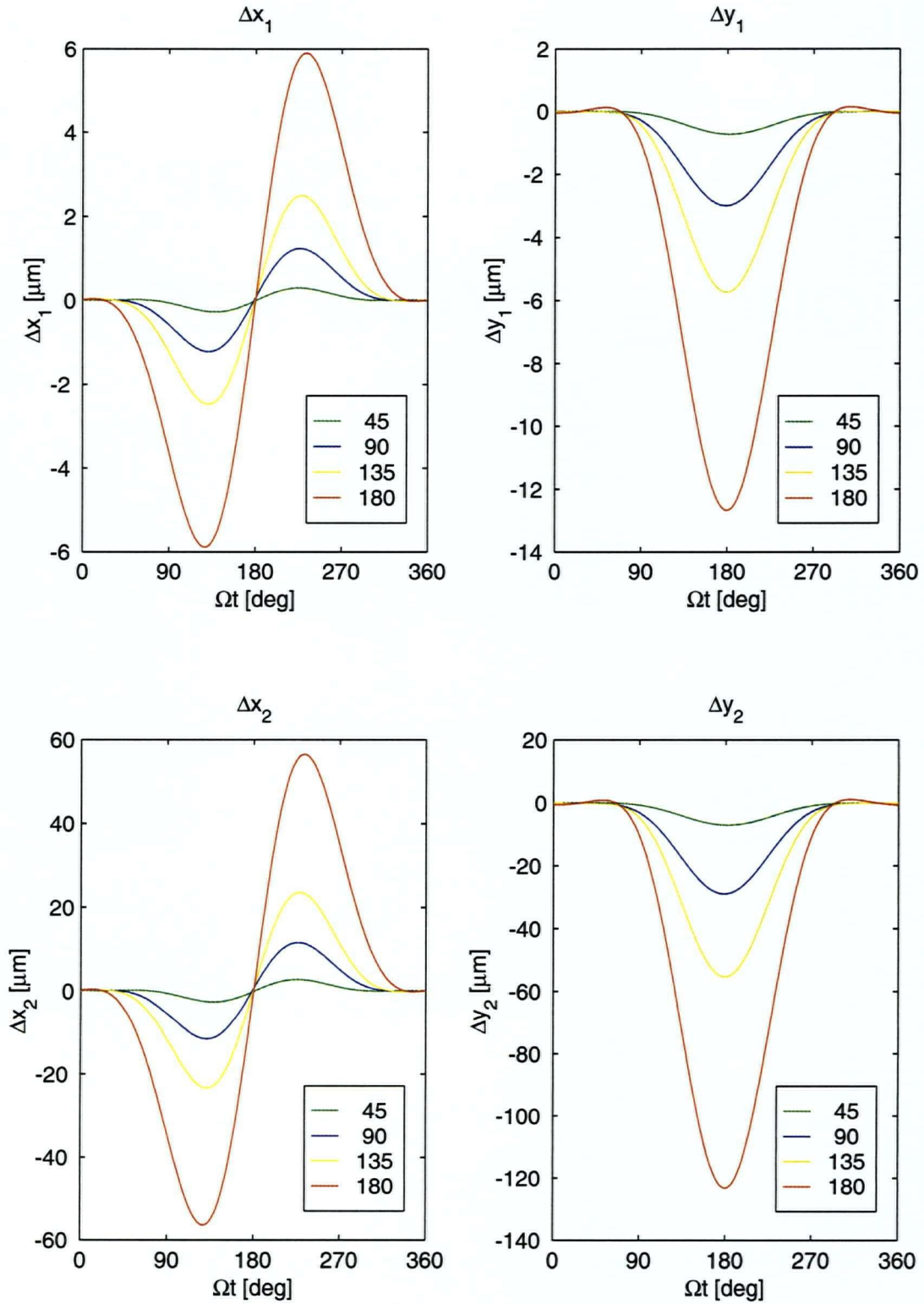


Figure 4.8: Simulated horizontal (Δx) and vertical (Δy) vibration for a crack at location 6 using the nodal crack force method (colours indicate crack size α [deg]).

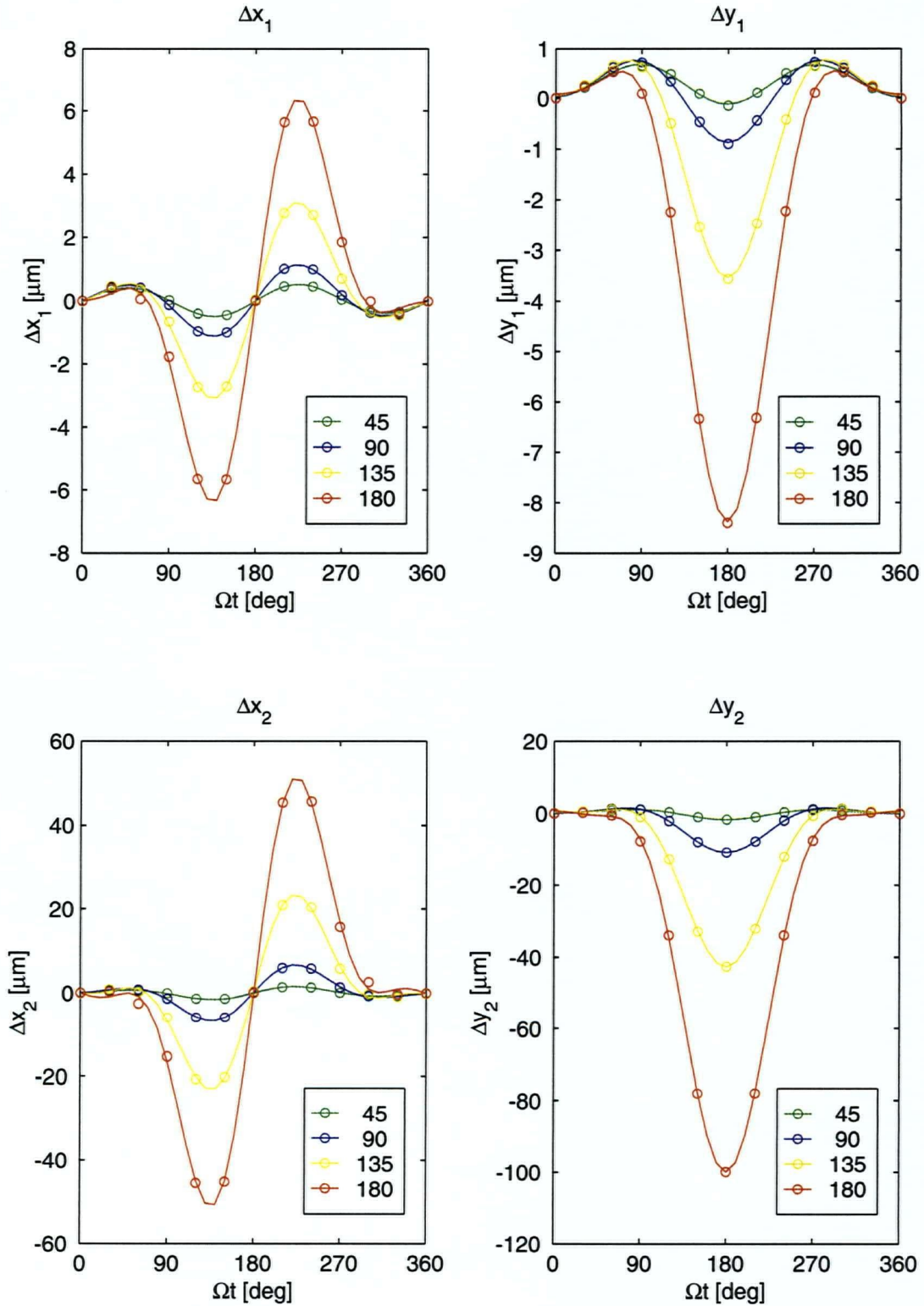


Figure 4.9: Simulated horizontal (Δx) and vertical (Δy) vibration for a crack at location 6 using contact elements at the crack surfaces (colours indicate crack size α [deg]).

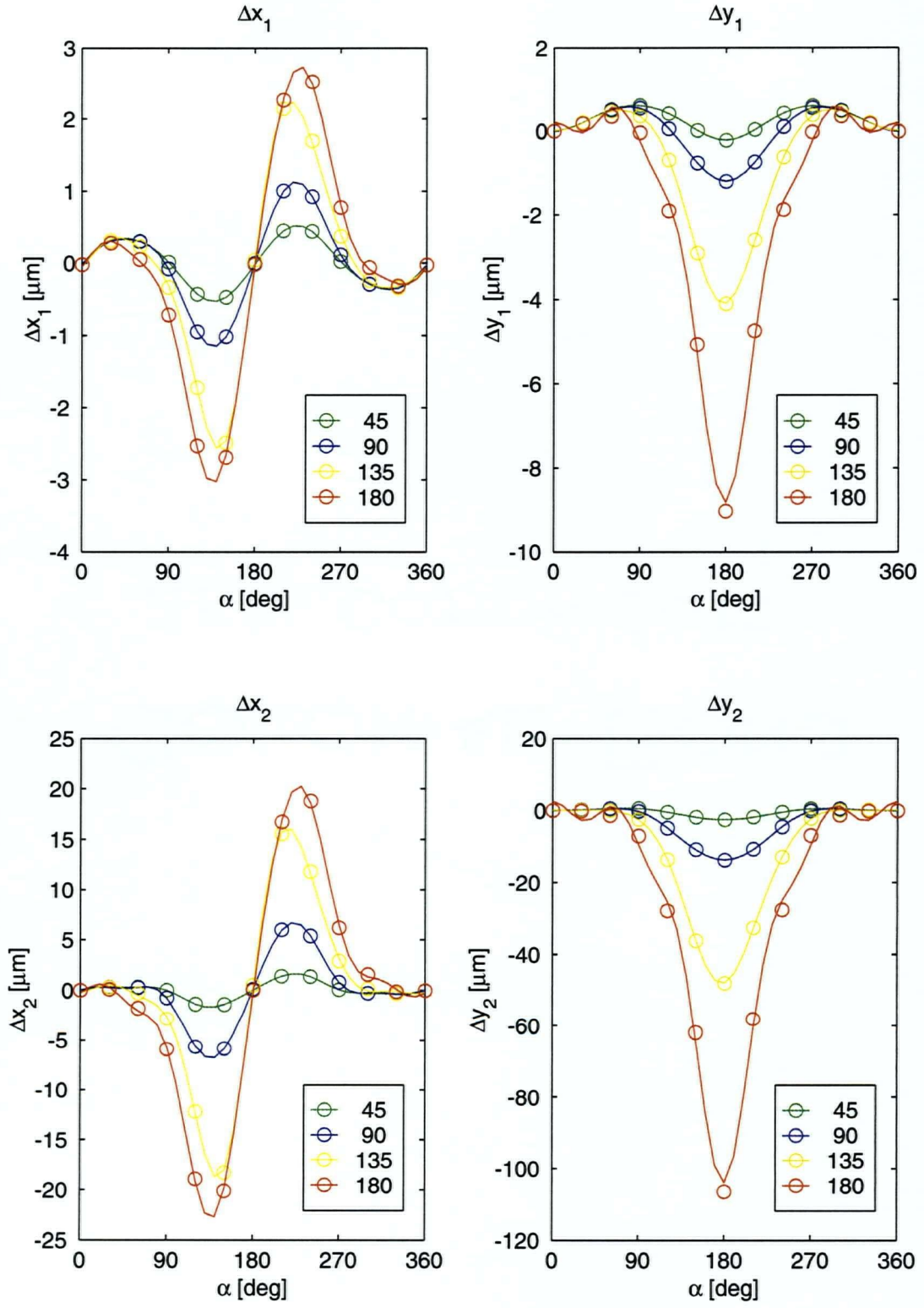


Figure 4.10: Simulated horizontal (Δx) and vertical (Δy) vibration for a crack at location 6 using the nodal de-coupling method (colours indicate crack size α [deg]).

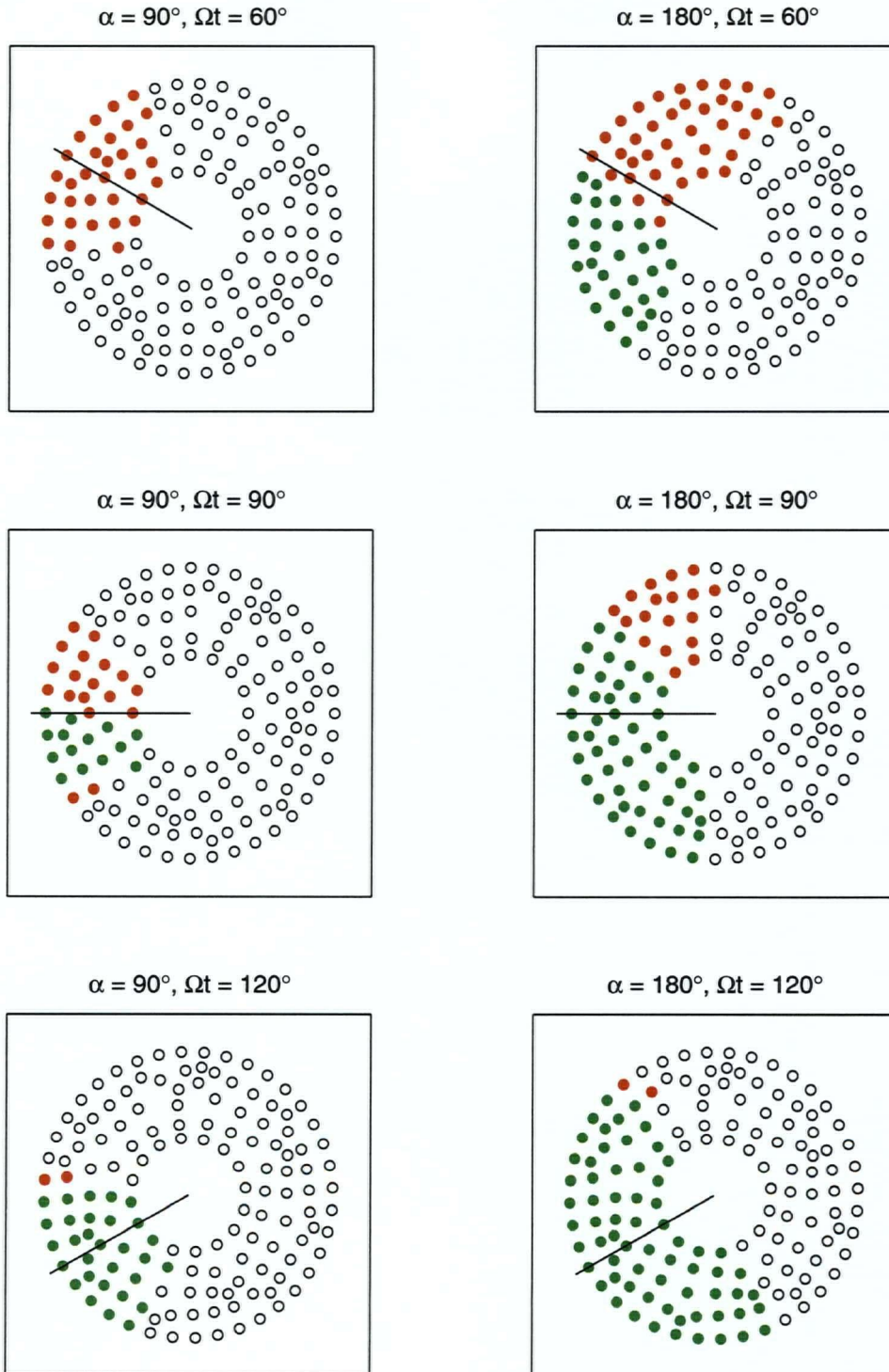


Figure 4.11: Simulated crack opening for $\alpha = 90^\circ$ and 180° using contact elements at the crack surfaces (red = compression, green = tension, black line = crack center line).

CHAPTER 5

EXPERIMENT

5.1 Experimental setup

An experimental setup was designed to simulate the vibration of a large, slow rotating, cracked rotor under load. Results from the test specimen were used to verify the FE model, to compare various experimental crack modeling techniques and to provide the experimental input for the inverse analysis procedure. The following is a description of the experimental specimen, the sensors and data acquisition (DAQ) system, and the analysis program used to analyze the recorded data.

5.1.1 Scaled-down pressure washer drum test specimen

The scaled-down pressure washer drum test specimen was designed to resemble a real pressure washer drum at a scale of 1:10. A schematic view and a photograph of the test specimen are shown in Figure 5.1. Detailed parts and assembly drawings are given in Appendix B.1. Loads and materials for the test specimen were determined through a similarity analysis which may be found in Appendix B.2.

Analogue to the FE model, the test specimen consisted of seven main components: drum shell, two endplates, two hub and two shaft pieces. All components were made of aluminium 6061-T6 except for the drum shell which was made of AISI 316 stainless steel. The overall length of the drum was 1000 mm (40 in). The shaft diameter was 19.1 mm (0.75 in), the hub diameter 64 mm (2.5 in) and the drum shell diameter 305 mm (12 in). The endplate wall thickness was 6.4 mm (0.25 in) whereas the drum shell wall thickness was 4.8 mm (0.1875 in). A total of 112 1/4-UNC cap screws were used to bolt the individual components together over the circumference: eight at the shaft-hub intersection, twelve at the hub-endplate intersection and 36 at the endplate-drum intersection at each end.

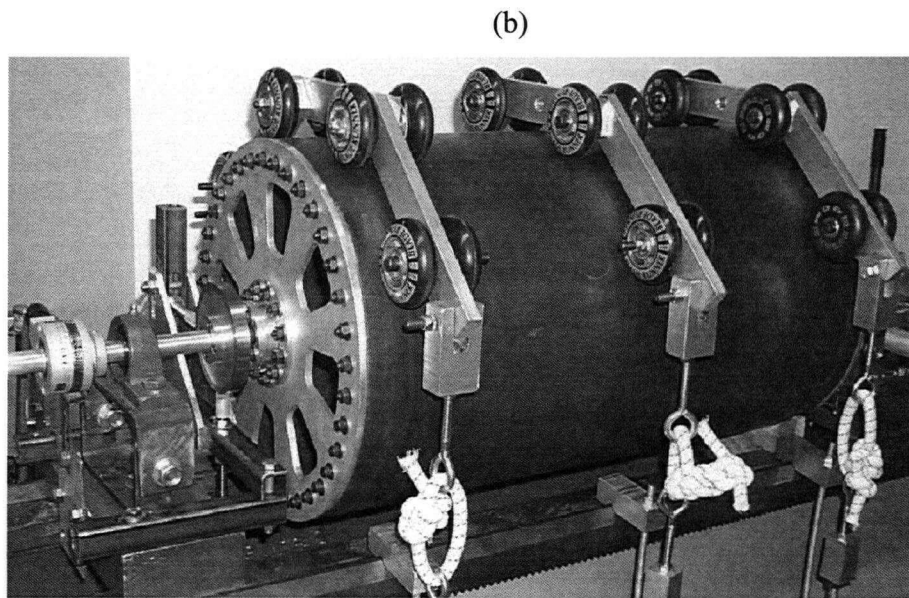
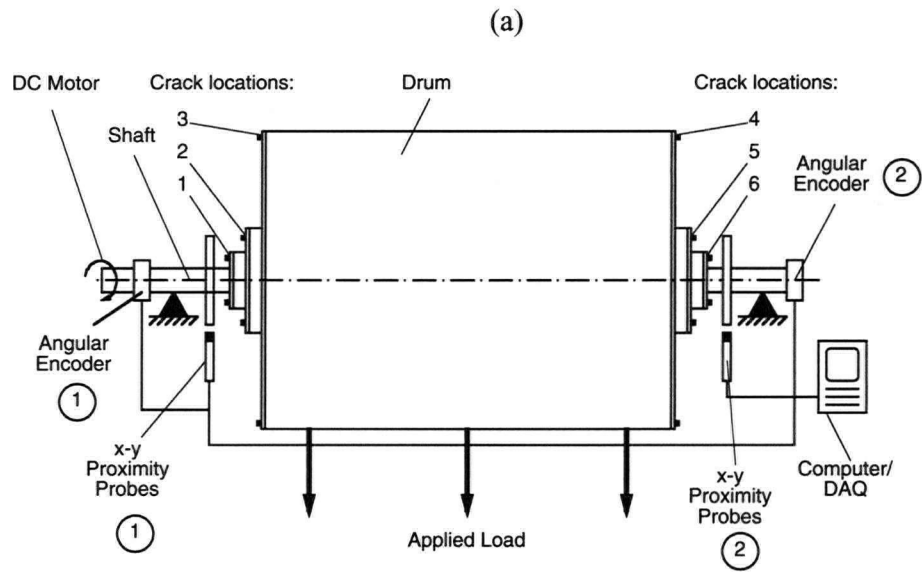


Figure 5.1: Schematic view (a) and photograph (b) of pressure washer drum experimental setup.

The drum was supported by two self-aligning pillow block roller bearings. The free span of the drum between the bearing centerlines was 900 mm (35.4 in). The bearings were mounted on steel support blocks which in turn were mounted on a lathe bed acting as a rigid base for the experimental setup. The drum was actuated by a 0.28 kW (0.375 hp) electric DC motor and a worm gear drive with a speed reduction ratio of 1:65. The motor speed was controlled by an infinitely variable voltage supply providing the 0-90 V drive voltage.

The drum was loaded through three specially designed loading frames in order to simulate the pulp pressure acting on a real pressure washer drum. The frames consisted of three aluminium plates which were loosely bolted together. The connecting bolts and two additional bolts on the sides were held in place by lock nuts and acted as axis for rubber wheels which pushed on the drum in the radial direction while allowing it to rotate freely. The frames were loaded by mounting weights on one end of the frame while constraining the other to the lathe bed. Hence, the applied load was transferred as radial force through the wheels onto the drum. Tangential force creating a torque could be applied by fastening the lock nuts, thus the resulting friction would hinder the free rotation of the wheels. The applied weights were attached to the loading frames through an elastic rope acting as a buffer spring regulating the load and keeping it independent of the motion of the drum. The applied load was 267 N (60 lbs) through the two outside loading frames and 445 N (100 lbs) through the center loading frame resulting in a total applied load of 979 N (220 lbs) in the vertical direction including the weight of the loading frame.

5.1.2 Vibration sensors, signal conditioning and data acquisition

Vibration measurements on the drum were performed using two types of sensors: non-contacting proximity probes to measure the lateral shaft deflection and angular encoders to measure the torsional drum vibration as well as to supply an angular position reference signal of the drum. Signals from all sensors were fed into a signal conditioning unit and subsequently into a DAQ board driven by a Labview [143] DAQ program. Sensor and DAQ equipment specifications are listed in Appendix B.3.

Horizontal and vertical vibrations at both ends of the drum were measured using four non-contacting eddy-current proximity probes (Bently Nevada 3300XL). The probes function by creating an electric field over the probe head and sensing the electric field strength which is dependent on the distance of an electric conductor to the probe head. The result is a voltage output signal between 0-22 V approximately proportional to the probe range of 0-2 mm (0-0.08 in). Since the minimum shaft diameter for a probe to operate reliably is 75 mm (3 in) and the probes work only poorly when sensing aluminium, two extension wheels of 100 mm (4 in) in diameter, were placed at the vibration pick-up points on either side of the drum. The wheels, with a core made of aluminium, were mounted on the shaft by a set screw. A ring of 4140 steel was press-fit to the outside. 4140 steel was chosen based on the probe manufacturer's recommendation to achieve accurate and reliable measurements. The probes were held in place by a steel fixture mounted on the lathe bed at a distance of 50 mm (2 in) away from the support bearing centerline. The supply voltage was provided by a constant voltage circuit driven by a rechargeable 24 V battery. The constant voltage circuit ensured that the supply voltage remained at a constant level independent of the charge state of the battery.

Even though the proximity sensors exhibit an almost linear response over the range of interest, a calibration curve for each sensor was recorded to convert the voltage signal to physical units at high accuracy. Points on the calibration curve were taken at an interval of 12.7 μm using a micrometer as a target for the proximity probe. Each calibration point resulted from an average of 100 samples. Intermediate points were linearly interpolated. The results were implemented as a Matlab [144] function allowing easy and accurate conversion from measured voltage signal to physical quantity.

Two optical angular encoders (BEI-HS25F) were mounted on the drive end and the idle end of the shaft, outside the two support bearings. The encoders were used to measure the angular position of the shaft as well as the torsional vibration. The encoders were driven by a 5 V supply voltage and their output signals were two 0-5 V pulse waves per encoder at a resolution of 1024 pulses per revolution. Each pulse consists of two voltage steps that

were individually counted by the DAQ system. The two pulse waves, which were phase shifted by a quarter period, were fed into an exclusive OR (XOR) gate thus the resolution for each encoder was doubled to 4096 steps per revolution or 0.088° per step. Additionally, both encoders supplied a once per revolution pulse which was used as trigger signal for the DAQ unit.

Signal conditioning of the vibration voltage signal was performed in two stages. First, the voltage was attenuated by a simple voltage divider circuit since the sensor output voltage was 0-22 V, but the DAQ board (IOTech Daqboard 2000) only supported an input voltage of 0-10 V. The voltage divider circuit was designed such that the dividing ratio was user-selectable at 1:1, 3:1 or 3:2 to make optimal use of the actual voltage output. The attenuated signal was then fed into a hardware low pass filter, featuring a Butterworth filter with a cutoff frequency of 5 Hz, in order to remove high frequency noise from the signal.

The filtered signal was converted by a 16-bit analogue to digital converter and recorded on a Pentium 166 MHz computer with 80 MB of RAM. The pulse signals from the angular encoders were counted and converted cumulatively to form a measure for the current angle of rotation. A flow chart of the signal conditioning and data acquisition process is shown in Figure 5.2.

The program controlling the data acquisition process was written in Labview [143,145]. Its core consisted of the data acquisition module for the DAQ card supplied by the card manufacturer. Data recording was triggered by the 1/rev. pulse signal from encoder 1 (drive side). All four analogue signals from the proximity sensors and the pulse count from both encoders were then sampled at a frequency of 100 Hz and stored in memory. Data sampling took place for a total of five complete revolutions of the drum. The sampled data was recorded by taking the average of ten consecutive sampled data points for each sensor and storing the result into an experimental data file.

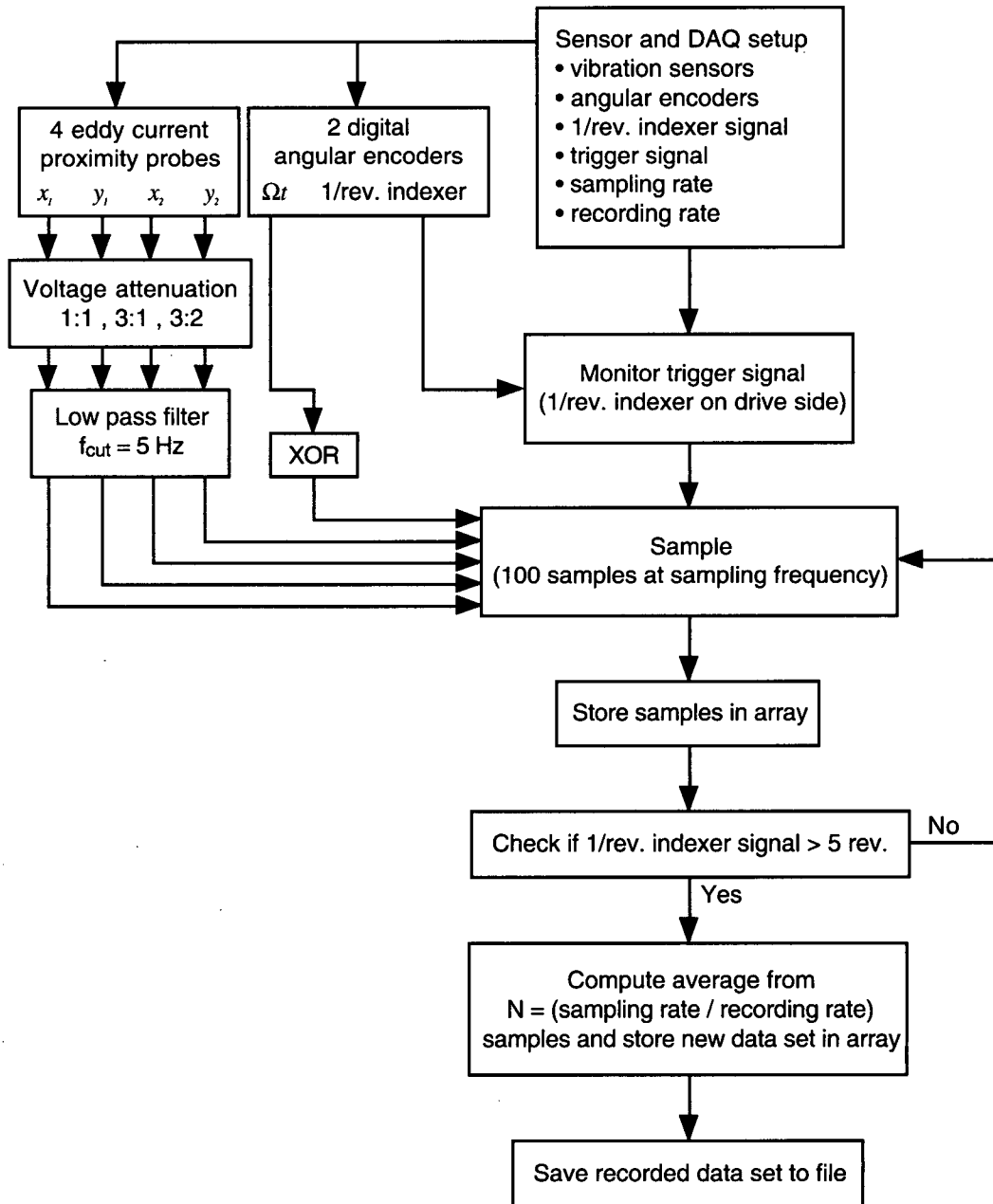


Figure 5.2: Flow chart of the signal conditioning and data acquisition (DAQ) process.

5.1.3 Experimental data analysis program

An experimental data analysis (EDA) program was written in Matlab [144] to analyze and graphically display the experimental results. A flowchart of the EDA program is shown in Figure 5.3. The stored data file (ASCII format) by the DAQ program is read by the EDA program and the recorded sensor signals are converted into physical units using the previously recorded calibration curves. Since the exact rotational speed of the drum was not constant over the five recorded revolutions, the discrete points of the vibration signals, even though recorded at equidistant points in time, do not lie at equidistant points of angle of rotation. Therefore, the measured points are transformed by linear interpolation based on the recorded signal of angle of rotation from encoder 1 to equidistant points along the Ωt -axis. This transformation is necessary for the subsequent averaging and Fourier analysis procedure.

The transformed signal is now parsed into the five separate revolutions and an averaged solution for one revolution is computed. Finally, Fourier analysis is applied to the averaged signal using Matlab's *fft* function resulting in the Fourier coefficients for the averaged signal. The Fourier coefficients, header information as well as many intermediate results are stored in binary form as analyzed and converted data files that serve as the basis for subsequent processing and evaluating of experimental results.

The second stage of the EDA program serves as an easy tool to evaluate and graphically display the recorded data. The Fourier coefficients are passed through a low pass filter and compared to a reference signal which had been previously recorded and processed in analogue manner. The time-domain signal is reconstructed and graphically displayed for visual evaluation of the experimental data. Cutoff frequency and reference signal may be varied easily, allowing a quick evaluation of important frequency components and comparison between vibration signals from different crack parameters.

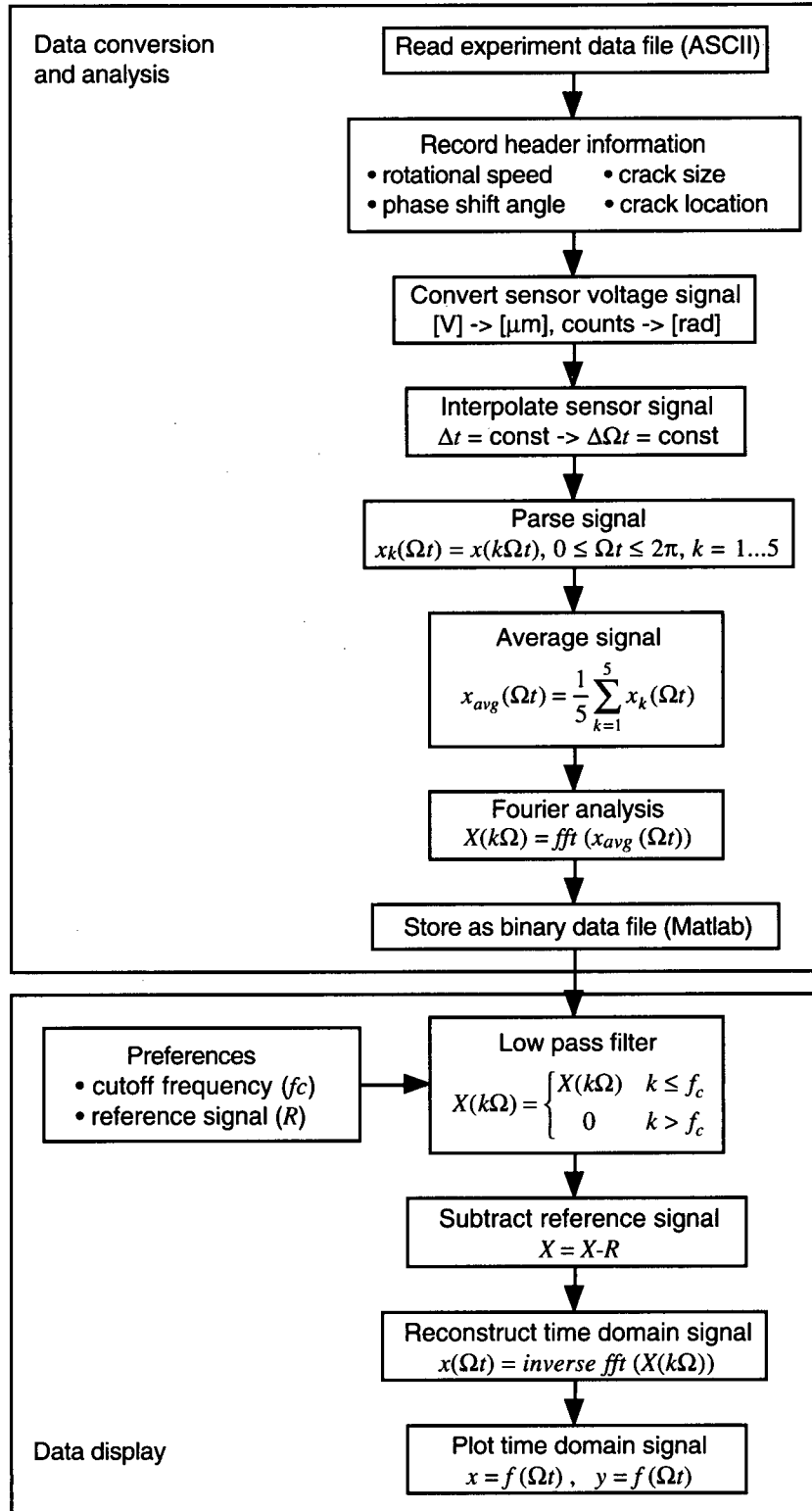


Figure 5.3: Flow chart of experimental data analysis (EDA) program.

5.2 Experimental crack modeling

The difficulties involved in growing a fatigue crack of predetermined size at a specific location in a structure have been discussed in section 2.3. Two alternative methods were introduced: the bolt removal method [42,100] and the gap insertion method [58,59].

While it must be recognized that neither of the proposed alternatives offers an accurate experimental model for a grown fatigue crack, their advantages with respect to cost, time involvement and flexibility in the crack parameters are enormous, especially for the bolt removal method. Also, since the investigated quantities are not local stresses or deformation around the crack tip but global deflection of the rotor measured at points far away from the crack, it is conceivable that bolt removal and gap insertion method will yield quantitatively comparable results to a real fatigue crack, as has been proposed by Ishida [58,59], Tamura et al.[100] and Liao and Gasch [42]. Hence, the usage of either of these methods will yield tremendous cost and time savings in a large-scale parameter study investigating the influence of the crack size and location on the vibration of a cracked drum. Therefore, the current study will investigate a quantitative comparison of vibration signals using all three experimental crack models at one of the proposed crack locations in the drum and will proceed with further experiments using the method that promises to be most effective for the large-scale parameter study.

5.2.1 Bolt removal method

The bolt removal method used to experimentally simulate the non-linear vibration behaviour of a cracked rotor was introduced by Tamura et al. [100]. It is based on the assumption that any suitable mechanism that simulates the full compressive stiffness of the uncracked structure, while allowing gapping of the cracked region under tensile load, will yield a vibration pattern comparable to that of a cracked structure. In the case of the bolt removal method the connection between two separate rotor pieces is achieved through connecting bolts located around the circumference of the structure. Figure 5.4 shows the hub region design of the drum using the bolt removal method. Six connecting bolts (1/4 UNC) are distributed equally at an angular distance of 45° over the circumference. To simulate a crack, the appropriate number of bolts is removed from the

circumference, allowing the two parts to separate under tensile load in that region. It is obvious that the bolt removal method lends itself to model cracks in stepped cross-sections and shafts of large diameter. Therefore, it seemed particularly advantageous for usage in the drum model. The drum was designed such that the bolt removal method might be applied at all proposed crack locations, i.e., shaft-hub, hub-endplate and endplate-drum shell intersections. All crack locations, number of connecting bolts and resulting crack sizes are listed in Table 5.1. The exact definition of the crack size when using the bolt removal method is explained in Figure 5.5. Instead of defining the crack size through the ratio of crack length to diameter a/D , the crack angle α is used, which was introduced by Gasch [30] to define cracks in hollow cylinders. Here, α is defined by the midpoint along the radial centerline between the last connecting bolt and the first removed bolt. With this definition there is a unique relation between α and a/D :

$$\frac{a}{D} = \frac{1}{2} - \frac{(D_{inner}/D)+1}{4} \cos(2\alpha) \quad (5.1)$$

However, in this study the crack angle is used as a measure for crack size because of its intuitive connection to the number of removed bolts.

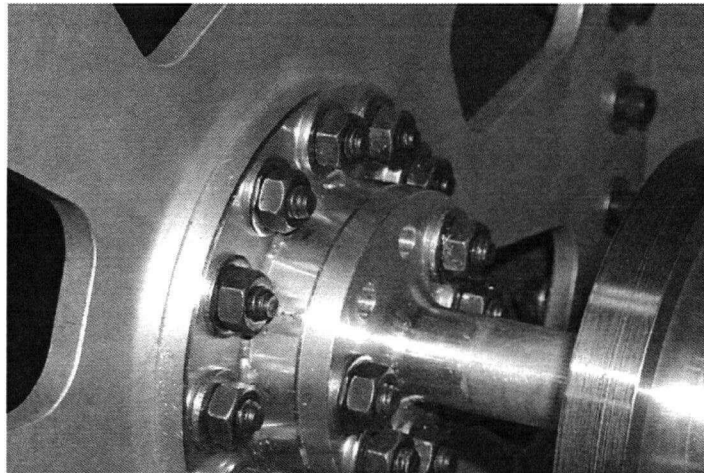


Figure 5.4: Simulating a crack at the inner hub location by removing two bolts from the circumference.

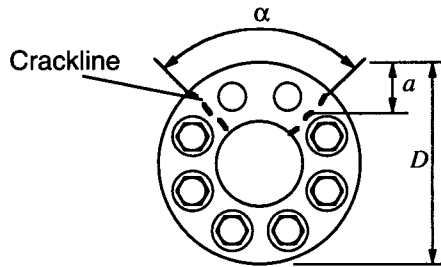


Figure 5.5: Definition of crack size parameter α for the bolt removal method.

Bolts removed	α [deg]		
	Inner Hub ($L=1,6$)	Outer Hub ($L=2,5$)	Drum ($L=3,4$)
1	45	30	-
2	90	60	20
3	135	90	-
4	180	120	40
5	225	150	-
6	-	180	60
7	-	200	-
8	-	-	80
10	-	-	100
12	-	-	120
14	-	-	140
16	-	-	160
18	-	-	180
20	-	-	200

Table 5.1: Investigated crack sizes for simulation cracks using the bolt removal method.

5.2.2 Gap insertion method

For the gap insertion method, a slot was created at the inner hub location using a circular cutter. The slot width was 0.5 mm. A thin aluminium plate was manufactured to act as an insertion and was placed in the saw cut. The plate was hand-filed such that it created a snug fit when inserted into the gap. Figure 5.6 shows the slotted shaft and the inserted aluminium plate and lists the slot sizes. A total of four slot sizes were investigated. A technical drawing of the specimen used in the gap insertion method is shown in Appendix B.4.

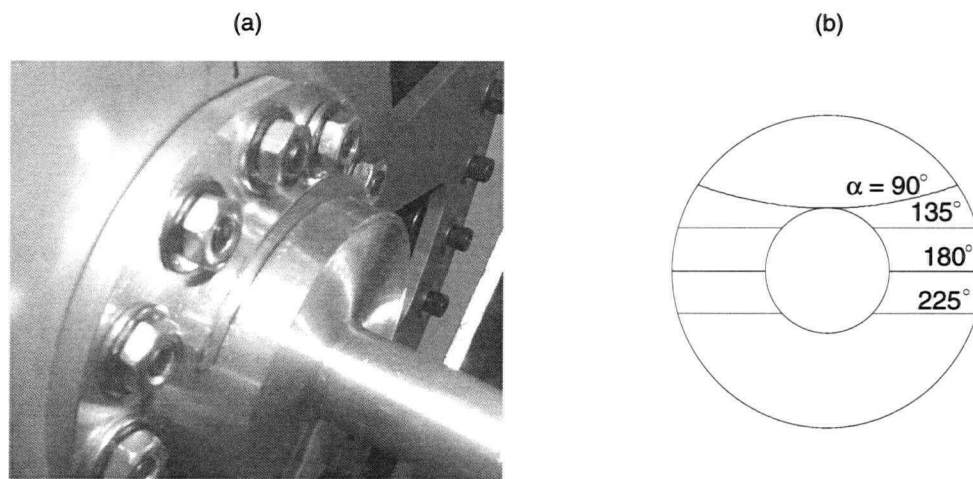


Figure 5.6: (a) Slotted hub with insertion. (b) Slot sizes α for gap insertion method.

5.2.3 Real fatigue crack

In order to place a grown fatigue crack into the shaft-hub component, the specimen was first fatigued on a hydraulically activated material testing system (MTS). A photograph of the MTS with the mounted shaft-hub specimen is shown in Figure 5.7(a). Instead of fatiguing the specimen in its final shape, a raw specimen of 108 mm (4 in) diameter and 40 mm (1.57 in) flange thickness was used. A photograph of the raw specimen is shown in Figure 5.7(b), detailed drawings are provided in Appendix B.5. The main advantages of using the raw specimen was to ensure that the propagating crack would grow in a self similar manner through the cross-section. The specimen was slotted in two steps to a

minimum diameter of 66 mm (2.6 in) and a slot width of 3.5 mm (0.14 in). The interior of the specimen was drilled out from one side with a diameter of 24 mm (0.95 in) and a depth of 66 mm (2.6 in) extending to the cross-section of the outside slot. The stress concentration was then amplified by placing a straight-fronted saw cut at the bottom of the slot using a handsaw with a blade width of 0.3 mm (0.012 in).

The specimen was mounted offset from the load centerline of the MTS in order to create a dominant bending load case driving the crack propagation. The saw cut was positioned at the point of highest tensile stress. The applied load was cycled between $F_{\max} = 5000$ N (1124 lbs) and $F_{\min} = 100$ N (22.5 lbs) resulting in an approximated stress intensity factor (SIF) of $\Delta K_I = 300$ MPa $\sqrt{\text{mm}}$ (8.6 ksi $\sqrt{\text{in}}$), greater than the threshold SIF of $\Delta K_{I\text{th}} = 150$ MPa $\sqrt{\text{mm}}$ (4.3 ksi $\sqrt{\text{in}}$) but below the critical SIF of $\Delta K_{I\text{cr}} = 915$ MPa $\sqrt{\text{mm}}$ (26.3 ksi $\sqrt{\text{in}}$). Threshold and critical SIF had been estimated from values in the literature [15] and from a previous calibration experiment fatiguing a 25.4 mm (1 in) thick aluminium 6061-T6 plate with a through thickness crack. The load was cycled at a frequency of 1 Hz and crack initiation was achieved after approximately 72000 cycles, equivalent to 20 hours.

Crack propagation was monitored using dye-penetrant and an optical microscope mounted to the MTS fixtures. The microscope provided an optical zoom of 1:20 and allowed the observation of the opening and closing of the crack throughout the fatigue test. It also provided a good estimate of the current size of the fatigue crack. The dye-penetrant was used to verify the estimated crack size in places that could not be reached using the microscope, such as the crack propagation at the interior hole. Once the crack had propagated to the proposed size, the specimen was unmounted and machined to its final dimensions; see Figure 5.7(c) and (d). A 6.5 mm (0.25 in) thick outside flange containing the bolt holes remained for later use when failing the specimen after vibration measurements were complete. The final specimen containing the fatigue crack was assembled into the drum and vibration measurements were taken as described in section 5.3.

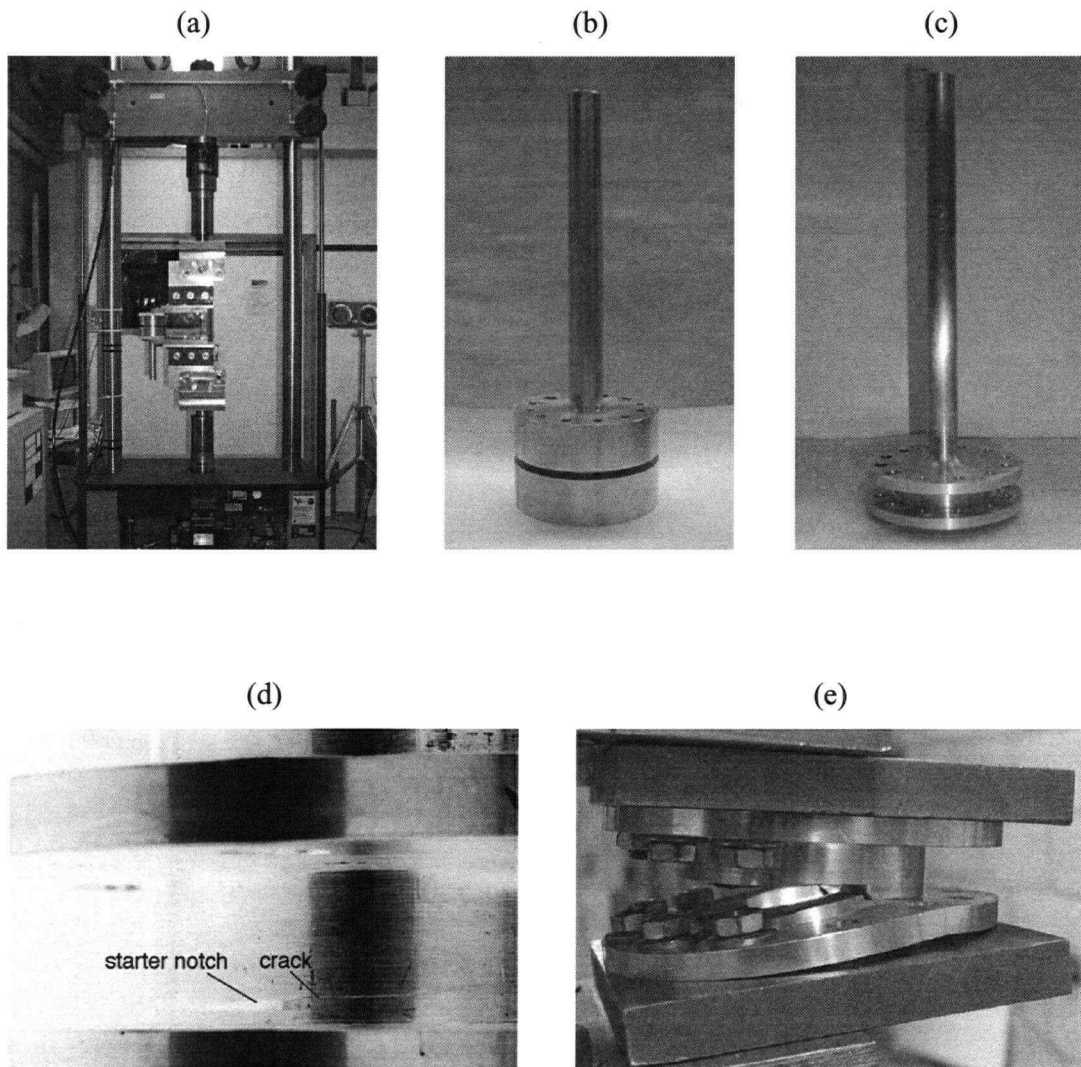


Figure 5.7: (a) Material testing system with mounted specimen, (b) raw fatigue crack specimen, (c) finished fatigue crack specimen, (d) fatigue crack in finished specimen (colours are inverted to make crack more visible), (e) failed specimen after vibration measurements were complete.

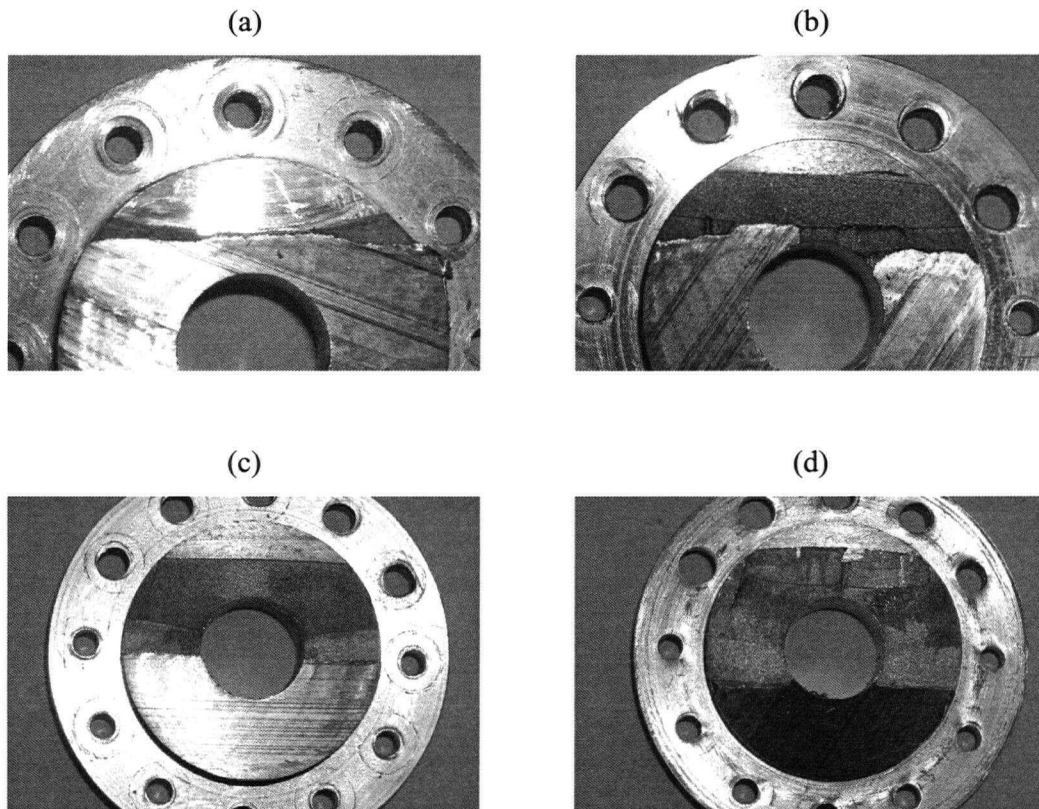


Figure 5.8: Exposed crack surfaces after complete failure of fatigue crack specimen for estimated equivalent crack sizes $\alpha = 81^\circ$ (a), 112° (b), 180° (c) and 220° (d).

Subsequently, the specimen was disassembled from the drum, remounted in the MTS and failed through static overload. In all cases, failure occurred at the cross-section containing the fatigue crack, thus exposing the fatigue crack surfaces. It was now possible to verify the final fatigue crack size during the vibration measurements by inspection of the failed cross-section. A photograph of a failed specimen is shown in Figure 5.7(e). Since the specimens were failed after each vibration measurement, a new specimen had to be manufactured for every investigated crack size. The four investigated fatigue crack specimens and their exposed crack surfaces are shown in Figure 5.8.

5.3 Experimental procedure

For all specimens, experiments were conducted in the following manner. The specimen in question was assembled into the drum. A static deflection measurement was taken from the two vertical displacement pick-up points to establish a zero deflection point. The load was applied and the vertical static deflection was measured again, yielding the uncracked static reference deflection. Next, the drum was rotated and the DAQ program was started. The DAQ program recorded data for a total of five revolutions, as described in section 5.1.2, for the uncracked drum in order to establish a reference vibration signature. The drum was stopped and the appropriate number of bolts was removed from the planned crack location. The drum was rotated again and the DAQ program recorded data in the same manner as before. When data recording was completed, the drum was stopped and unloaded. The above described process represented the taking of one vibration measurement for one set of parameter combinations.

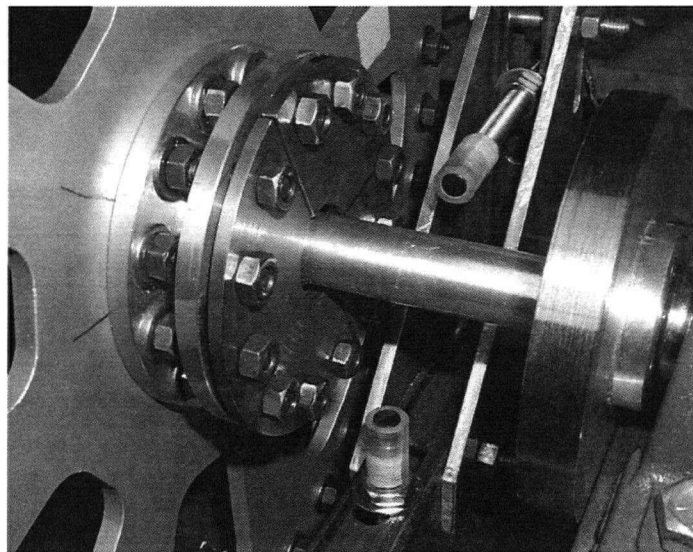


Figure 5.9: Fastening plate used to provide reference vibration signature for gap insertion method and fatigue crack specimens.

Since it was obviously not possible to provide a reference vibration signature for those specimens that had been permanently damaged during their preparation, i.e., specimens for the gap insertion and the grown fatigue crack method, a reference signature had to be created otherwise. A specially designed support plate was used to clamp the damaged cross-section together when taking the reference measurements for those specimens. A photograph of the mounted support plate is shown in Figure 5.9. It is assumed that the vibration signature of the cracked drum with the support plate will not be significantly different from that of the uncracked drum. This assumption was verified by measuring and comparing both vibration signatures, and they were found to be within acceptable error limits of $\pm 5 \mu\text{m}$.

5.4 Results and discussion

Recorded vibration signatures for the cracked drum using the bolt removal method are shown in Figures 5.10 to 5.12. The graphs show mean values of the differential horizontal and vertical deflection versus angle of rotation Ωt for a crack at location 6. “Differential” refers to the recorded vibration signal minus the reference signal recorded with none of the bolts removed; see Figure 5.3. Mean values are based on a set of ten recorded vibration signals for each parameter combination. In the graphs, for instance Δx_1 refers to the recorded signal from the horizontal proximity probe at sensor location 1, whereas Δy_2 refers to the vertical probe at location 2.

The qualitative shape of the deflection curves measured on the cracked side, i.e., Δx_2 and Δy_2 shown in Figure 5.10, for a simulated crack at location 6 using the bolt removal method agree with results from the previous FEA and with results published in the literature [52]. This is also true for measurements taken on the uncracked side for larger crack sizes. Quantitatively the maximum vertical deflection on the cracked side for $\alpha = 180^\circ$ and $\alpha = 225^\circ$ (four and five bolts removed) is $165 \mu\text{m}$ and $330 \mu\text{m}$ below the point of uncracked static deflection, respectively. The peak to peak value for the horizontal deflection is even greater with $220 \mu\text{m}$ for four bolts and $410 \mu\text{m}$ for five bolts

removed. A summary of maximum vertical and peak to peak horizontal deflections for all crack locations is presented in Table 5.2.

Recorded vibration signatures for a simulated crack at locations 1 to 5, which may be found in Appendix B.6, show similar behaviour as those of location 6. As was expected, symmetry in the vibration measurements on opposite sides of the drum was observed for the inner and outer hub locations, i.e., 1, 2, 5 and 6. For the two drum locations, i.e., 3 and 4, deflection curves for location 4 show reasonable results while in particular the horizontal deflection for location 3 shows an unusual behaviour. However, the measurements were considered accurate since they repeatedly showed the same results. A possible explanation may be that not all the holes along the circumference of the drum endplate intersection were lined up accurately during the manufacturing process, thus the removal of a bolt during the experiment could have caused a small change in the drum's alignment.

Method	Crack location	Horizontal deflection (peak to peak)		Vertical deflection (maximum)	
		Δx_1 [μm]	Δx_2 [μm]	Δy_1 [μm]	Δy_2 [μm]
Bolt removal	1	181	21	169	14
	2	283	60	242	13
	3	164	65	114	6
	4	78	559	49	475
	5	28	192	20	159
	6	22	218	8	167
Gap	6	24	198	16	167
Fatigue crack	6	17	138	13	162

Table 5.2: Mean values of measured peak to peak horizontal and maximum vertical deflection for $\alpha = 180^\circ$ (four bolts removed).

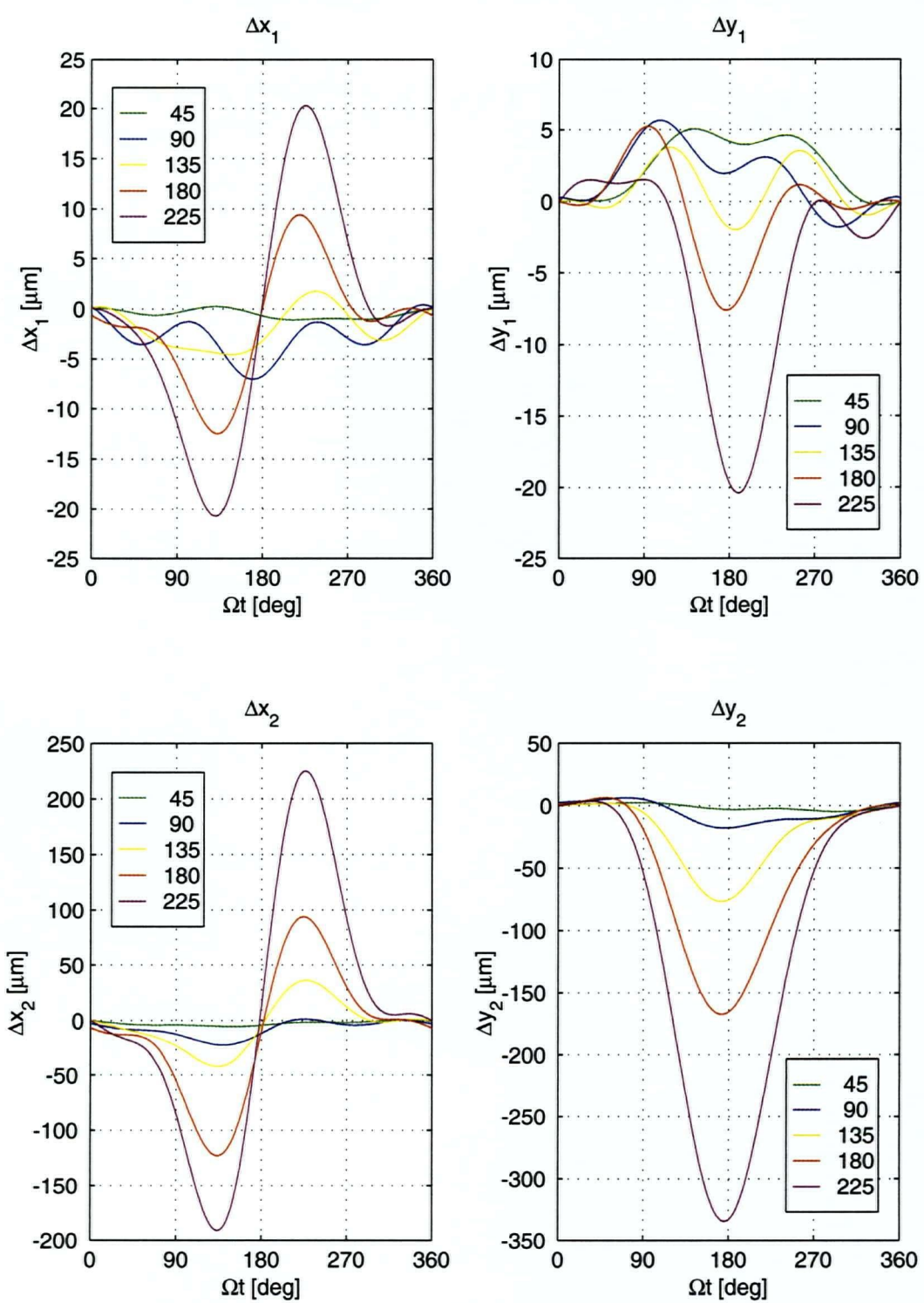


Figure 5.10: Mean values of recorded vibration signals for a simulated crack at location 6 using the bolt removal method (colours indicate crack size α [deg]).

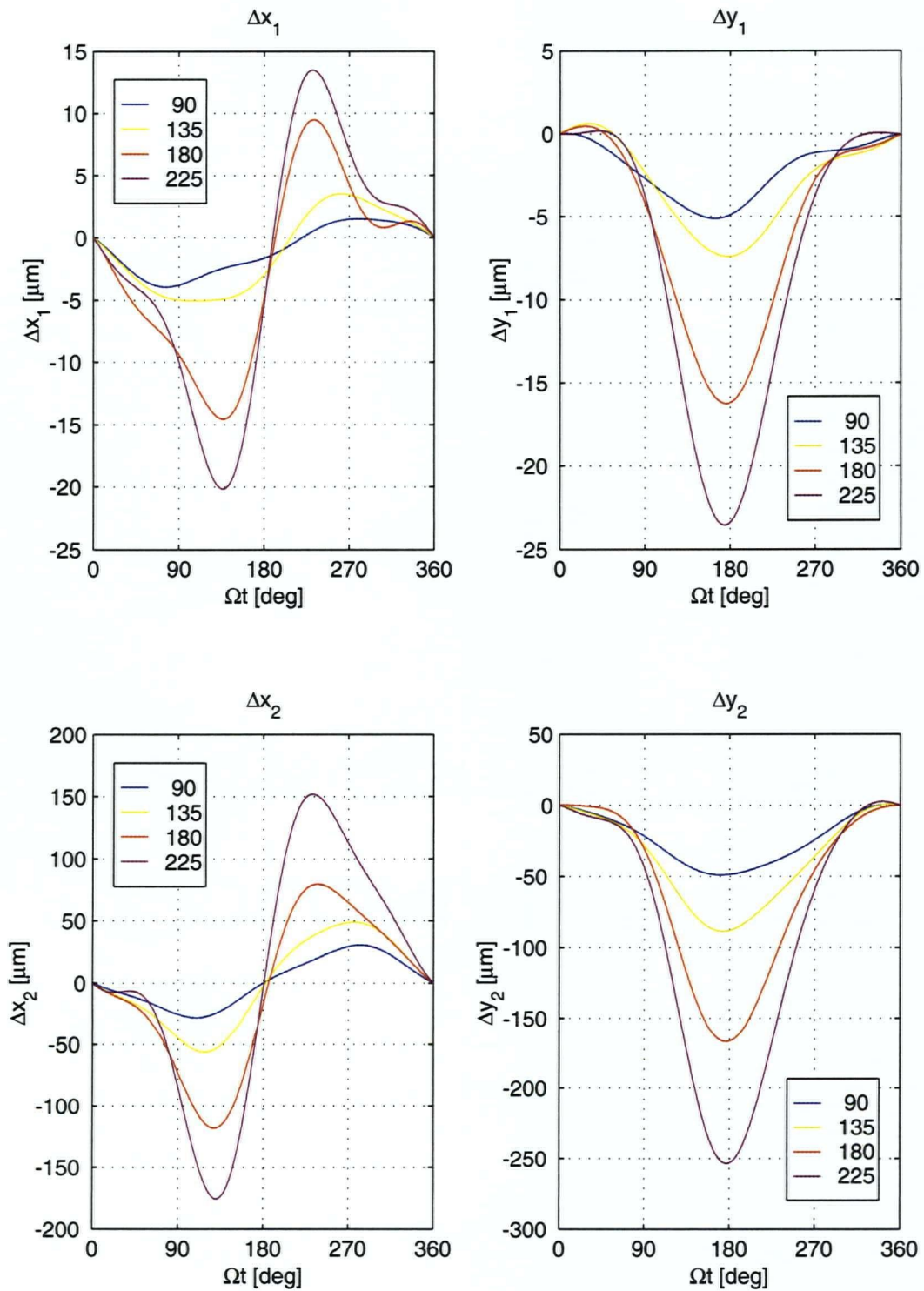


Figure 5.11: Mean values of recorded vibration signals for a simulated crack at location 6 using the gap insertion method (colours indicate crack size α [deg]).

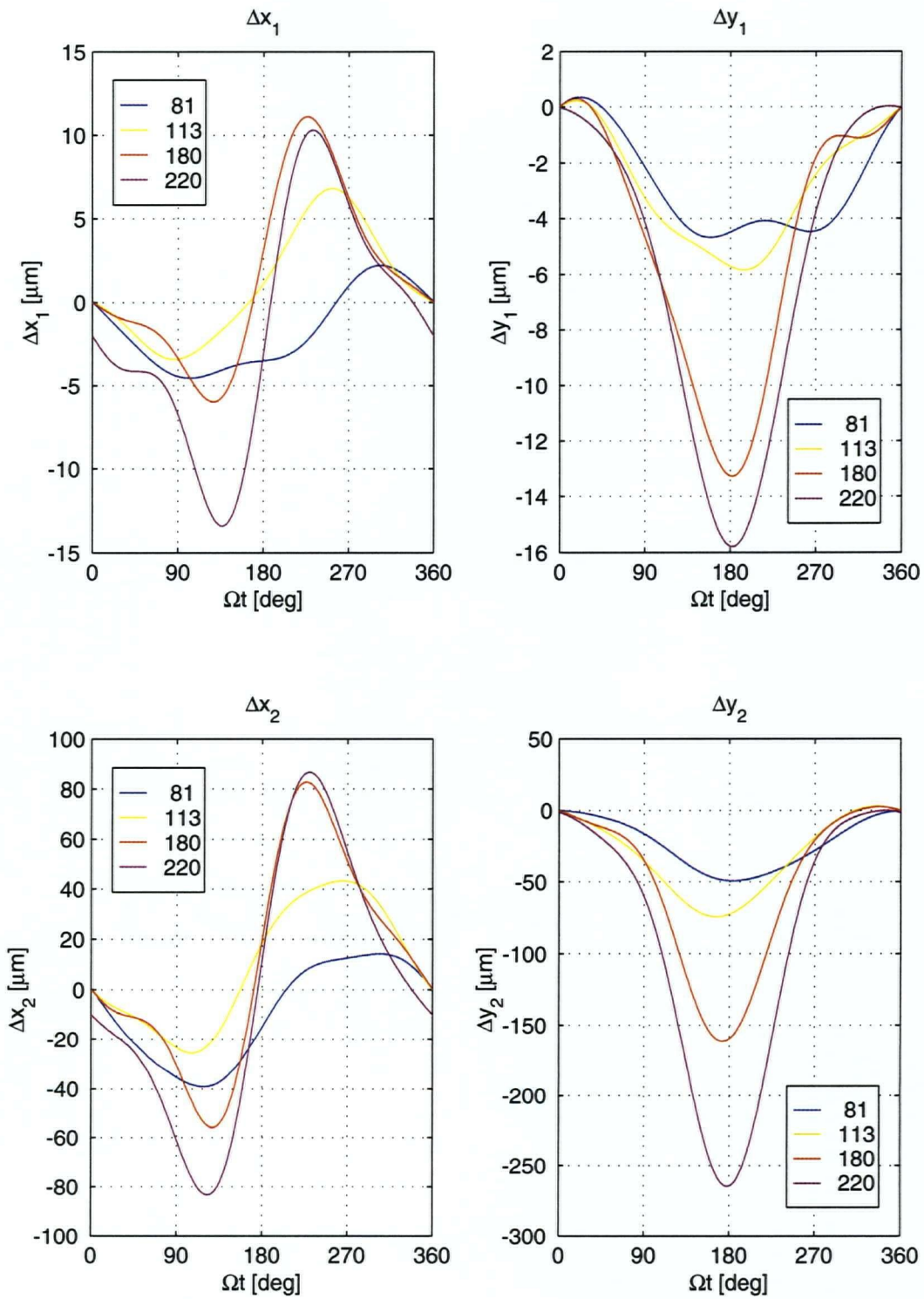


Figure 5.12: Mean values of recorded vibration signals for a fatigue crack at location 6 (colours indicate crack size α [deg]).

Nevertheless it may be said that all recorded vibration signatures using the bolt removal method show the expected key features of an existing crack: strong increase in vertical deflection at $\Omega t = 180^\circ$ and swinging from one side to the other for the horizontal deflection. The vibration amplitude shows a clear increase with increase in crack size for all cases, and results for individual crack sizes are clearly distinct, which represents a key requirement for using the vibration signature for solving the inverse problem of crack size identification. Furthermore, these features can be identified in measurements on the cracked and uncracked side. Noise dominated vibration curves measured on the uncracked side only for small crack sizes, $\alpha \leq 60^\circ$, while measurements taken on the cracked side for the inner and outer hub indicated the existence of a crack even for one removed bolt, i.e., $\alpha \leq 30^\circ$. It is also interesting to note that the peak to peak horizontal vibration is actually greater than the vertical vibration amplitude.

Mean values of the recorded vibration signal using the gap insertion method and for a real fatigue crack at location 6 are shown in Figures 5.11 and 5.12, respectively. Both graphs are in good qualitative and quantitative agreement with the results from the bolt removal method at that location. They exhibit the same features described above for the cracked and uncracked side. This proves the general validity of bolt removal method by Tamura et al. [100] to simulate the vibration of a cracked drum. However, it should be noted that the bolt removal method does overestimate the peak to peak horizontal deflection particularly for larger crack sizes. Since for large crack sizes the crack faces are only partly open at the points of maximum horizontal deflection, it is conceivable that the rough crack face surfaces of the fatigue crack offer a greater frictional force resisting the horizontal deflection. This would not be the case for the smooth crack face surfaces of the bolt removal and gap insertion method. The results also show that the vibration signature is predominately influenced by the overall size of the crack and not by the exact shape of the crack front. The crack front of the fatigue crack and the gap were oriented horizontally straight across the cracked cross-section while those of the bolt removal method were assumed to lie in the radial direction. However, it remains difficult to draw

conclusions for small crack sizes since for both, the gap insertion method and the fatigue crack, the smallest investigated crack size was approximately equivalent to $\alpha = 90^\circ$, i.e., two bolts removed.

A more detailed analysis of the vibration components may be obtained from the mean and standard deviation for the individual Fourier coefficients plotted in Figures 5.13 to 5.15. The graphs confirm the increase of the first and second harmonics with an increase in crack size, as has been reported in the literature [40,41,85]. The graphs also show that when using the bolt removal method, the vertical deflection experiences a stronger increase in the first Fourier coefficient while the horizontal deflection shows a stronger increase in the second Fourier coefficient. However, this observation is not confirmed by the gap insertion and fatigue crack methods and therefore may be considered method specific rather than a feature of the developing crack. It may also be seen that the bolt removal method provides more consistent experimental results, while the variation for the other two methods are somewhat greater. Nonetheless, errorbars indicating the standard deviation yield a clear separation of different crack sizes for all methods.

Figure 5.16 compares the first and second Fourier coefficient measured on the cracked side for all crack implementation methods. Their quantitative comparison shows good agreement with the exception of the second Fourier coefficient of the horizontal deflection, which was discussed earlier. Overall it may be noted that the bolt removal method slightly overestimates the vibration of a cracked drum while results using the gap insertion method and the real fatigue crack show excellent agreement.

In summary the following points may be concluded:

- Experimental results of the vibration of a slow rotating drum containing a fatigue crack or a simulated crack using the gap insertion method or the bolt removal method showed the key features for the existence of a crack known from the literature.

- Results from the gap insertion and the bolt removal method showed very good agreement with results from a fatigue crack, with the bolt removal method slightly overestimating the horizontal vibration of the drum.
- Measured deflection curves were consistent and repeatable for all three methods and the deflection curves for different crack sizes were clearly distinguishable from one another.
- Based on these results, the bolt removal method by Tamura [100] may be considered a valid approach to simulate the vibration behaviour of a cracked rotor. This represents a significant advantage when conducting an experimental parameter study since it results in an enormous economic benefit due to the avoidance of having to grow a real fatigue crack in the structure.

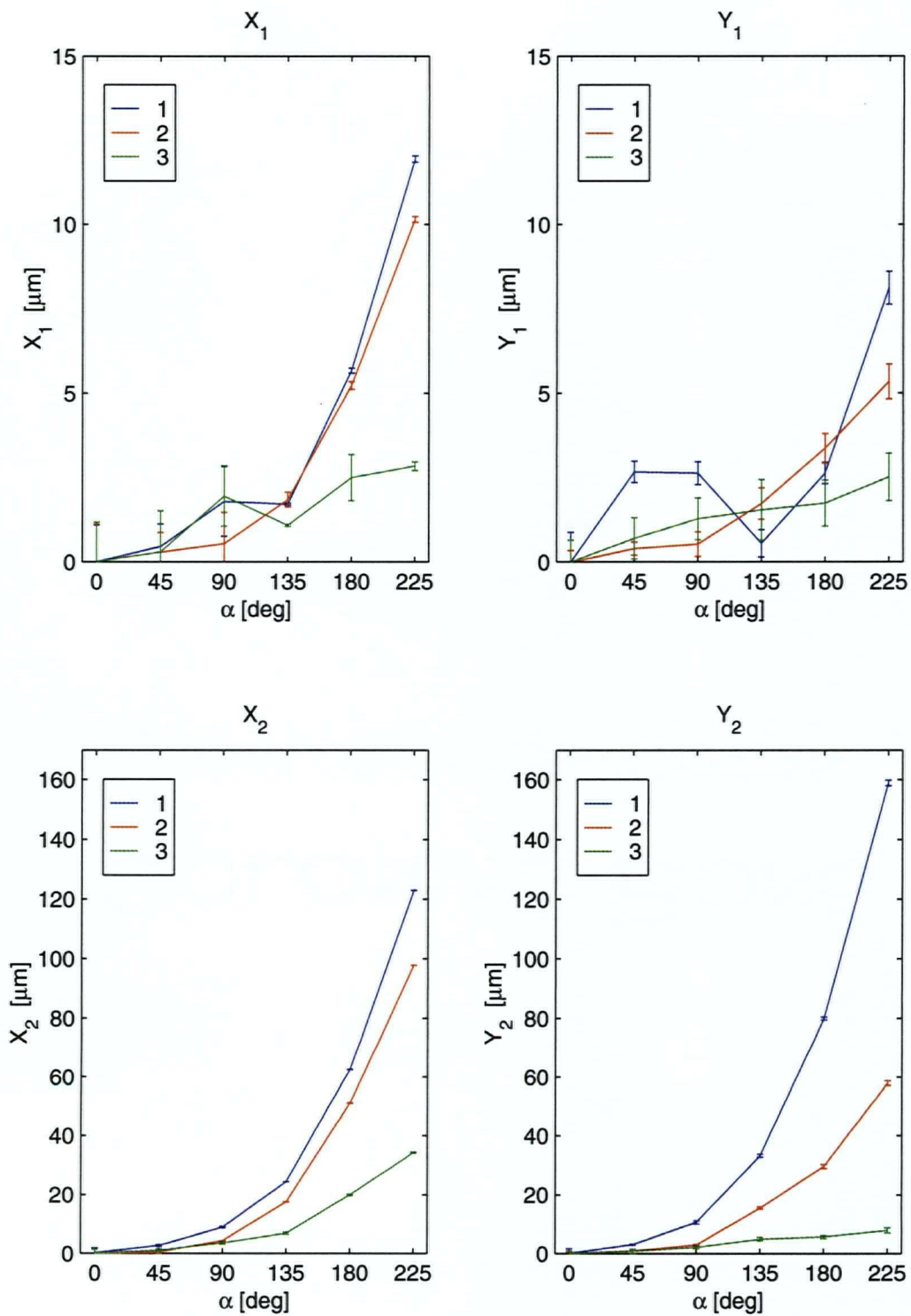


Figure 5.13: Mean values of 1st, 2nd and 3rd Fourier coefficients for a simulated crack at location 6 using the bolt removal method (errorbars mark standard deviation).

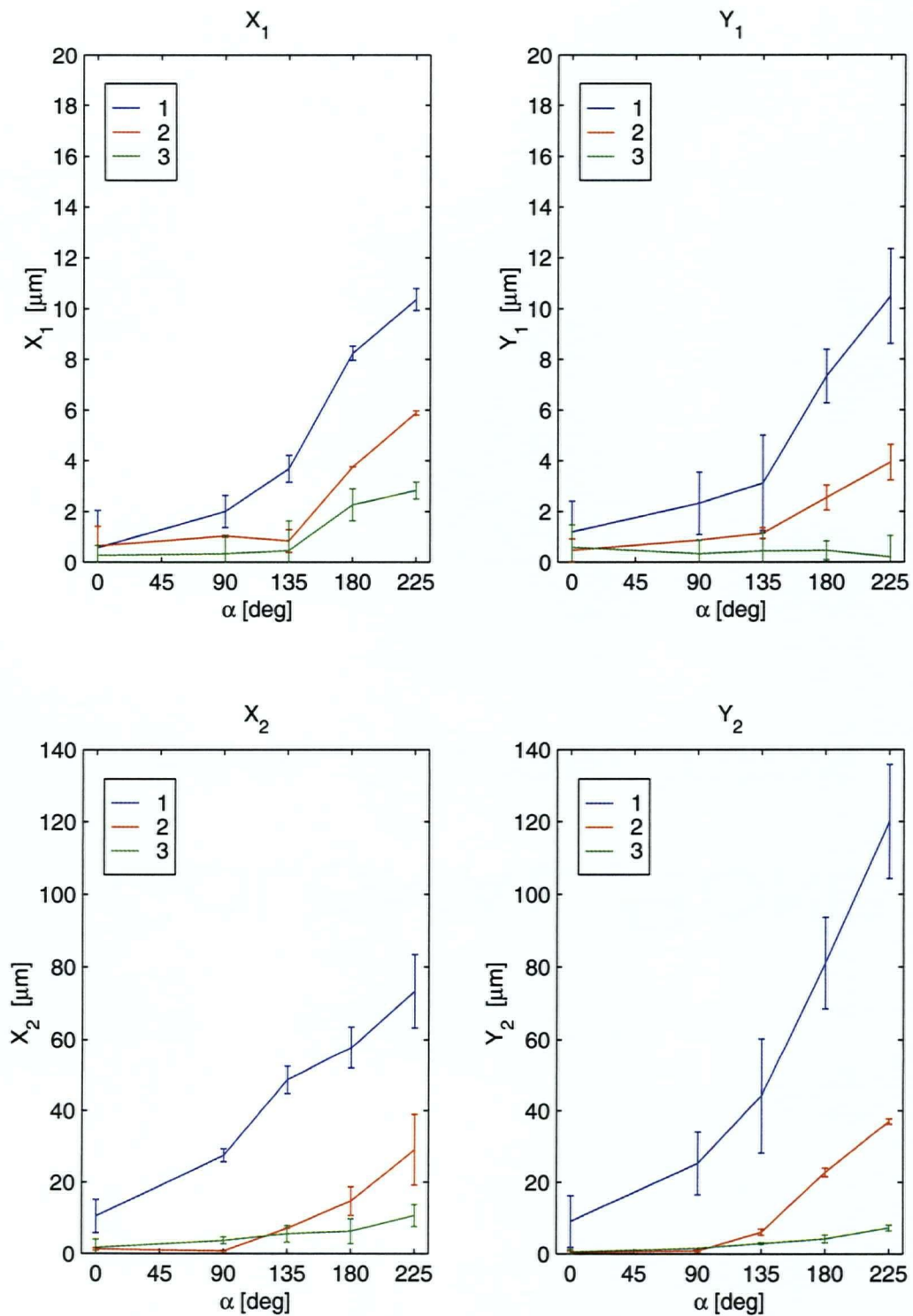


Figure 5.14: Mean values of 1st, 2nd and 3rd Fourier coefficients for a simulated crack at location 6 using the gap insertion method (errorbars mark standard deviation).

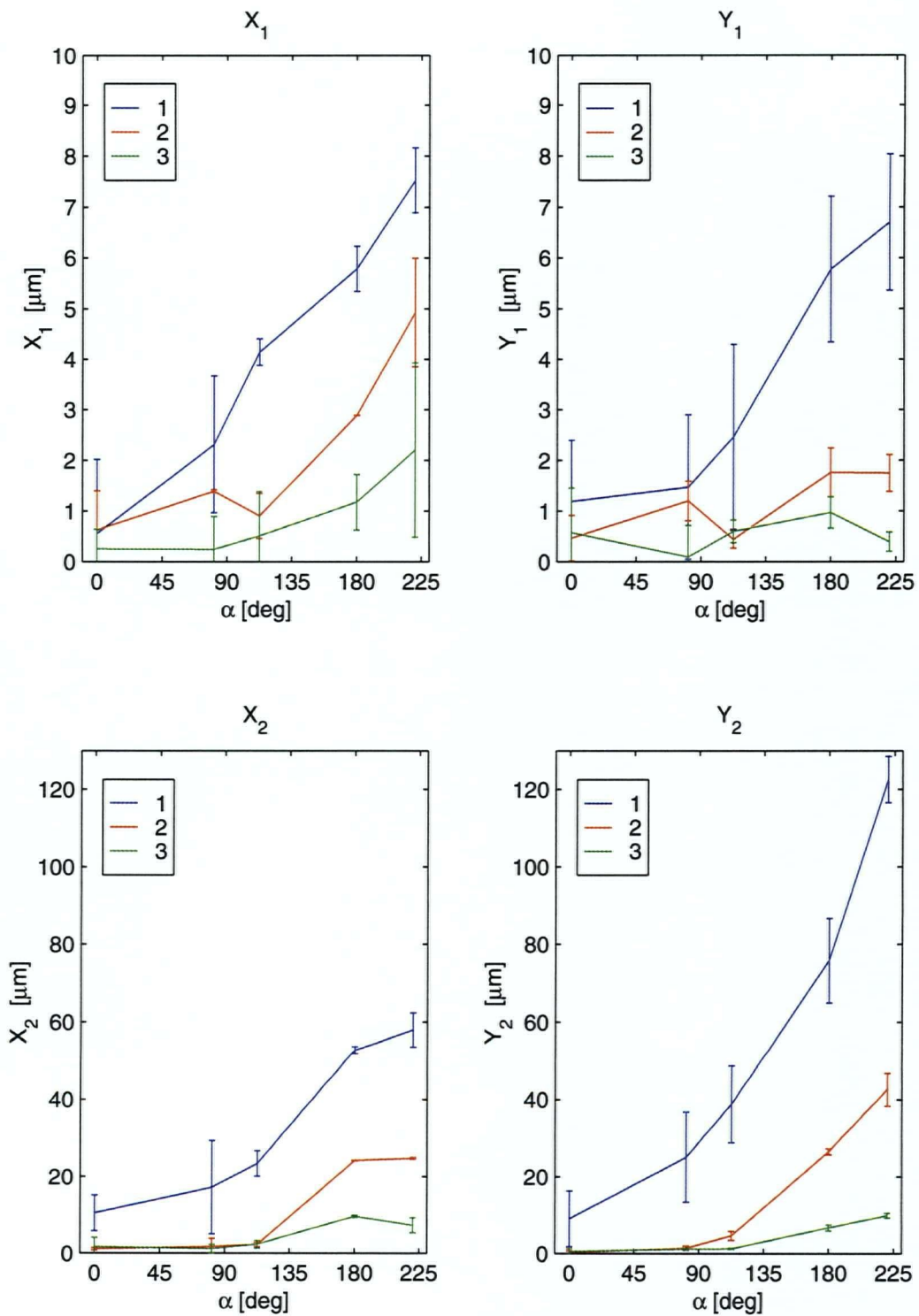


Figure 5.15: Mean values of 1st, 2nd and 3rd Fourier coefficients for a fatigue crack at location 6 (errorbars mark standard deviation).

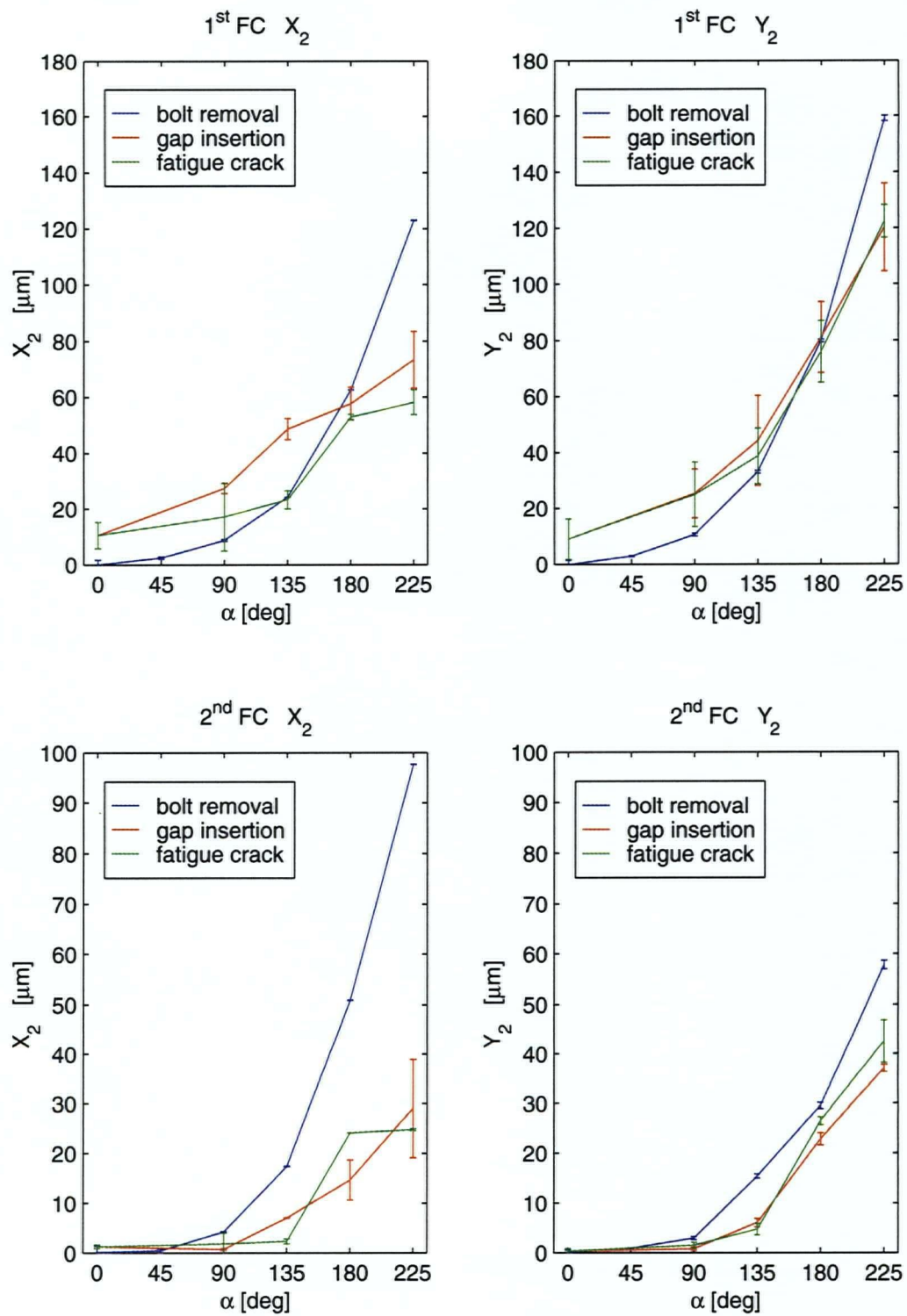


Figure 5.16: Comparison of 1st and 2nd Fourier coefficients for different crack simulation methods at location 6 (errorbars mark standard deviation).

CHAPTER 6

CRACK IDENTIFICATION USING INVERSE ANALYSIS

6.1 The inverse problem of crack identification

The problem of identifying a crack in a rotor based on vibration measurements represents an inverse problem where the sources (applied loading) and the response u (vibration) are known, but the exact state of the system (rotor) is unknown. To solve the problem using inverse analysis, it is treated as a parameter identification problem with the crack being completely described by a set of parameters x . A forward model $f(x)$ is required to compute the predicted response of the system based on the applied loading and the specified parameters. An objective function ϕ may be defined as a measure of the difference between the measured and the modeled responses across all measurement points. Here, a least-squares approach is commonly used:

$$\phi(x) = \sum_j (u_j - f_j(x))^2 \quad (6.1)$$

It is obvious that a set of parameters yielding $\phi = 0$ represents a possible solution to the inverse problem. However, due to modeling and measurement errors it is typically not possible to achieve $\phi = 0$, thus the goal is to find a set of parameters x that will minimize ϕ , which means that the inverse problem has been transferred to a non-linear optimization problem. Furthermore, inverse problems in physics typically allow the placement of lower and upper bounds to the parameter set describing the problem, thus the inverse problem results in the constraint optimization problem:

$$x^* = \text{minimize } \phi(x) \quad (6.2)$$

subject to: lower bound $< x <$ upper bound

which is well discussed in the literature and may be treated with a variety of solution techniques [146].

The main difficulty when solving inverse problems is that they are often ill-posed and that the solution is non-unique or may not exist at all. Transferred to the optimization problem this means that the objective function may have many local minima, the true solution might be one of the local minima rather than the global minimum or none of the minima at all. To counter these problems researchers typically employ regularization techniques [122] and try to keep the total number of parameters low.

For the case of the cracked drum, the describing parameter or the design parameter set is chosen to be the crack size α and the crack location L , where $L = 1, \dots, 6$ is a discrete parameter describing the six possible crack locations of the drum; see Figure 4.4. Furthermore, it is assumed that only one crack exists in the structure at a time and that the crack size is limited between 0° and an arbitrary upper bound greater than 180° , e.g., 250° . Thus the constraint optimization problem may be written as

$$(\alpha^*, L^*) = \text{minimize } \phi(\alpha, L) \quad (6.3)$$

$$\text{subject to: } 0^\circ \leq \alpha \leq 250^\circ, L = 1, 2, 3, 4, 5, 6.$$

The specific solution technique employed has a great influence on solving the optimization problem successfully. Local optimization algorithm such as second order Quasi-Newton methods are more commonly used to find the exact location of a close-by minimal point while global optimization algorithms such as golden section search, trust region methods or genetic algorithms are often used to determine approximate locations of the global minimum within the entire domain. The following sections investigate the solution of equation (6.3) and discusses the applicability of various optimization algorithms.

6.2 Identification of crack size for a known crack location

As a first step, the identification of the crack size for a known crack location, location 6, will be investigated. Hence, the optimization problem (eq. 6.3) simplifies to

$$\alpha^* = \text{minimize } \phi(\alpha) \quad (6.4)$$

subject to: $0^\circ \leq \alpha \leq 250^\circ$.

which represents a single variable constraint optimization problem. The objective function ϕ is chosen based on the general form of equation (6.1), yielding

$$\begin{aligned} \phi &= \sum_j w_j \frac{(C_j^{FEA} - C_j^{exp})^2}{(C_j^{exp})^2} \\ &= w_{x1} \frac{(C_{x1}^{FEA} - C_{x1}^{exp})^2}{(C_{x1}^{exp})^2} + w_{x2} \frac{(C_{x2}^{FEA} - C_{x2}^{exp})^2}{(C_{x2}^{exp})^2} + w_{x3} \frac{(C_{x3}^{FEA} - C_{x3}^{exp})^2}{(C_{x3}^{exp})^2} \\ &\quad + w_{y1} \frac{(C_{y1}^{FEA} - C_{y1}^{exp})^2}{(C_{y1}^{exp})^2} + w_{y2} \frac{(C_{y2}^{FEA} - C_{y2}^{exp})^2}{(C_{y2}^{exp})^2} + w_{y3} \frac{(C_{y3}^{FEA} - C_{y3}^{exp})^2}{(C_{y3}^{exp})^2} \\ &\quad + v_{x1} \frac{(D_{x1}^{FEA} - D_{x1}^{exp})^2}{(D_{x1}^{exp})^2} + v_{x2} \frac{(D_{x2}^{FEA} - D_{x2}^{exp})^2}{(D_{x2}^{exp})^2} + v_{x3} \frac{(D_{x3}^{FEA} - D_{x3}^{exp})^2}{(D_{x3}^{exp})^2} \\ &\quad + v_{y1} \frac{(D_{y1}^{FEA} - D_{y1}^{exp})^2}{(D_{y1}^{exp})^2} + v_{y2} \frac{(D_{y2}^{FEA} - D_{y2}^{exp})^2}{(D_{y2}^{exp})^2} + v_{y3} \frac{(D_{y3}^{FEA} - D_{y3}^{exp})^2}{(D_{y3}^{exp})^2} \end{aligned} \quad (6.5)$$

where, for example, C_{x1}^{FEA} is the amplitude of the 1/rev. vibration component (1st Fourier coefficient) in the x (horizontal) direction predicted on side 1 (drive side) of the drum, and D_{y3}^{exp} is the amplitude of the 3/rev. vibration component (3rd Fourier coefficient) in the y (vertical) direction measured on side 2 (idle side).

Since absolute values of vibration levels of the 1/rev., 2/rev. and 3/rev. vibration components C_j vary greatly, they are normalized by dividing through the associated measured vibration component. Their relative importance within the objective function is then determined by the weighting functions w_j . Several sets of weighting functions have been investigated in this study and they are summarized in Table 6.1.

weight factor w_j	Description	Objective function
$w_j = 1$	Fourier coefficients are weighted equally	Φ_{fc0}
$w_j = \begin{cases} 0 & , j \neq 1 \\ 1 & , j = 1 \end{cases}$	1/rev. amplitude only	Φ_{fc1}
$w_j = \begin{cases} 0 & , j \neq 2 \\ 1 & , j = 2 \end{cases}$	2/rev. amplitude only	Φ_{fc2}
$w_j = \begin{cases} 0 & , j \neq 3 \\ 1 & , j = 3 \end{cases}$	3/rev. amplitude only	Φ_{fc3}
$w_j = (C_j^{exp})^2$	Unweighted time-domain signal difference	Φ_{tds}
$w_j = \frac{(C_j^{exp})^2}{(C_1^{exp})^2}$	Fourier coefficients are weighted relative to the 1/rev. amplitude	Φ_{exp1}

Table 6.1: Weight factors and associated objective functions.

The optimization was performed using Matlab's Optimization Toolbox [144] and employed algorithms were the golden section search (GSS: Matlab's *fminbnd* function), Powell's method (Appendix C.1), a Sequential Quadratic Programming (SQP: Matlab's *fmincon* function for medium scale problems) method and a trust region method based on a least-squares implementation of the objective function (LSQ: Matlab's *lsqnonlin* function for large scale problems). The required forward solution of the problem was obtained using the drum FE model in conjunction with the nodal crack force method, described in Chapter 4. The FE calculations were previously conducted using ANSYS [143] and results for a specific set of parameters were recorded into a response database which then acted as a look-up table for the required solutions throughout the inverse analysis process. The measured vibration components were obtained from experimental results using the bolt removal method, described in Chapter 5. Values for crack sizes between the discrete measured crack sizes were linearly interpolated from the two neighbouring measured Fourier coefficients. A flow chart of the optimization procedure is shown in Figure 6.1.

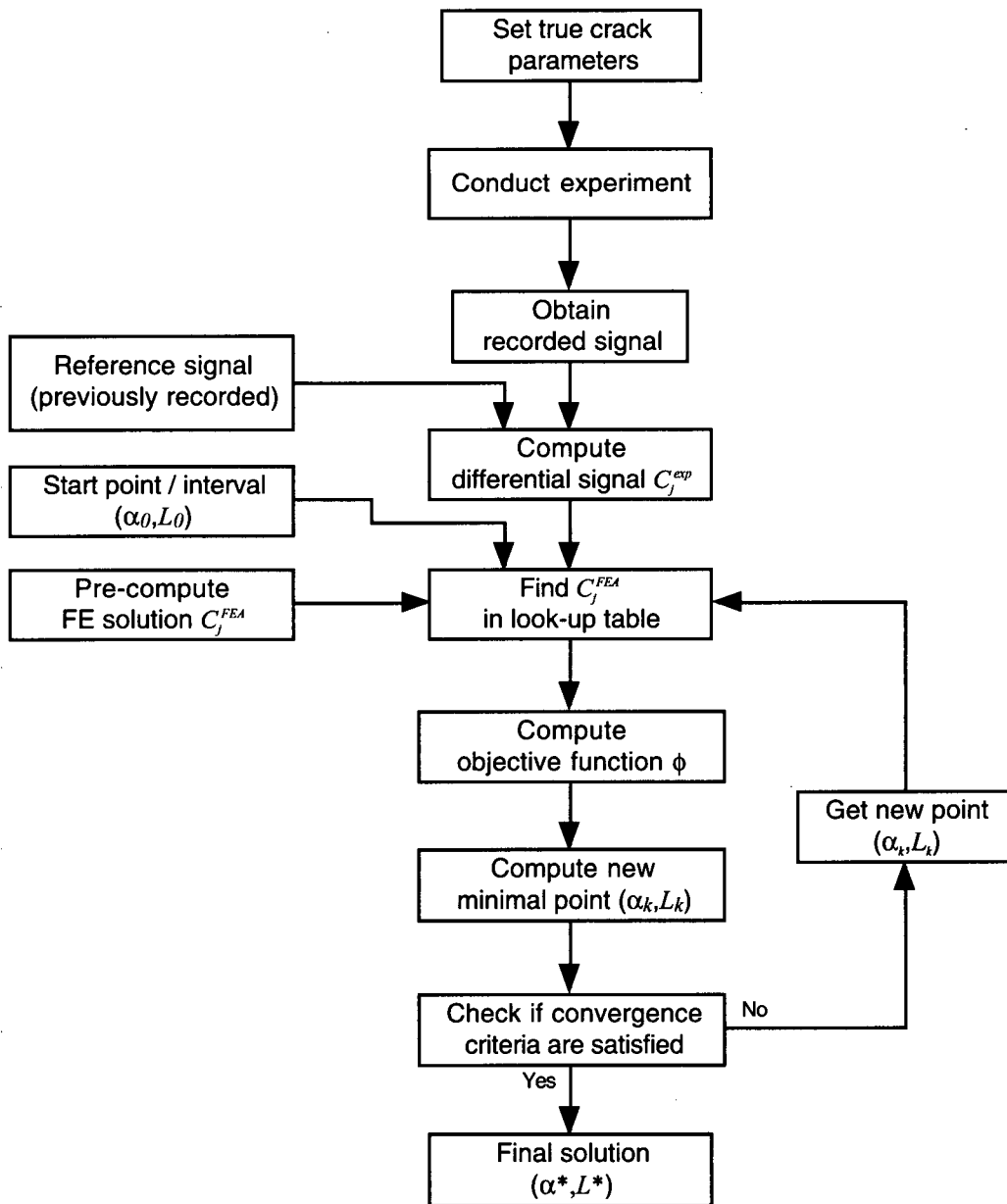


Figure 6.1: Flow chart of the optimization procedure.

Results of the inverse analysis are shown in Figure 6.2. Numerical values of the results are summarized in Table 6.2. A sample comparison of the experimental and the identified time-domain signal for $\alpha_{\text{true}} = 120^\circ$ is shown in Figure 6.3. Inverse analysis results for crack locations 1 to 5 may be found in Appendix C.2.

Results based on the GSS and LSQ algorithms show generally good agreement with the true crack size. For the majority of the domain, $30^\circ \leq \alpha \leq 160^\circ$, the algorithms underestimates the true crack size by 10 % on average while somewhat overestimating α for larger crack sizes. Both methods yield virtually identical minimal points in these regions. However, the LSQ method requires on average only 8.7 function evaluations to achieve these results, while the GSS requires 12.2. For smaller crack sizes, $\alpha < 30^\circ$, noise dominates the measured vibration signal, thus a crack of $\alpha^* \approx 30^\circ$ is always identified. Therefore, $\alpha^* = 30^\circ$ must be considered a lower detection limit, below which reliable crack size identification may not be achieved.

Powell's method yields results comparable to those from the other two methods but underestimates the true crack size on average by 20 %. Furthermore, values of the objective function for the identified minima; see Figure 6.2(b), confirm that deviating results using Powell's method are clearly worse than those of the GSS and LSQ algorithm.

Method	Mean relative error ⁽¹⁾ $\frac{1}{n} \sum_{j=1}^n \frac{ \alpha_n^* - \alpha_n }{\alpha_n}$	Mean number of function evaluations (N_f)
GSS	10.7 %	12.2
Powell	23.1 %	10.4
SQP	56.5 %	7.9
LSQ	11.9 %	8.7

⁽¹⁾ for $\alpha \geq 30^\circ$

Table 6.2: Performance comparison of optimization techniques.

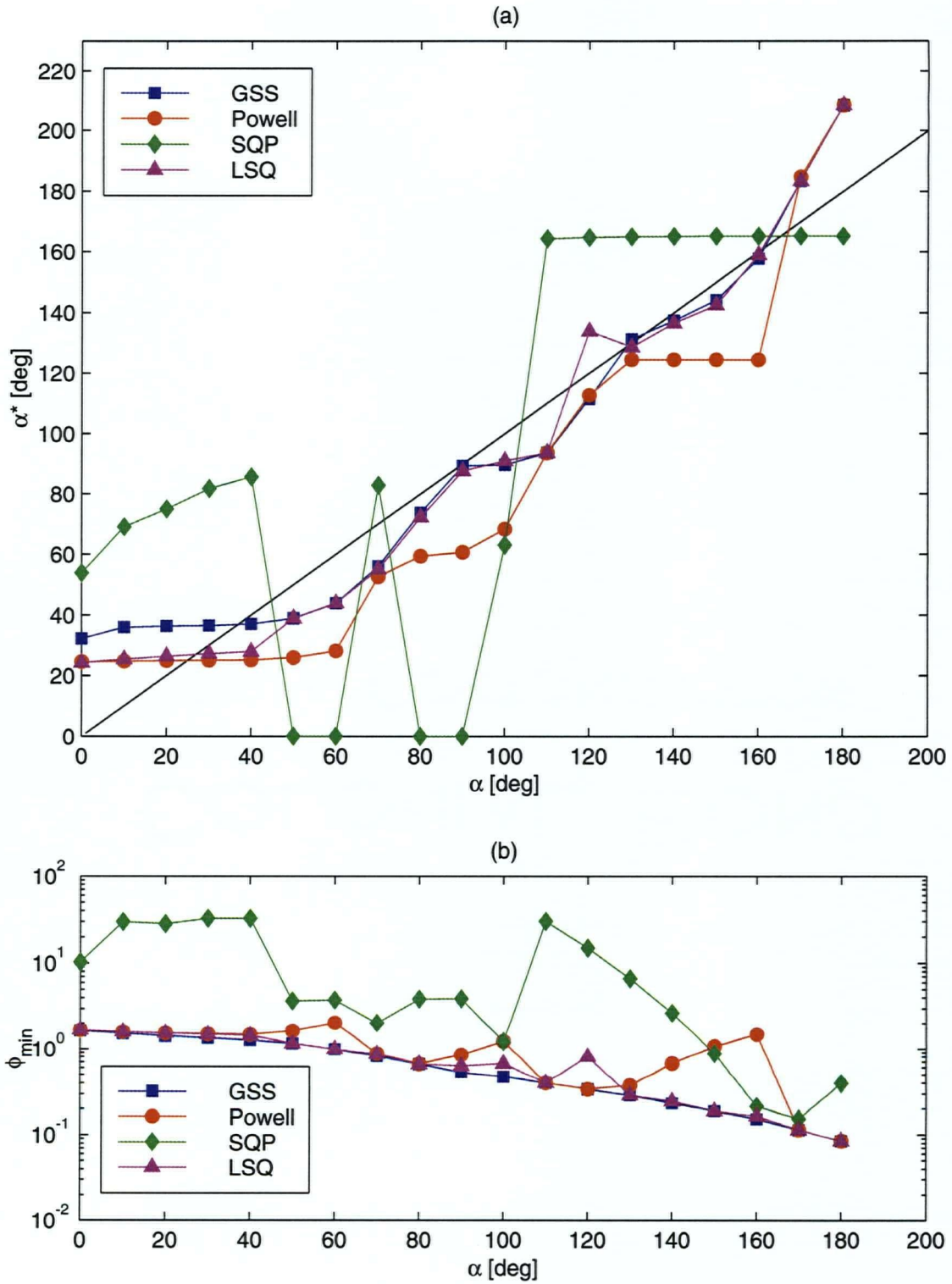


Figure 6.2: (a) Results of the crack identification procedure for a crack at known crack location 6. (b) Value of the objective function at the minimal point.

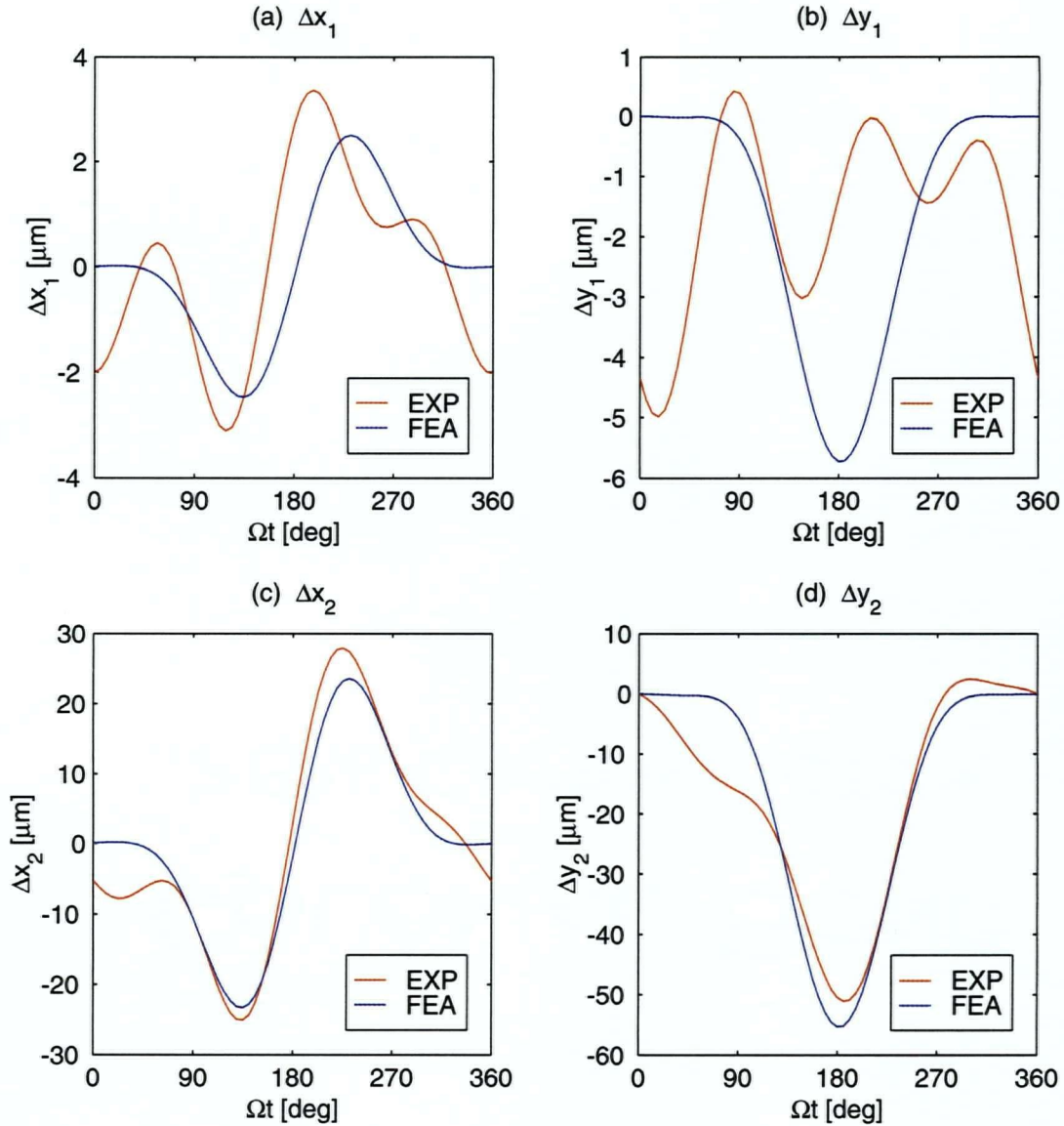


Figure 6.3: Comparison of experimental and identified vibration signature for $\alpha_{\text{true}} = 120^\circ$ at location 6.

On the other hand, results using the SQP method bear no resemblance to the true crack size for the entire domain, and their minimal function values are significantly greater than those from the other methods. This surprising result may be explained by graphing the shape of the objective function versus the increase in crack size, shown in Figure 6.4. The graph shows that GSS, LSQ and Powell's method do identify the global minima correctly. More importantly however, it shows that the shape of the objective function is

not smooth at all and that the gradient would be of very little use in finding the location of the function's minimum. Therefore, it is not surprising that the SQP method, relying strongly on the function gradient, is the least successful in reaching the global minimum of the objective function.

The influence of the weight factors on the identified crack size is shown in Figure 6.5(a). Identified crack sizes α^* for $\alpha \geq 130^\circ$ are virtually identical. Below $\alpha = 130^\circ$ results are generally close to the true solution, but ϕ_{fc1} , ϕ_{exp1} and ϕ_{lds} tend to overestimate the true crack size, while ϕ_{fc0} and ϕ_{fc2} slightly underestimate α_{true} . Further analysis shows that this stems from the strong influence of the 1/rev. vibration component on the former objective functions, while ϕ_{fc0} and ϕ_{fc2} are greater influenced by the 2/rev. amplitude.

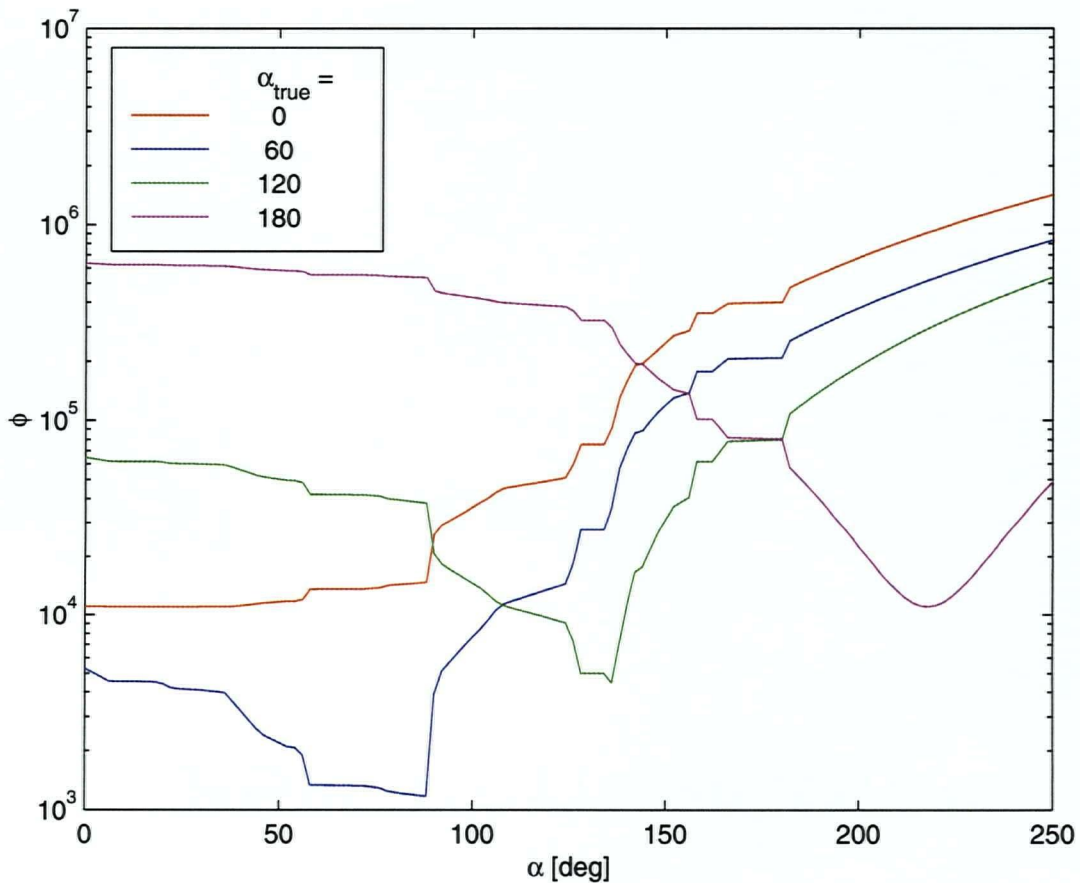


Figure 6.4: Value of the objective function $\phi(\alpha)$ for various true crack sizes α_{true} .

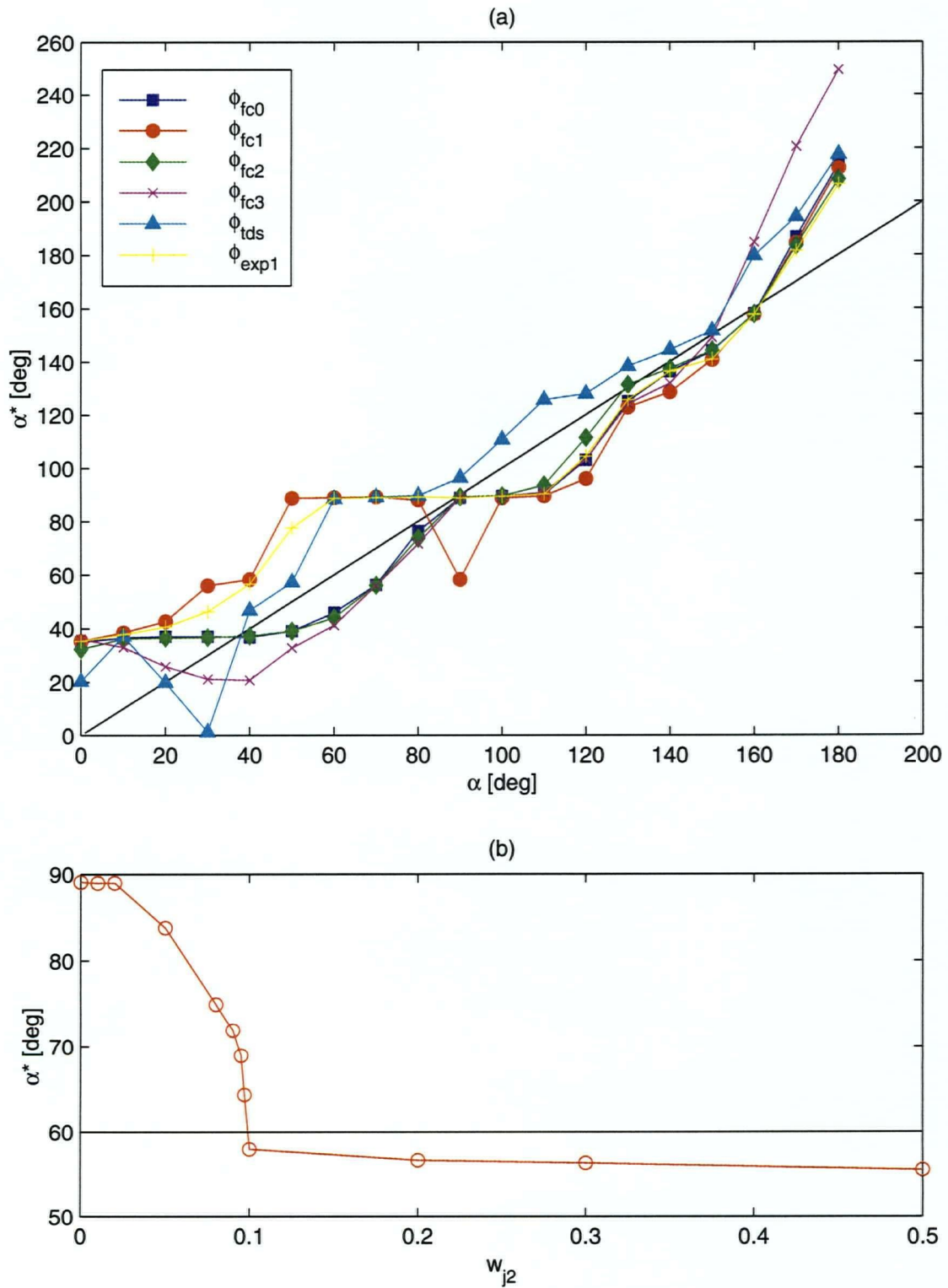


Figure 6.5: (a) Identified crack size α^* for different weight functions w_j ; see Table 6.1.

(b) Influence of the weight factor w_{j2} on the identified crack size.

The objective function ϕ_{fc3} , which depends on the 3/rev. amplitude only, yields clearly the worst results. It appears that the right combination of 1/rev. and 2/rev. amplitude should yield an optimal objective function for the purpose of crack identification. Figure 6.5(b) shows the influence of w_{j2} for $w_{j1} = 1$ and $w_{j3} = 0$, i.e., interpolation between ϕ_{fc1} and ϕ_{fc0} for $\alpha = 60^\circ$. It shows that the interpolation is not linear but rather a step function. Furthermore, results for other values of α show a similar behaviour. This makes optimization of the weight factors difficult beyond a basic common sense approach. On the other hand, Figure 6.5(a) shows that simple ϕ_{fc0} and ϕ_{fc2} will yield good results over the entire domain, and it confirms the importance of the 2/rev. amplitude that has been noted by many researchers.

6.3 Identification of crack size and location

6.3.1 Multi-variable optimization

In order to solve the original problem stated in equation (6.3), the simultaneous identification of crack size and location using multi-variable optimization algorithms, the discrete parameter L is converted to a continuous parameter by linearly interpolating Fourier coefficients from neighbouring crack locations, thus

$$C_j^{FEA}(\alpha, L) = (L_2 - L) C_j^{FEA}(\alpha, L_1) + (L - L_1) C_j^{FEA}(\alpha, L_2), \quad (6.6)$$

where L_1 and L_2 are the next lower and higher integers to L , respectively.

It should be noted that strictly speaking the chosen interpolation for L (eq. 6.6) is certainly not ideal to be used in multi-variable optimization, since L is not directly related to any physical quantity. A better approach might be interpolation along the drum axis coordinate or between the coordinates of a 3D coordinate system. However, the former approach may yield poor results since the drum axis coordinates of the three crack locations on either side of the drum are almost identical, while the latter requires the increase in the number of location parameters from one to three. Hence, it is believed that

equation (6.6) represents a simple and acceptable compromise to evaluate the feasibility of multi-variable optimization for crack identification in the pressure washer drum.

The employed optimization algorithms are the LSQ and SQP methods described in section 6.2, a two-dimensional version of Powell's method (Appendix C.3) and the Nelder-Mead algorithm [146], a special optimization algorithm for noisy objective functions. A contour plot of the objective function for a crack of size $\alpha = 120^\circ$ at location 6 is shown in Figure 6.6. Exemplary convergence paths and results for the four optimization algorithms are shown in Figure 6.7. Numerical values of the results are summarized in Table 6.3.

The graphs emphasize the difficulties of using deterministic multi-variable optimization routines when solving this inverse problem. The objective function is not smooth and the ridge rising between $L = 3$ and 4 for high values of α poses additional difficulties. For the starting point $x_0 = (200,4)$, from an optimization point of view, the best result is achieved by the LSQ method, reaching the global minimum while requiring the least number of function evaluations. The global minimum is also correctly identified using the Nelder-Mead algorithm, but significantly more function evaluations are required. On the other hand, the SQP algorithm correctly identifies the true solution, marked by a red square. However, this point does not represent the global minimum of the objective function but rather a local minimum close by. This is a direct result of the always present experimental uncertainty, modeling error and noise. Therefore, it may be concluded that the correct identification of the true solution by the SQP algorithm is a coincidence rather than superior performance. Nonetheless, results from the SQP, LSQ and Nelder-Mead algorithms certainly aid in identifying the real crack size and location. Their shortcoming is that they provide very little information about the neighbourhood around the global minimum.

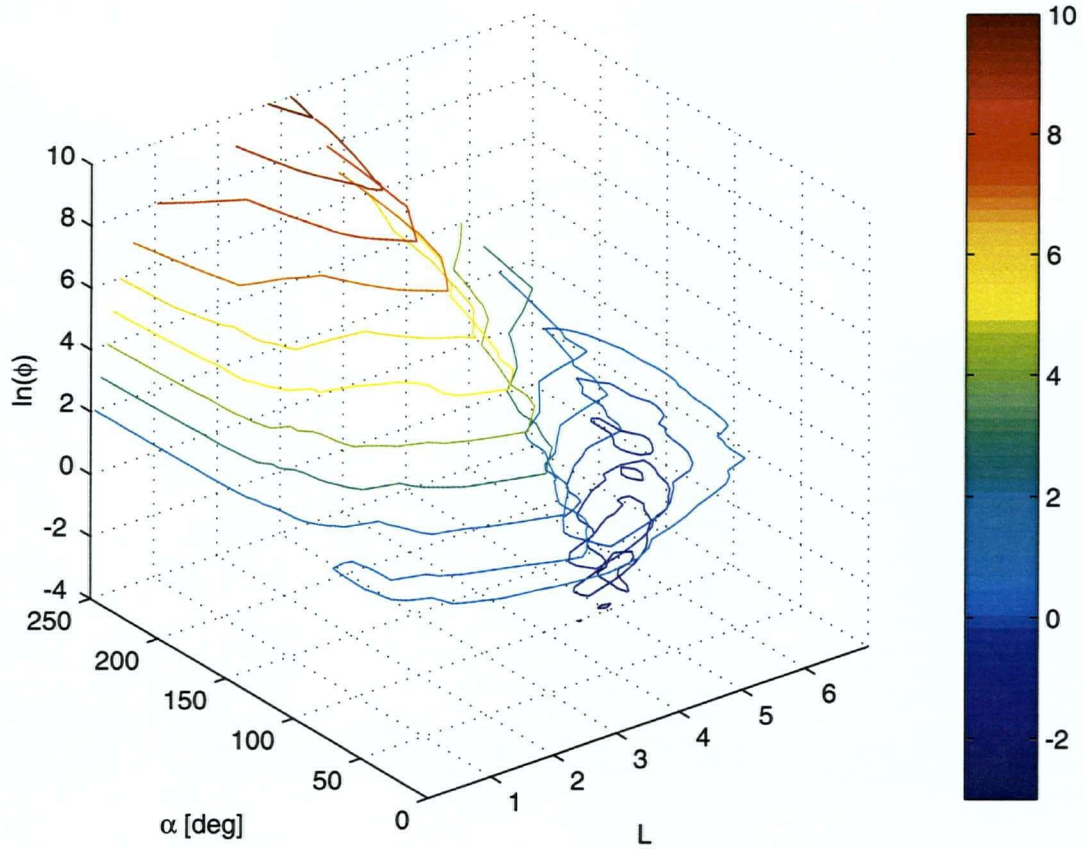


Figure 6.6: 2D objective function $\phi(\alpha, L)$ for a crack
of size $\alpha_{\text{true}} = 120^\circ$ at location $L_{\text{true}} = 6$.

Method	Identified crack size α^*	Identified location L^*	Function value ϕ_{\min}	Number of function evaluations N_f
Powell 2D	17°	2.9	1.9325	21
LSQ	105°	5.0	0.0332	19
Nelder-Mead	105°	5.2	0.0270	33
SQP	122°	6.0	0.1210	14

Table 6.3: Performance comparison of multi-variable optimization techniques for $(\alpha_{\text{true}} = 120^\circ, L_{\text{true}} = 6)$.

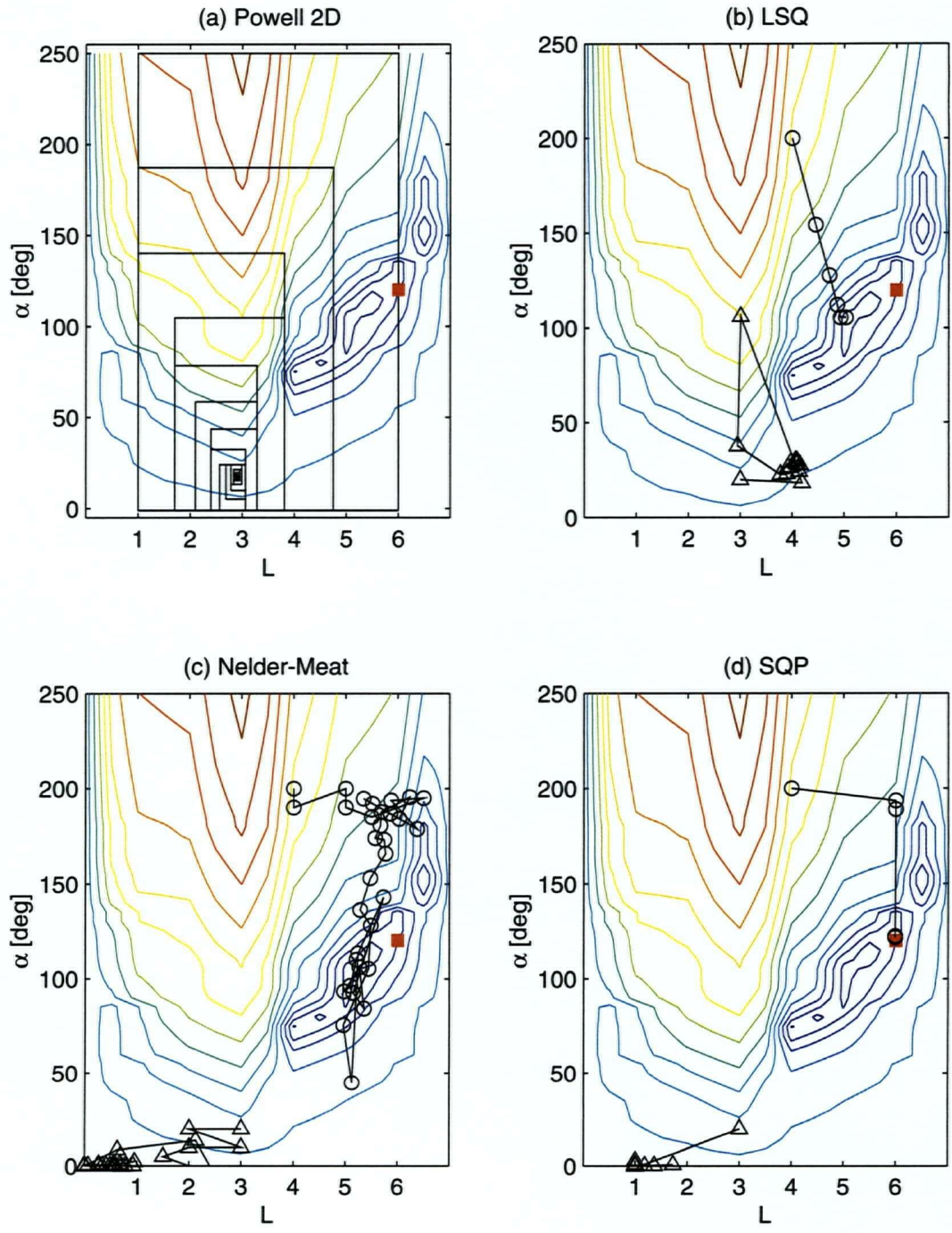


Figure 6.7: Inverse analysis results for $\alpha_{\text{true}} = 120^\circ$, $L_{\text{true}} = 6$ (■):

(a) 2D Powell algorithm, (b) LSQ, (c) Nelder-Mead algorithm, (d) SQP.

O indicates convergence path from starting point $x_0 = (200, 4)$,

Δ indicates convergence path from starting point $x_0 = (20, 3)$.

For a different starting point, in particular one at the other side of the ridge, e.g., $x_0 = (20,3)$, neither of the three algorithms converges to the global minimum. This shortcoming may be easily prevented by beginning a series of optimization procedures from different starting points and comparing the achieved solutions. Naturally, the cost of this analysis will rise linearly with the number of trial starting points. The simple two-dimensional Powell method, even though sampling function values over the entire domain, converges to the wrong area of the domain and is considered unsuitable for solving this type of problem.

Other examples of crack identification results for different crack parameter combinations are shown in Appendix C.4. In general, objective function and optimization algorithms show a similar behaviour as was described above. While in most cases the true solution did not represent the global minimum, they were always in close proximity to one another. Hence, it may be concluded that finding the global minimum of $\phi(\alpha,L)$, while not being identical to the true solution, does yield a good estimate of the existing crack.

6.3.2 De-coupling of crack size and location

Placing the original problem of equation (6.3) into a more practical context and based on the results discussed in section 6.3.1, it seems more advantageous to a machine operator to obtain information about the neighbourhood around the global minimum rather than to obtain a single minimizing result. In practice this means the machine operator would be provided with a set of the most probable crack parameter combinations and ideally a measure of probability or confidence associated with each set. Furthermore, it should be recognized that the crack location L in equation (6.3) is actually a discrete parameter taking on only a limited number of values. Therefore, a different approach to solving the inverse problem is taken in which the de-coupling of crack size and location throughout the optimization procedure will provide more information of the solution while making use of the discrete nature of L .

In a first step equation (6.3) will be divided into six separate sub-problems for each of the crack locations:

$$(\alpha^*, L^*) = \min \psi(L), \quad L = 1, \dots, 6 \quad (6.7)$$

$$\text{where: } \psi(L) = \min \phi_L(\alpha), \quad \text{subject to: } 0^\circ \leq \alpha \leq 250^\circ,$$

which means that the inverse problem will be performed as a single-variable parameter optimization for each of the two crack locations, and the final solution is chosen to be the minimum of the individual solutions. To solve each separate sub-problem, the solution techniques discussed in section 6.2 may be used. However, rather than choosing a final solution (α^*, L^*) , as suggested by equation (6.7), a confidence measure λ is introduced, defined by

$$\lambda(L) = \frac{\min \psi}{\psi(L) \cdot \sum_{L=1}^6 \frac{\min \psi}{\psi(L)}} \quad (6.8)$$

λ represents a relative measure of the value of the objective function for the individual solutions ϕ_L^* , where a greater value of ϕ_L^* yields a lower value of $\lambda(L)$, i.e., a lower confidence in the sub-solution at that crack location being the global minimum. It is easily shown that

$$\sum_{L=1}^6 \lambda(L) = 1. \quad (6.9)$$

Figure 6.8 shows typical results of the identified crack size at each location and their associated confidence value for various crack parameter combinations. First, it can be seen that for the two medium sized cracks, $\alpha_{\text{true}} = 90^\circ$ and 120° , Figures 6.8(c) and (d), the identified crack sizes at the true crack location are very close to the real crack sizes.

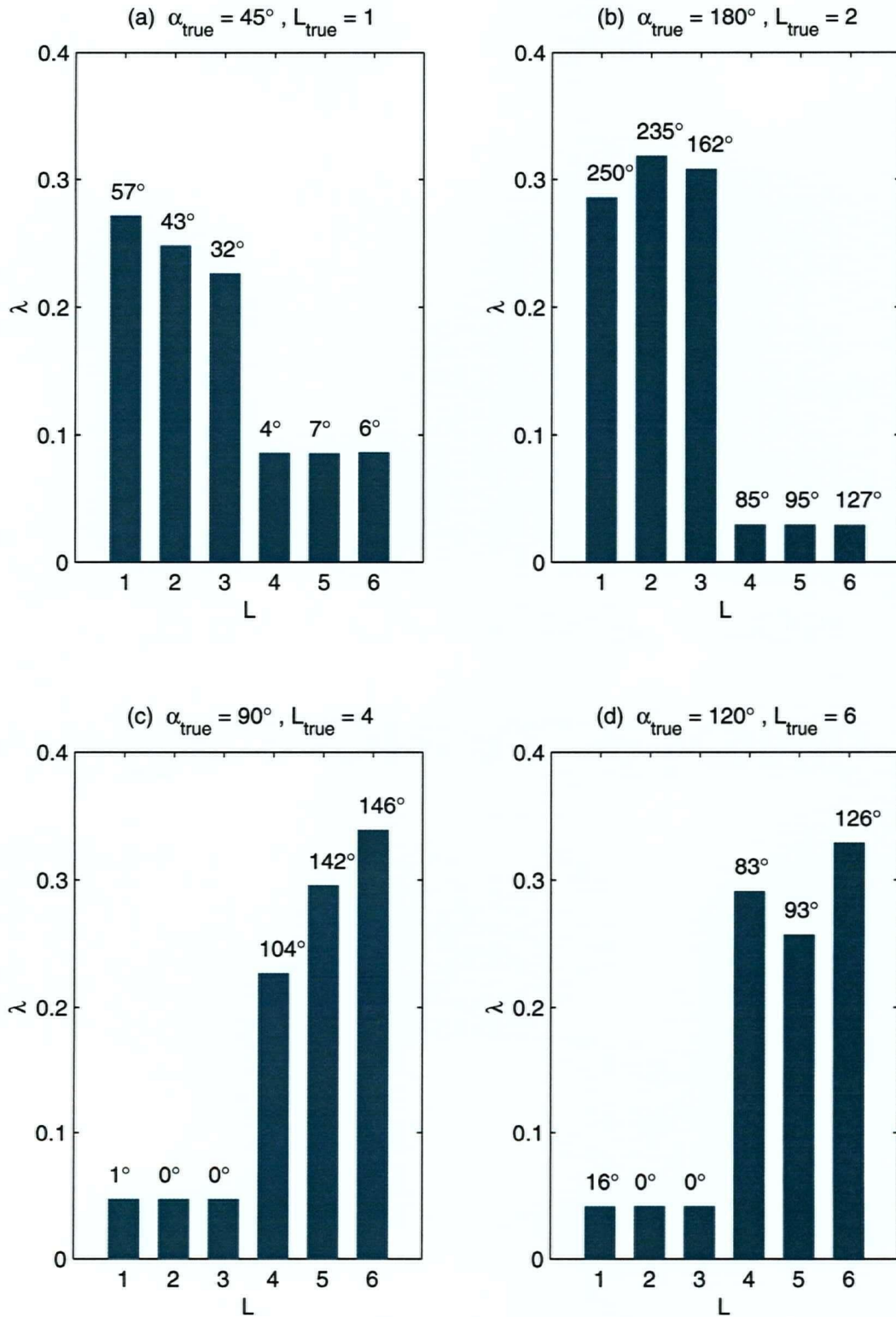


Figure 6.8: Identified crack sizes and confidence values for various crack parameters.

For the $\alpha_{\text{true}} = 45^\circ$ and 180° , Figures 6.8(a) and (b), the real crack size is overestimated by approximately 25-30 %. At the same time, the confidence values for locations on the cracked side of the drum are generally high while those of the uncracked side are comparably low. Thus, it can be concluded that the inverse analysis correctly identifies the cracked side of the drum for all cases. Also, in three cases, (a), (b) and (d), the highest confidence value was assigned to the real crack location, thus identifying the true location correctly. For case (c), ($\alpha_{\text{true}} = 90^\circ$, $L_{\text{true}} = 4$), a crack of similar size at a close-by location had also been identified and been given a higher confidence value. This was to be expected since crack locations 1, 2 and 3 as well as 4, 5 and 6 are quite close to one another and their axial distances from the bearing locations are virtually identical.

Overall it can be said that the information drawn from the results of this inverse analysis seem more valuable in identifying a crack in the drum than results from the multi-variable optimization presented in section 6.3.1. By de-coupling the optimization problem, the solution techniques for solving the single-variable optimization sub-problem can be employed, which are more stable and always converged to the true solution. This is not true for the results from multi-variable optimization algorithms which depended on the starting point. Therefore, it is necessary to conduct a series, three at a minimum, of optimization runs in order to verify the global minimum. The computational effort for conducting three multi-variable inverse analyses is approximately equal to that of the six single-variable analyses. Hence, de-coupling the inverse problem will result in a more detailed image of the real situation at the same or less cost than a multi-variable approach.

Naturally, the cost of de-coupling will rise with an increase in considered crack locations. However, for many applications it seems feasible to limit the number of possible crack locations to a small number, e.g., less than ten. In other cases a multi-variable approach may be more beneficial. This decision must be made on a case by case basis.

CHAPTER 7

CONCLUSIONS

7.1 Summary of results

A new approach to compute the vibration of a cracked rotor, the nodal crack force approach, was introduced making use of the dominant static deflection of heavy rotors or a dominant steady state solution around which the non-linear vibrations due to the crack are linearized. The vibrations are computed using 3D solid Finite Element (FE) analysis, which allows the analysis of structures of complicated geometry and does not impose common simplifications of previous analysis techniques. Results for the subcritical range for a short cantilever and a slender Laval rotor were computed and compared to alternative solutions from a two degree of freedom analytical model and a 3D FE solution based on time-integration and node de-coupling to simulate crack breathing. The nodal crack force approach yielded results very close to the 3D node de-coupling simulation. The typical features of a cracked shaft known from the literature, additional peaks at $1/2$ and $1/3$ the critical speed and double and triple loop orbit shapes, were present in all simulation results. There was a significant difference, however, between the simplified analytical and the two 3D FE solutions, even for these ideal rotor shapes. It is conceivable that the difference will be even greater for a more complicated rotor geometry, in which case the 3D FE models might be considered as more accurate. The most important result, however, is that the 3D nodal crack force approach yields comparable accuracy to the 3D time-integration results at a fraction of the computational cost. It was estimated that the computational savings factor will be at least 1:40 while avoiding the computational difficulties of convergence and stability problems altogether. This is a great advantage when considering the method for on-line crack identification purposes.

The nodal crack force approach was implemented for a scaled-down model of a slow rotating pressure washer drum. A crack of arbitrary size could be placed in the model at either of six locations that were known to experience cracking in the field. Again, two 3D FE comparison models, a nodal de-coupling approach and a contact element approach

computing a quasi-static solution, were used to verify the nodal crack force results. Results show the nodal crack force approach to be in excellent agreement with the contact element approach. In particular, it may be seen that the nodal crack force approach does not suffer the reduced peak horizontal deflection results of the node decoupling method. The early opening of crack faces in the nominally compressive region of the rotor for larger crack sizes, predicted by Schmalhorst [52], was confirmed by plotting the contact element status over one full revolution. The only disadvantage of the nodal crack force approach is that in its present form it is unsuitable to model cracks greater than 180° or half of the diameter. However, for practical purposes crack identification should take place before a crack may grow to this size. Overall it is concluded that the 3D nodal crack force approach represents the most efficient method to compute the vibration of a cracked rotor yielding significant computational savings and stability at acceptable accuracy.

On the experimental side, a scaled-down model of a pressure washer drum was built and equipped with proximity probes to monitor its lateral vibration. Since growing a fatigue crack of known size at a specific location poses great difficulties, two alternative experimental crack simulation techniques were also investigated. It was found that the simple bolt removal technique by Tamura [100] yielded only slightly increased vibration levels compared to the more accurate, but more elaborate, gap insertion method or growing a fatigue crack. Only the second Fourier coefficient of the horizontal vibration was significantly increased when using the bolt removal method. This may be due to the different shape of the crack front and to the fact that the simulated crack faces were smooth while the fatigue crack faces were rough offering much more sliding resistance due to friction. While the absolute value of the 1/rev. vibration amplitude was greater than the 2/rev. amplitude, the 1/rev. component exhibits generally more noise, thus emphasizing the importance of the 2/rev. vibration amplitude as a crack indicator. In conclusion the bolt removal method was viewed as the most effective approach for a complete parameter study for cracks at various locations, and it was estimated that the results will overestimate the vibration from a fatigue crack by approximately 10 %.

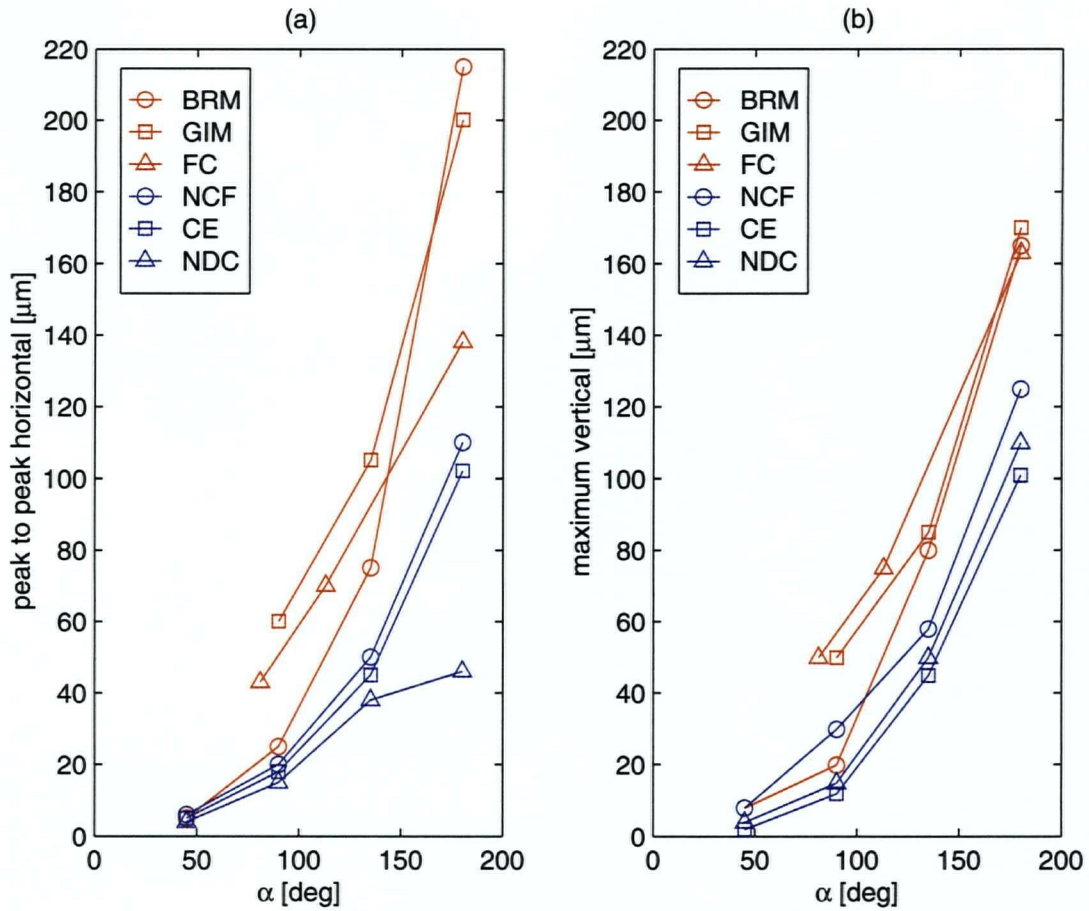


Figure 7.1: Comparison of FE (blue) and experimental (red) results for peak to peak horizontal (a) and maximum vertical (b) deflection.

Legend: BRM = bolt removal method, GIM = gap insertion method, FC = fatigue crack, NCF = nodal crack force approach, CE = contact element approach, NDC = node de-coupling approach.

A comparison between simulated and experimental results is provided in Figure 7.1. The graphs show peak to peak horizontal and maximum vertical deflection for all FE results and experimental crack simulation methods. As expected, the FE results underestimate the experimental results due to the higher stiffness of the FE approximation. FE results from the nodal crack force approach and the contact element analysis being approximately 75 % of the experimental measurements using a fatigue crack may be considered within the expected margin of error. Only the simulated horizontal deflection

compared to experimental results using gap insertion and bolt removal method show a larger difference of approximately 50 %. This indicates that the FE simulation provides good approximations to a fatigue crack while the experimental crack simulation methods are the reason for the increased horizontal deflection as was discussed previously. Overall, mean simulated and experimental vibration levels were distinct enough and their variations were small enough to differentiate between different crack sizes. It was concluded that simulation results using the nodal crack force approach and experimental results using the bolt removal method were similar enough to be used as the input to crack identification. In particular since for medium sized cracks a 25 % difference in vibration levels represents only a 10 % difference in crack size.

An experimental parameter study for all six proposed crack locations was conducted using the bolt removal method. Results served as measurement input to the inverse analysis process. In a first step, crack identification at a known crack location was conducted by single-variable optimization. The objective function was a weighted difference measure of Fourier coefficients and a variety of weight factors and optimization algorithms were employed. Results identified the true crack size within 10 % for most parts of the domain. It was shown that global optimization algorithms (golden section search, trust region method) yielded significantly better results than a Quasi-Newton method relying strongly on the objective function gradient. A graph of the objective function for several measurement points confirmed the noisy nature of the objective function and a significant variation in gradients over the entire domain. Hence, the usage of global optimization techniques is recommended for this type of problem, an observation which had previously been made in the literature [115]. Influence of the weighting function, and hence the importance of certain vibration components over others, proved to be of minor importance to the inverse analysis results. Various combinations of first and second Fourier coefficients all lead to similar results close to the true solution with objective functions relying strongly on the second Fourier coefficient achieving slightly better results. It was shown that the third Fourier coefficient has only a small influence on the identified crack size and could safely be ignored. For

the case of the drum, a crack size of $\alpha = 30^\circ$ must be considered as the lower limit below which reliable crack detection and identification is not possible.

Simultaneous identification of crack size and location was attempted using multi-variable optimization algorithms. Here, it was shown that the difficulty in finding the solution to the inverse problem using optimization lies in the fact that the true solution does not always coincide with the global minimum of the objective function. In most of the investigated cases the true solution was located at a local minimum close-by to the global minimum. Furthermore, the ability of the optimization algorithm to converge to the true solution was highly dependent on the starting point, requiring a series of optimization attempts to find the global minimum. Surprisingly, the gradient based algorithms performed much better than in the single-variable case. Nonetheless, Nelder-Mead and trust region approaches are considered more reliable in solving this type of problem.

While some of the difficulties of multi-variable optimization may be overcome by employing more suitable optimization algorithms, consecutive optimization runs or adapting convergence criteria, the computational requirements remain high and there is no guarantee for a satisfactory solution. At the same time, this technique provides only little insight into neighbourhood around the global minimum. Therefore, it must be recognized that from a practical point of view a broad picture of the region around the global minimum will provide better information with respect to crack identification than a single solution point representing the exact global minimum. De-coupling of the identification of crack size and location addresses this point. De-coupling is achieved by making use of the limited number of discrete possible crack locations. A single-variable inverse problem is solved at every crack location and a confidence measure is assigned to each identified crack. The machine operator is then provided with an identified crack size and a confidence value in this solution for every investigated crack location. It is conceivable to remove locations with low confidence value from the list to further limit the amount of unnecessary information. The important point is that for machine operator and maintenance personnel the exact crack size and location is of minor importance. More critical is information regarding the probability of the existence of a crack,

approximate crack size with respect to critical crack size and approximate crack location, e.g., in which machine component might the crack exist. This type of information will provide significant aid to answer questions such as whether to keep running, when to schedule the next service interval, or whether to shut down immediately.

7.2 Outlook

There are several important aspects of crack identification based on vibration monitoring that have not been addressed in this study. For instance, while the nodal crack force approach is capable of handling the simulation of high speed rotors, this type of application has not been studied experimentally or in the inverse problem of crack identification. However, high speed rotating machinery, just as low speed rotors, are an important application for crack identification systems. The slow rotating pressure washer drum was chosen as sample application because it was believed that ignoring inertia effects will initially simplify the necessary evaluation of experimental crack models and the initial implementation of a crack identification procedure using inverse analysis. It is also true that a slow rotating drum provided a more cost effective approach for this initial step in developing crack identification technology. The positive results recommend future work be extended to high speed rotor applications. Furthermore, there have been indications in the literature suggesting that crack identification in high speed rotating machinery is actually easier than that for slow rotating machinery since inertia effects tend to amplify the vibration response, even if modeling of the dynamic behaviour will be more difficult.

Another important point is the reliance on a previously recorded comparison vibration signature or data trending. Data trending refers to the observation of changes in vibration signals over a specific time window rather than a comparison to a single previously recorded reference signature. In the field, the likelihood of the vibration signature of a "healthy" rotor to change due to a change in running conditions, such as normal wear of components or vibration from surrounding machinery, is much greater than under lab conditions, and data trending has been the preferred choice to eliminate noise and other non-essential vibration components. Therefore, an important step in the inverse problem

of crack identification will be the implementation of trended vibration measurements to act as a baseline signature rather than a single reference measurement. For this, measurements have to be taken either directly in the field, or lab conditions have to simulate field conditions more closely.

However, the requirement of continuously monitoring trended data cannot be viewed as all negative. It must be recognized that crack identification, as presented in this study, was the result of a "snapshot" analysis at a single point in time. In practice this would not be the case. Tracking the vibration signature history should provide an additional source of information. For instance, a steadily rising 2/rev. vibration amplitude may indicate a crack while an increase in 1/rev. amplitude together with a decrease in 2/rev. amplitude may point to an unbalance problem, even though at a certain point in time the "snapshot" vibration signatures are identical. Additional information could be provided by other condition monitoring techniques such as oil analysis or thermal imaging. The information from a variety of sources could be tied together and used by a higher level expert system to evaluate the type of malfunctioning. Detailed analysis submodules could be invoked to investigate the severity and exact location of the developing fault. It is believed that further developments in using historic data in the crack identification process together with the development and interfacing of hierarchical condition monitoring modules will be the key components leading to the successful application of this technology in the field.

BIBLIOGRAPHY

1. Goldman, S., *Vibration Spectrum Analysis*, Industrial Press, New York, USA, 1999.
2. Bently, D. E. and Muszynska, A., "Detection of Rotor Cracks," Proceedings of the 15th Turbomachinery Symposium, Texas A&M, Corpus Christi, TX, pp. 129-139, 1986.
3. McCracken, J. and Brose, W. R., "Risk Assessment Method for LP Disc Attachments with Stress Corrosion Cracking," Proceedings of the 1997 International Joint Power Generation Conference, Denver, USA, **32** (2), pp. 383-390, 1997.
4. Advanced Information Institute, "Predictive and Preventive Maintenance," Seminar February 2002, Vancouver, Canada, 2002.
5. Bevilacqua, M. and Braglia, M., "The analytical hierarchy process applied to maintenance strategy selection," *Reliability Engineering and System Safety*, **70**, pp. 71-83, 2000.
6. Boulahbal, D., Farid Golnaraghi, M. and Ismail, F., "Amplitude and phase wavelet maps for the detection of cracks in geared systems," *Mechanical Systems and Signal Processing*, **13** (3), pp. 423-436, 1999.
7. Irving, P. E., Strutt, J. E., Hudson, R. A., Allsop, K. and Strathern, M., "The contribution of fatigue usage monitoring systems to life extension in safe life and damage tolerant designs," *The Aeronautical Journal*, **103** (1030), pp. 589-595, 1999.
8. Matthews, M. S., "Picking up the vibrations for life extension," *Nuclear Engineering International*, **35**, pp. 44-45, 1990.
9. Valenti, M., "Aftermarket services reveal a gold mine for gas turbine manufacturers," *ASME News*, **18** (7), p. 1,7, July 1999.
10. Kippels, D., "Wenn der Service Ingenieur auf Internet Dienstreise geht," *VDI-Nachrichten*, Nr. 13, pp. 13, 2000.
11. VDI nachrichten, "Maschinendaten automatisch im Griff," *VDI nachrichten* Nr. 29, p. 18, July 23, 1999.
12. Kacprzynski, G. J. and Roemer, M. J., "Health Management Strategies for 21st Century Condition-Based Maintenance Systems," Proceedings of COMADEM 2000, Houston, USA, pp. 245-256, 2000.
13. McClung R.C., Leverant, G.R., Wu, Y.-T., Millwater, H.R., Chell, G.G., Kuhlman, C.J., Lee, Y.-D., Riha, D.S., Johns, S.R. and McKeighan, P.C., "Development of a Probabilistic Design System for Gas Turbine Rotor Integrity," Proceedings of the Seventh International Fatigue Congress (FATIGUE '99), Beijing, China, pp. 2655-2660, 1999.

14. Lin, C. C. and Wang, H. P., "Performance Analysis of Rotating Machinery using Enhanced Cerebellar Model Articulation Controller (E-CMAC) Neural Networks," *Computers ind. Engng*, **30** (2), pp. 227-242, 1996.
15. Broek, D., *Elementary engineering fracture mechanics*, Kluwer Academic Publishers, Dordrecht, The Netherlands, 1986.
16. Maintenance Technology, "2001 Vibration Analysis Guide," *Maintenance Technology*, **14** (4), 2001.
17. ANSI "Mechanical Vibration of Large Rotating Machines with Speed Range from 10 to 200 rev/s – Measurement and Evaluation of Vibration Severity *in situ*," ANSI S2.41-1985.
18. Kippels, D., "Wälzlager-Diagnose online," *VDI-Nachrichten*, Nr. 39, pp. 29, 1999.
19. Maintenance Technology, "2001 Condition Monitoring Software Guide," *Maintenance Technology*, October, pp. 30-31, 2001.
20. Klein, U. and Lülff, G., "Grundlagen rechnergestützter Maschinenüberwachung und praktische Anwendungen," *VDI Berichte 846*, VDI-Verlag, Düsseldorf, Germany, pp. 217-232, 1990.
21. Scheibel, J. R., Imam, I., Ebben, T. G., and Blomgren, R., "An expert system-based, on-line rotor crack monitor for utility steam turbines," Proceedings of the 51st American Power Conference, Chicago, IL, pp. 369-380, 1989.
22. Safizadeh, M.S., Lakis, A.A. and Thomas, M., "Using Short-Time Fourier Transforms in Machinery Diagnosis," *International Journal of COMADEM*, **3** (1), pp. 5-16, 2000.
23. Dimarogonas, A. D., "Dynamic response of cracked rotors," General Electric Co., Schenectady, NY, 1970
24. Pafelias, T., "Dynamic behavior of a cracked rotor," Technical Information Series, General Electric Co., No. DF-74-LS-79, 1974.
25. Gasch, R., "Dynamisches Verhalten des Laval-Läufers mit angerissenem Wellenquerschnitt," *VDI Berichte 269*, VDI-Verlag, Düsseldorf, Germany, 1976.
26. Henry, T. A. and Okah-Avae, B. E., "Vibrations in cracked shafts," *Vibrations in Rotating Machinery*, The Institution of Mechanical Engineers, London, U. K., pp. 123-128, 1976.
27. Mayes, I. W. and Davies, W. G. R., "A method of calculating the vibrational behavior of coupled rotating shafts containing a transverse crack," *Vibrations in Rotating Machinery*, The Institution of Mechanical Engineers, London, U. K., pp. 17-27, 1980.
28. Mayes, I. W. and Davies, W. G. R., "The vibrational behavior of a rotating shaft system containing a transverse crack," *Vibrations in Rotating Machinery*, The Institution of Mechanical Engineers, London, U. K., pp. 53-64, 1976.
29. Grabowski, B., "Das Schwingungsverhalten eines angerissenen Turbinenläufers," *VDI Bericht, 320*, VDI-Verlag, Düsseldorf, Germany, pp. 31-36, 1978.

30. Gasch, R., Person, M., and Weitz, B., "Dynamic behaviour of the Laval rotor with a cracked hollow shaft – a comparison of crack models," TecIMECH Conference of Vibration in Rotating Machinery, C314/88, Edinburgh, UK, pp. 463-472, 1988.
31. Dimarogonas, A. D., and Papadopolous, C. A., "Vibration of Cracked Shafts in Bending," *Journal of Sound and Vibration*, **91** (4), pp. 583-593, 1983.
32. Dimarogonas, A. D. and Massouros, G., "Torsional Vibration of a Shaft with a Circumferential Crack," *Engineering Fracture Mechanics*, **15** (3-4), pp. 439-444, 1981.
33. Dimarogonas, A. D. and Paipetis, S. A., *Analytical Methods in Rotor Dynamics*, Applied Science Publishers, London, U. K., 1983.
34. Dimarogonas, A. D., and Papadopolous, C. A., "Crack Detection in Turbine Rotors," *Dynamics of Rotating Machinery*, Hemisphere Publishing Corp., New York, USA, pp. 227-239, 1988.
35. Papadopoulos, C. A. and Dimarogonas, A. D., "Coupled longitudinal and bending vibrations of a cracked shaft," *Journal of Vibration, Acoustics, Stress, and Reliability in Design*, **110**, pp. 1-8, 1988.
36. Chondros, T. G. and Dimarogonas, A. D., "Dynamic Sensitivity of Structures to Cracks," *Journal of Vibration, Acoustics, Stress, and Reliability in Design*, **111**, pp. 251-256, 1989.
37. Papadopoulos, C. A. and Dimarogonas, A. D., "Coupled Vibration of Cracked Shafts," *Journal of Vibrations and Acoustics*, **114**, pp. 461-467, 1992.
38. Changhe, L., Bernasconi, O., and Xenophontidis, N., "A Generalized Approach to the Dynamics of Cracked Shafts," *Journal of Vibration, Acoustics, Stress, and Reliability in Design*, **111**, pp. 257-263, 1989.
39. Bently D. E. and Muszynska, A., "Early detection of shaft cracks on fluid-handling machines," ASME. Fluids Engineering Division (Publication) FED v46, New York, USA, pp.53-58, 1986.
40. Muszynska, A., "Shaft crack detection," 7th Machinery Dynamics Seminar, Canada, 1982.
41. Imam, I., Azzaro, S. H., Bankert, R. J., and Scheibel, J., "Development of an On-line Rotor Crack Detection and Monitoring System," *Journal of Vibration, Acoustics, Stress, and Reliability in Design*, **111**, pp. 241-250, 1989.
42. Liao, M., and Gasch, R., "Crack detection in rotating shafts - an experimental study," IMechE Conference of Vibration in Rotating Machinery, C432/106, pp. 289-295, 1992.
43. Gasch, R., "A survey of the dynamic behaviour of a simple rotating shaft with a transverse crack," *Journal of Sound and Vibration*, **160** (2), pp. 313-332, 1993.
44. Schmied, J. and Krämer, E., "Vibrational behaviour of a rotor with a cross-sectional crack," *Vibrations in Rotating Machinery*, The Institution of Mechanical Engineers, London, U. K., pp. 183-192, 1984.

45. Wen, B. C. and Wang, Y. B., "Theoretical research, calculation and experiments of cracked shaft dynamic response," *Vibrations in Rotating Machinery*, The Institution of Mechanical Engineers, London, U. K., pp. 473-478, 1988.
46. Iwatsubo, T., Arii, S., and Oks, A., "Detection of a transverse crack in a rotor shaft by adding external force," *Vibrations in Rotating Machinery*, The Institution of Mechanical Engineers, London, U. K., pp. 275-282, 1992.
47. Nelson, H.D. and Nataraj, C., "The Dynamics of a Rotor System with a Cracked Shaft," *Journal of Vibration, Acoustics, Stress, and Reliability in Design*, **108**, pp. 189-196, 1986.
48. Ratan, S., Baruh, H., and Rodriguez, J., "On-line identification and location of rotor cracks," *Journal of Sound and Vibration*, **194** (1), pp. 67-82, 1996.
49. Wauer, J., "Modelling and Formulation of Equations of Motion for Cracked Rotating Shafts," *International Journal of Solids and Structures*, **26** (8), pp. 901-914, 1990.
50. Maxwell, J.H. and Rosario, D.A., Using Modeling to predict vibration from a shaft crack, *Proceedings of COMADEM 2001*, Elsevier, pp. 243-250, 2001.
51. Dirr, B. and Schmalhorst, B., "Crack Depth Analysis of a Rotating Shaft by Vibration Measurement," *Journal of Vibration, Acoustics, Stress, and Reliability in Design*, **110**, pp. 158-164, 1988
52. Schmalhorst, B., "Experimentelle und theoretische Untersuchungen zum Schwingungsverhalten angerissener Rotoren," VDI Fortschrittberichte, Reihe 11: Schwingungstechnik Nr 117, VDI Verlag, Düsseldorf, Germany, 1989
53. Schmalhorst, B., "Laboratory and theoretical investigations of the vibrational behavior of a uniform rotor with a transverse crack," The Third International Symposium on Transport Phenomena and Dynamics of Rotating Machinery, Volume 2: Dynamics, Honolulu, USA, 1990.
54. Schmalhorst, B., "Numerical Simulation of Cracked Rotor's Vibrations Due to Measured Crack Shapes," *Dynamics of Rotating Machinery*, Hemisphere Publishing Co., New York, USA, pp. 211-225, 1988.
55. Keiner, H. and Gadala, M. S., "3D Finite Element Analysis of a Cracked Rotor," Proceedings of the 1st Canadian Conference on Nonlinear Solid Mechanics, Victoria, Canada, pp. 366-374, 1999.
56. Bush, A. J., "Experimentally Determined Stress-intensity Factors for Single-edge-crack Round Bars Loaded in Bending," *Experimental Mechanics*, **16**, pp. 249-257, 1976.
57. Hamidi, L., Piaud, J.-B., and Massourd, M., "A study of cracks influence on the modal characteristics of rotors," IMechE Conference of Vibration in Rotating Machinery, C432/066, pp. 283-288, 1992.
58. Ishida, Y. and Hirokawa, K., "Internal Resonances of a Cracked Rotor," *JSME International Journal Series C*, **39** (2), pp. 225-233, 1996.

59. Ishida, Y., Ikeda, T., Yamamoto, T. and Masuda, N., "Vibrations of a Rotating Shaft Containing a Transverse Crack," *JSME International Journal Series III*, **31** (1), pp. 22-29, 1988.
60. Meng, G. and Gasch, R., "Stability and Stability Degree of a Cracked Flexible Rotor Supported on Journal Bearings," *Journal of Vibration and Acoustics*, **122**, pp. 116-125, 2000.
61. Takahashi, I., "Vibration and stability of a cracked shaft simultaneously subjected to a follower force with an axial force," *International Journal of Solids and Structures*, **35** (23), pp. 3071-3080, 1998.
62. Wu, M.-C. and Huang, S.-C., "Vibration and Crack Detection of a Rotor with Speed-Dependent Bearings," *International Journal of Mechanical Sciences*, **40** (6), pp. 545-555, 1998.
63. Zheng, G.T. and Leung, A.Y.T., "On the stability of cracked rotor systems," *Journal of the Chinese Society of Mechanical Engineers*, **19** (1), pp 125-133, 1998.
64. Meng, G. and Hahn, E. J., "Dynamic Response of a Cracked Rotor With Some Comments on Crack Detection," *Journal of Engineering for Gas Turbines and Power*, **119**, pp. 447-455, 1997.
65. Chan, R. K. C. and Lai, T. C., "Digital simulation of a rotating shaft with a transverse crack," *Applied Mathematical Modeling*, **19**, pp. 411-420, 1995.
66. Tsai, T. C. and Wang, Y. Z., "The vibration of a multi-crack rotor," *International Journal of Mechanical Sciences*, **39** (9), pp. 1037-1053, 1997.
67. Tsai, T.-C., and Wang, Y.-Z., "The Vibration of a Rotor with a Transverse Open Crack," Proceedings of the National Science Council, Republic of China, Part A - Physical Science and Engineering, pp. 372-383, 1998.
68. Keiner, H. and Gadala, M.S., "Comparison of Different Modelling Techniques to Simulate the Vibration of a Cracked Rotor," *Journal of Sound and Vibration*, **254** (5), pp. 1012-1024, 2002.
69. Lee C.-W., Yun, J.-S., and Jun, O. S., "Modeling of a Simple Rotor With a Switching Crack and Its Experimental Verification," *Journal of Vibration and Acoustics*, **114**, pp. 217-225, 1992.
70. Darpe, A. K., Chawla, A. and Gupta, K., "Analysis of the response of a cacked Jeffcott rotor to axial excitation," *Journal of Sound and Vibration*, **249** (3), pp. 429-445, 2002.
71. Zheng J., Mi Z., and MENG G., "Bifurcation and Chaos Response of a Nonlinear Cracked Rotor," *International Journal of Bifurcation and Chaos*, **8** (3), pp. 597-607, 1998.
72. Sekhar, A. S., "Vibration characteristics of a cracked rotor with two open cracks," *Journal of Sound and Vibration*, **233** (4), pp. 497-512, 1999.

73. Sekhar, A. S. and Balaji Prasad, P., "Dynamic Analysis of a Rotor System Considering a Slant Crack in the Shaft," *Journal of Sound and Vibration*, **208** (3), pp. 457-474, 1997.
74. Sekhar, A. S., "Condition Monitoring of a Rotor System having a Slant Crack in the Shaft," *Noise and Vibration Worldwide*, **30** (3), pp. 23-31, 1999.
75. Ichimonji, M. and Watanabe, S., "The Dynamics of a Rotor System with a Shaft Having a Slant Crack," *JSME International Journal Series III*, **31** (4), pp. 712-718, 1988.
76. Nink, A. and Stölben, H., "Rißerkennung an Vertikalrotoren mittels frequenz-selektiver Schwingungsüberwachung," *VDI Berichte 846*, VDI-Verlag, Düsseldorf, Germany, pp. 29-46, 1990.
77. Mohiuddin, M. A. and Khulief, Y. A., "Modal characteristics of cracked rotors using a conical shaft finite element," *Computer Methods in Applied Mechanical Engineering*, **162**, pp. 223-247, 1998.
78. Parhi, D. R. and Behera, A. K., "Vibrational Analysis of Cracked Rotor in Viscous Medium," *Journal of Vibration and Control*, **6**, pp. 331-349, 2000.
79. Wauer, J., "On the dynamics of cracked rotors: A literature survey," *Applied Mechanics Review*, **43** (1), 1990.
80. Dimarogonas, A. D., "Vibration of Cracked Structures: A State of the Art Review," *Engineering Fracture Mechanics*, **55** (5), pp. 831-857, 1996.
81. Lees, A. W. and Friswell, M. I., "Crack Detection in Asymmetric Rotors," *Key Engineering Materials*, **167-168**, pp. 246-255, 1999.
82. Doyle, James F., "Determining the Size and Location of Transverse Cracks in Beams," *Experimental Mechanics*, September 1995, pp. 272-280, 1995.
83. Sekhar, A. S. and Prabhu, B. S., "Condition Monitoring of Cracked Rotors Through Transient Response," *Mechanical Machinery Theory*, **33** (8), pp. 1167-1175, 1998.
84. Mühlenfeld, K., "Der Wellenriß im stationären Betrieb von Rotoren," Dissertation, Technische Universität Berlin, Berlin, Germany, 1992.
85. Rothkegel, W., "Rißerkennung bei Rotoren durch Schwingungsüberwachung," *VDI-Fortschrittsberichte, Reihe 11: Schwingstechnik*, Nr. 180, 1993.
86. Tsyfansky, S.L. and Beresnevich, V.I., "Detection of Fatigue Cracks in Flexible Geometrically Non-linear Bars By Vibration Monitoring," *Journal of Sound and Vibration*, **213** (1), pp. 159-168, 1998.
87. Dirr, B. O., Popp, K. and Rothkegel, W., "Detection and simulation of small transverse cracks in rotating shafts," *Archive of Applied Mechanics*, **64**, pp. 206-222, 1994.
88. Gelman, L., Giunta, G., Perego, G. and Petrunin, I., Usage of the Fourier components for Fatigue Crack Diagnostics, *Proceedings of COMADEM 2002*, COMADEM International, pp. 163-170, 2002.

89. Franklin, W., Bently, D. E., Goldman, P., and Muszynska, A., "Early Cracked Shaft Detection in Pumps Using Rotor Lateral Vibration Analysis," *Pumping Machinery Symposium - Proceedings of the 1997 ASME Fluids Engineering Summer Meeting, Vancouver, Canada, 1997.*
90. Rizos, P.F., Aspragathos, N. and Diamarogonas, A.D., "Identification of Crack Location and Magnitude in a Cantilever Beam from Vibration Modes," *Journal of Sound and Vibration*, 138 (3), pp. 381-388, 1990.
91. Ruotolo, R. and Surace, C., "Damage Assessment of Multiple Cracked Beams: Numerical Results and Experimental Validation," *Journal of Sound and Vibration*, 206 (4), pp. 567-588, 1997.
92. Kuang, J. H. and Huang, B. W., "The effect of blade crack on mode localization in rotating bladed disks," *Journal of Sound and Vibration*, 227 (1), pp. 85-103, 1999.
93. Seibold, S. and Weinert, K., "A Time Domain Method for the Localization of Cracks in Rotors," *Journal of Sound and Vibration*, 195 (1), pp. 57-73, 1996.
94. Nandwana, B. P. and Maiti, S. K., "Detection of the location and size of a crack in stepped cantilever beams based on measurements of natural frequencies," *Journal of Sound and Vibration*, 203 (3), pp. 435-446, 1997.
95. Nandwana, B. P. and Maiti, S. K., "Modelling of vibration of beam in presence of inclined edge or internal crack for its possible detection based on frequency measurements," *Engineering Fracture Mechanics*, 58 (3), pp. 193-205, 1997.
96. Rivola, A. and White, P. R., "Bispectral analysis of the bilinear oscillator with application to the detection of fatigue cracks," *Journal of Sound and Vibration*, 216 (5), pp. 889-910, 1998.
97. Fonte, M.A. and Freitas, M.M., "Semi-Elliptical Fatigue Crack Growth under Rotating or Reversed Bending Combined with Steady Torsion," *Fatigue and Fracture of Engineering Materials and Structures*, 20 (6), pp. 895-906, 1997.
98. Muszynska, A., Goldman, P., and Bently, D. E., "Torsional/lateral vibration cross-coupled responses due to shaft anisotropy: a new tool in shaft crack detection," *Vibrations in rotating machinery*, The Institution of Mechanical Engineers, London, U. K., pp. 257-262, 1992.
99. Hertzberg, R.W., *Deformation and Fracture Mechanics of engineering materials*, J. Wiley & Sons, New York, USA, 1995.
100. Tamura, A., Iwata, Y., and Sato, H., "Unstable vibration of a rotor with a transverse crack," *Vibrations in Rotating Machinery*, The Institution of Mechanical Engineers, London, U. K., pp. 647-653, 1988.
101. Iwata, Y., Sato, H., Takamori, Y., and Tamura, A., "Vibration of a Rotor with Imitation Crack," *Nippon Kikai, Gakkai Ronbunshu C Hen*, 54 (503), pp. 1433-1438, 1988.
102. Sanderson, A. F. P., "The vibration behaviour of a large steam turbine generator during crack propagation through the generator rotor," *Vibrations in Rotating*

- Machinery*, The Institution of Mechanical Engineers, London, U. K., pp. 263-273, 1992.
103. Lindley, T.C., "Fatigue Cracking in Power Plant," Proceedings of the Fifth International Conference on Fatigue and Ftigue Thresholds, Montreal, Canada, 1993.
 104. Bicego, V., Lucon, E., Rinaldi, C., and Crudeli, R., "Failure analysis of a generator rotor with a deep crack detected during operation: fractographic and fracture mechanics approach," *Nuclear Engineering and Design*, **188**, pp. 173-183, 1999.
 105. Parida, N. and Tarafder, S., "Failure analysis of turbo-generator of a 10 MW captive power plant," *Engineering Failure Analysis*, **8**, pp. 303-309, 2001.
 106. Mahmoud, M.A. and Kiefa, M.A., "Neural network solution of the inverse vibration problem," *NDT&E International*, **32**, pp.91-99, 1999.
 107. Gadala, M.S. and Keiner, H., "Design, Optimization and On-line Vibration Monitoring of a Pressure Washer Drum," ESDA 2002: DES055, Istanbul, Turkey, 2002.
 108. Chen, C. K. and Lin C. Y., "Failure analysis of brass rotor bars," *Engineering Failure Analysis*, **8** (20), pp. 293-301, 2001.
 109. Lancha, A.M, Serrano, M. and Gomez Briceño, D., "Failure analysis of a condensate pump shaft," *Engineering Failure Analysis*, **6**, pp. 337-353, 1999.
 110. Lancha, A.M., Lapeña, J., Serrano, M. and Gorrochategui, I., "Metallurgical failure analysis of a BWR recirculation pump shaft," *Engineering Failure Analysis*, **7**, pp. 333-346, 2000.
 111. Vodopivec, F., Vojvodovic-Tuma, J., Breskvar, B. and Arzensek, B., "Cracking and fracture of valve shafts in the secondary steam circuit of a nuclear power plant. A case investigation." *Nuclear Engineering and Design*, **207**, pp. 223-230, 2001.
 112. Tjernberg, A., "Fatigue lives for induction hardened shafts with subsurface crack initiation," *Engineering Failure Analysis*, **9**, pp. 45-61, 2002.
 113. Kubo, S., "Inverse Problems Related to the Mechanics and Fracture of Solids and Structures," *JSME International Journal, Series I*, **31** (2), pp. 157-166, 1988.
 114. Brandon, J., Nonlinear Vibration of Cracked Structures: Perspectives and Horizons, *The Shock and Vibration Digest*, **32** (4), pp. 273-280, 2000.
 115. Stavroulakis, G. E., *Inverse and Crack Identification Problems in Engineering Mechanics*, Kluwer Academic Publishers, Dordrecht, The Netherlands, 2000.
 116. Abdalla, K.M. and Stavroulakis, G.E., "A back-propagation neural network model for semi-rigid steel connections based on experimental data," *Microcomputers in Civil Engineering*, **10** (2), pp. 77-87.
 117. Stavroulakis, G.E. and Antes H., "Crack detection by elastostatic measurements: a neural network approach based on BEM modelling," *IUTAM Symposium on Discretization, Methods in Structural Mechanics II*, Kluwer Academic Publishers, Dordrecht, The Netherlands, pp. 199-206, 1999.

118. Hsieh, S.-C. and Mura, T., "Nondestructive cavity identification in structures," *International Journal of Solids and Structures*, **30** (12), pp. 1579-1587, 1993.
119. Hwu, C. and Liang, Y.C., "Hole/Crack Identification by Static Strains from Multiple Loading Modes," *AIAA Journal*, **39** (2), pp. 315-324, 2001.
120. Liu, C.T. and Chen W.J., "Some Advances in Study of Crack Identification Problems," *Key Engineering Materials*, **145-149**, pp. 375-380, 1998.
121. Ulrich, T. W., Moslehy, F. A., and Kassab, A. J., "A BEM based pattern search solution for a class of inverse elastostatic problems," *International Journal of Solids and Structures*, **33** (15), pp. 2123-2131, 1996.
122. Schnur, D. S. and Zabras, N., "Finite element solution of two-dimensional inverse elastic problems using spatial smoothing," *International Journal for Numerical Methods in Engineering*, **30**, pp. 57-75, 1990.
123. Schnur, D. S., "An inverse method for determining elastic material properties and a material interface," *International Journal for Numerical Methods in Engineering*, **33**, pp. 2039-2057, 1992.
124. Keat, W.D., Larson, M.C. and Verges, M.A., "Inverse method of identification for three-dimensional subsurface cracks in a half-space," *International Journal of Fracture*, **92**, pp. 253-270, 1998.
125. Larson, M.C., Verges, M.A. and Keat, W.D., "Nondestructive identification of three-dimensional embedded cracks in finite bodies by inversion of surface displacements," *Engineering Fracture Mechanics*, **63**, pp. 611-629, 1999.
126. Mccullough, A. D. B. and Gadala, M. S., "On the Finite Element Analysis of Inverse Problem in Fracture Mechanics," *Engineering Computations*, **16**, pp. 481-502, 1999.
127. Maniatty, A., Zabras, N. and Stelson, K., "Finite Element Analysis of Some Inverse Elasticity Problems," *Journal of Engineering Mechanics*, **115** (6), pp. 1303-1317, 1989.
128. Burczynski, T. and Beluch, W., "The identification of cracks using boundary elements and evolutionary algorithms," *Engineering Analysis with Boundary Elements*, **25**, pp. 313-322, 2001.
129. Suh, M.-W. and Shim, M.-B., "Crack Identification using Hybrid Neuro-Genetic Technique," *Journal of Sound and Vibration*, **238** (4), pp. 617-635, 2000.
130. Gladwell, G.M.L., "Inverse vibration problems for finite-element models," *Inverse Problems*, **13**, pp. 311-322, 1997.
131. Gladwell, G.M.L., "Inverse Finite Element Vibration Problems," *Journal of Sound and Vibration*, **211** (2), pp. 309-324, 1999.
132. Gladwell, G.M.L., *Inverse problems in scattering: an introduction*, Kluwer Academic Publishers, Dordrecht, The Netherlands, 1993.
133. Gladwell, G.M.L., *Inverse problems in vibration*, Kluwer Academic Publishers, Dordrecht, The Netherlands, 1986.

134. Lebedev, L.P., Vorovich, I.I. and Gladwell, G.M.L., *Functional analysis: applications in mechanics and inverse problems*, Kluwer Academic Publishers, Dordrecht, The Netherlands, 1996.
135. Seibold, S., A Multi-hypothesis approach to damage detection of rotating Machines, Proceedings of the 15th International Modal Analysis Conference, Orlando, USA, pp. 863-869, 1997.
136. He, Y., Guo, D. and Chu, F., "Using genetic algorithms and finite element methods to detect shaft crack for rotor-bearing systems," *Mathematics and Computers in Simulation*, **57**, pp. 95-108, 2001.
137. He, Y., Guo, D. and Chu, F., "Using genetic algorithm to detect and configure shaft crack for rotor-bearing system," *Computer Methods in Applied Mechanical Engineering*, **190**, pp. 5895-5906, 2001.
138. Keiner, H. and Gadala, M. S., "Vibration of a Cracked Drum - Comparison of 3D Finite Element Results with Experimental Measurements," Proceedings of COMADEM 2000, Houston, USA, pp. 119-126, 2000.
139. Carlson, G. J., Imam, I., Azzaro, S. H. and Scheibel, J. R., "An Expert System On-line Rotor Crack Monitoring and Diagnostic System," Proceedings of the 1988 ASME International Computers in Engineering Conference and Exhibition, San Francisco, USA, pp. 361-366, 1988.
140. ANSYS Rev. 5.5, ANSYS, Inc., Canonsburg, PA, USA, 1999.
141. Bathe, K.-J., *Finite Element Procedures*, Prentice-Hall, Upper Saddle River, USA, 1996.
142. Fok, C.M., "New Design for Pressure Washer Drums," Master of Science Thesis, Department of Mechanical Engineering, The University of British Columbia, 1997.
143. Labview Rev. 5.1, National Instruments Corporation, Austin, TX, USA, 1999.
144. MATLAB Rev. 5.3, The MathWorks, Inc., Natick, MA, USA, 1999.
145. Tang, T. "Online Crack Detection of Slowly Rotating Machinery," Master's Thesis, The University of British Columbia, Department of Mechanical Engineering, Vancouver, Canada, 2001.
146. Kelley, C.T., *Iterative Methods for Optimization*, SIAM, Philadelphia, USA, 1999.

APPENDIX

APPENDIX A

A.1 Element and material properties used in the 3D FE drum model

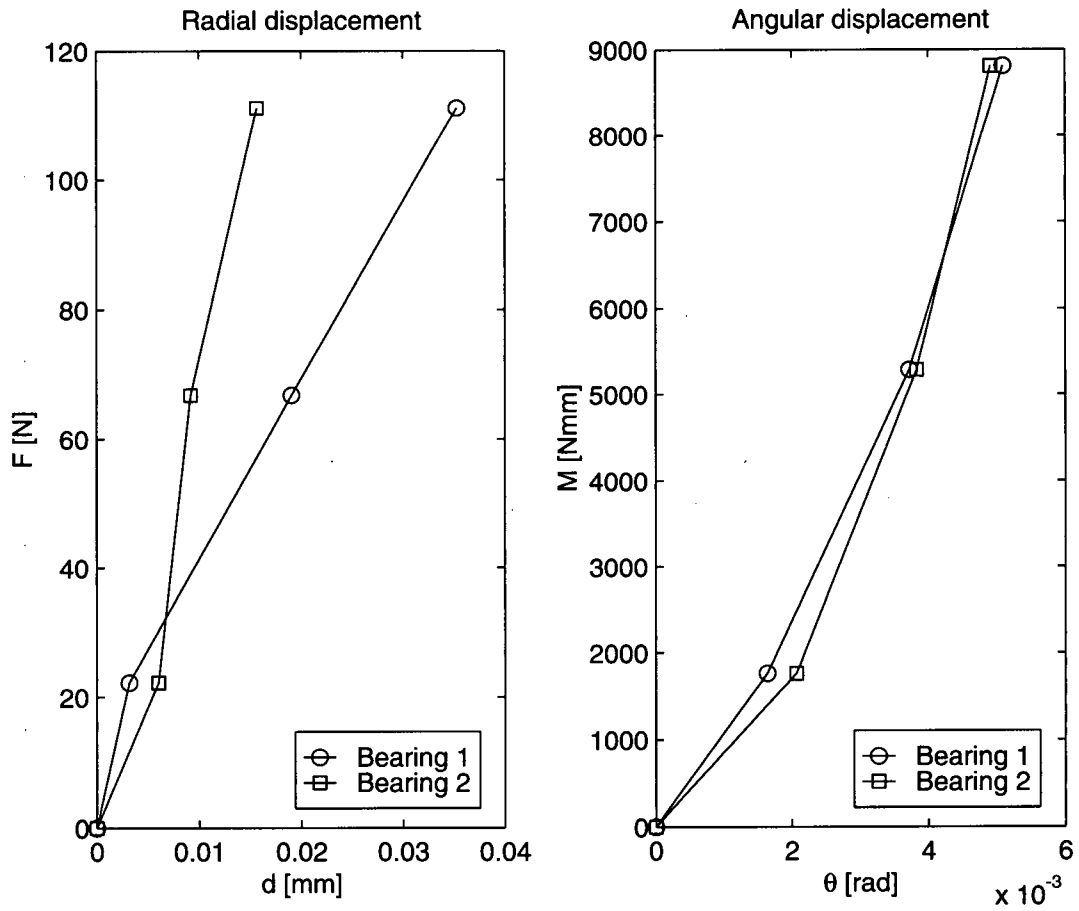
Element name	SOLID45	SHELL63	LINK1	COMBIN39	COMBIN14	MASS21
Type	3D solid	3D shell	3D spring	3D spring	3D spring	nodal mass
Number of nodes	8	4	2	2	2	1
DOF per node	3	6	3	2	2	3
Shape functions	linear	cubic	linear	N/A	N/A	N/A
Behaviour	linear	linear	linear	non-linear	linear	non-linear
Modeled components	shaft, hub	end plates, drum shell	radial bearing stiffness	(1)	(2)	bolt masses

(1) contact elements, rotational bearing stiffness (node de-coupling and contact element analysis)

(2) rotational bearing stiffness (nodal crack force approach)

Material	Aluminium 6061-T6	Steel AISI 316
Young's modulus	70 GPa	210 GPa
Poisson's ratio	0.33	0.3
Density	2700 kg/m ³	7800 kg/m ³

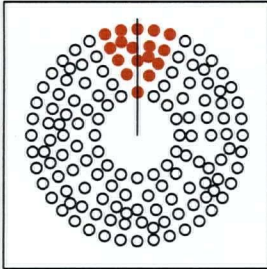
A.2 Measured and fitted bearing stiffness values



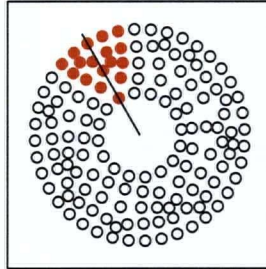
A.3 Simulated crack breathing using contact elements

$$\alpha = 45^\circ$$

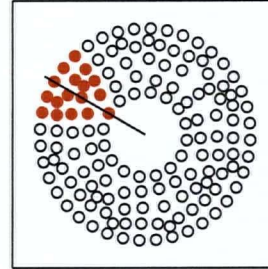
$$\Omega t = 0^\circ$$



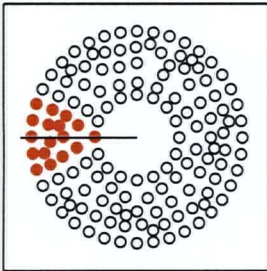
$$\Omega t = 30^\circ$$



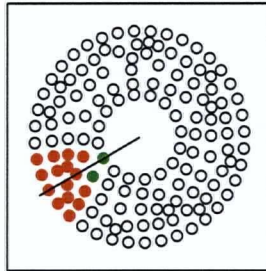
$$\Omega t = 60^\circ$$



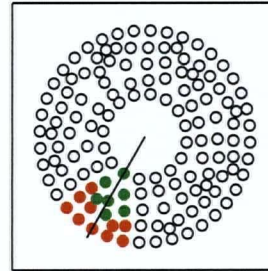
$$\Omega t = 90^\circ$$



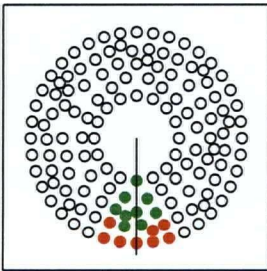
$$\Omega t = 120^\circ$$



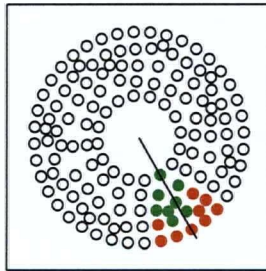
$$\Omega t = 150^\circ$$



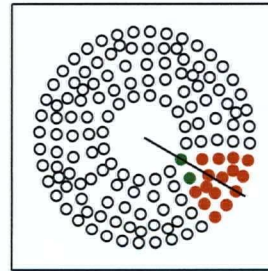
$$\Omega t = 180^\circ$$



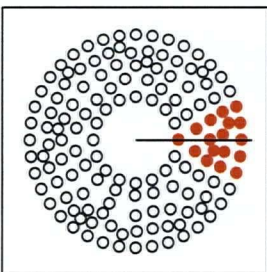
$$\Omega t = 210^\circ$$



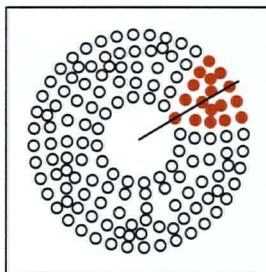
$$\Omega t = 240^\circ$$



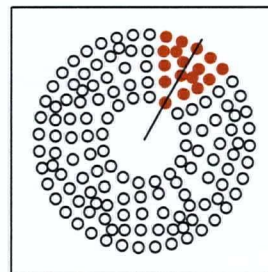
$$\Omega t = 270^\circ$$



$$\Omega t = 300^\circ$$

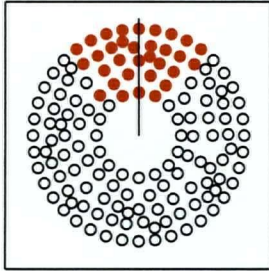


$$\Omega t = 330^\circ$$

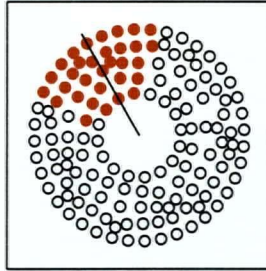


$$\alpha = 90^\circ$$

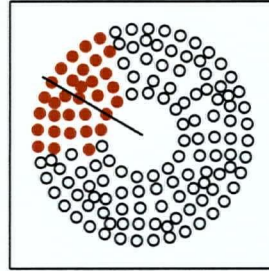
$$\Omega t = 0^\circ$$



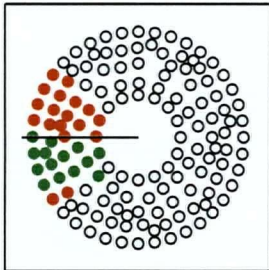
$$\Omega t = 30^\circ$$



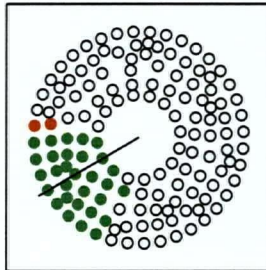
$$\Omega t = 60^\circ$$



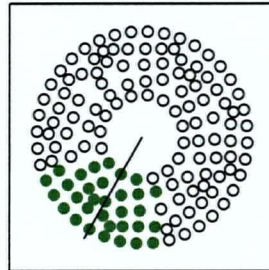
$$\Omega t = 90^\circ$$



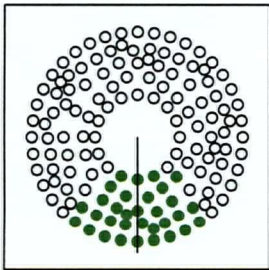
$$\Omega t = 120^\circ$$



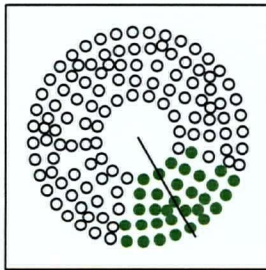
$$\Omega t = 150^\circ$$



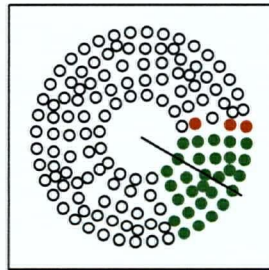
$$\Omega t = 180^\circ$$



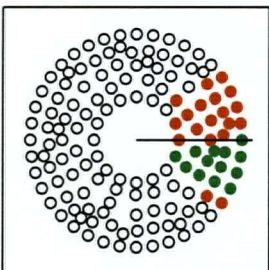
$$\Omega t = 210^\circ$$



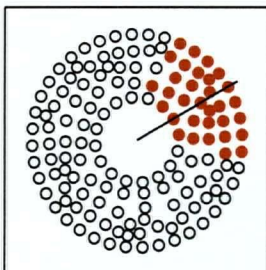
$$\Omega t = 240^\circ$$



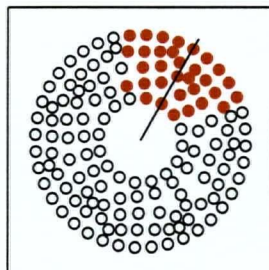
$$\Omega t = 270^\circ$$



$$\Omega t = 300^\circ$$

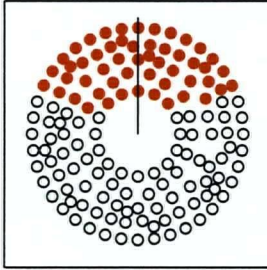


$$\Omega t = 330^\circ$$

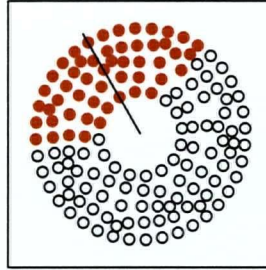


$$\alpha = 135^\circ$$

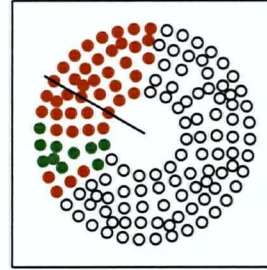
$$\Omega t = 0^\circ$$



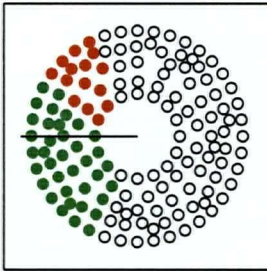
$$\Omega t = 30^\circ$$



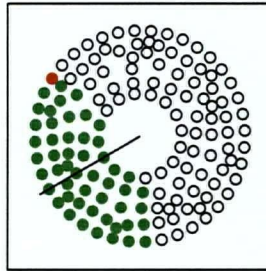
$$\Omega t = 60^\circ$$



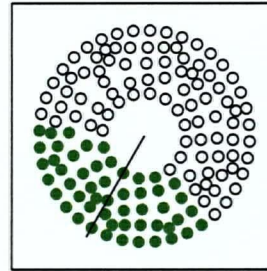
$$\Omega t = 90^\circ$$



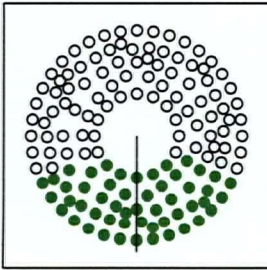
$$\Omega t = 120^\circ$$



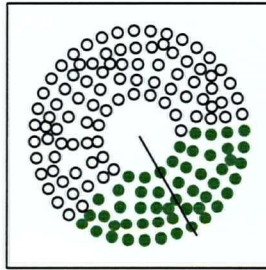
$$\Omega t = 150^\circ$$



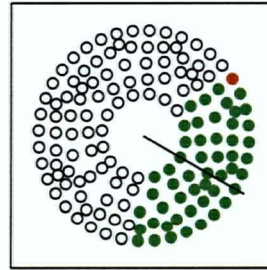
$$\Omega t = 180^\circ$$



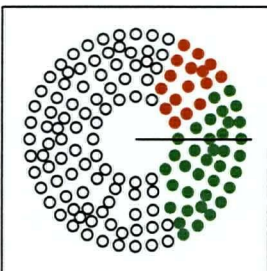
$$\Omega t = 210^\circ$$



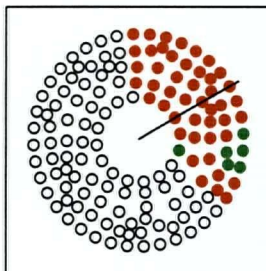
$$\Omega t = 240^\circ$$



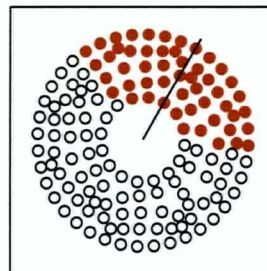
$$\Omega t = 270^\circ$$



$$\Omega t = 300^\circ$$

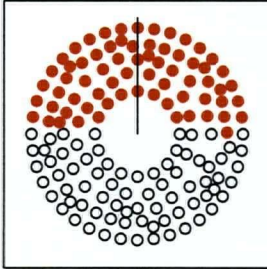


$$\Omega t = 330^\circ$$

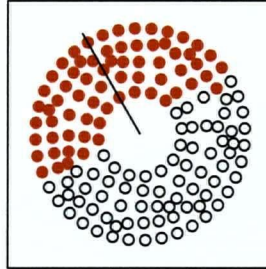


$$\alpha = 180^\circ$$

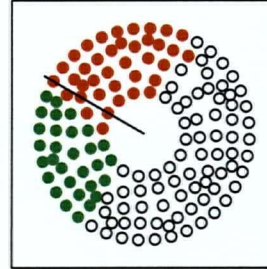
$$\Omega t = 0^\circ$$



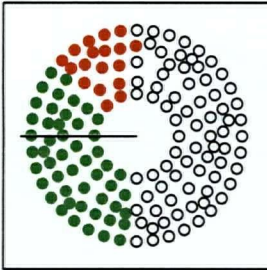
$$\Omega t = 30^\circ$$



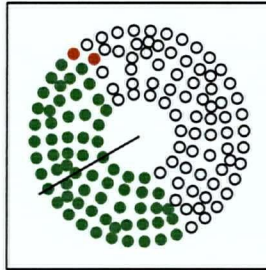
$$\Omega t = 60^\circ$$



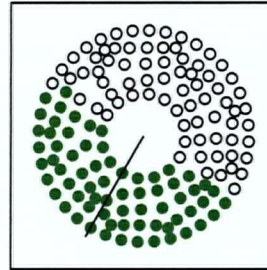
$$\Omega t = 90^\circ$$



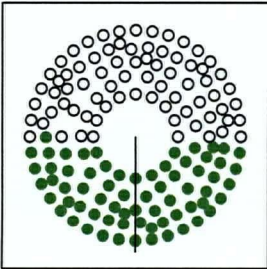
$$\Omega t = 120^\circ$$



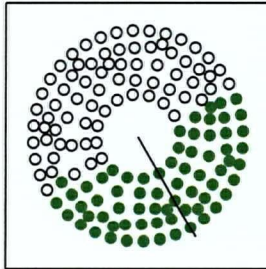
$$\Omega t = 150^\circ$$



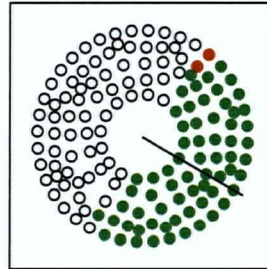
$$\Omega t = 180^\circ$$



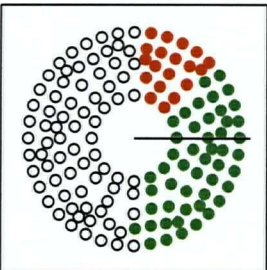
$$\Omega t = 210^\circ$$



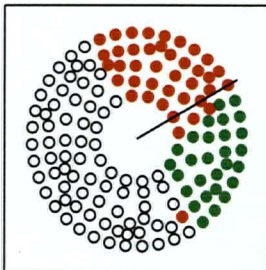
$$\Omega t = 240^\circ$$



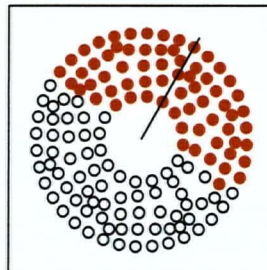
$$\Omega t = 270^\circ$$



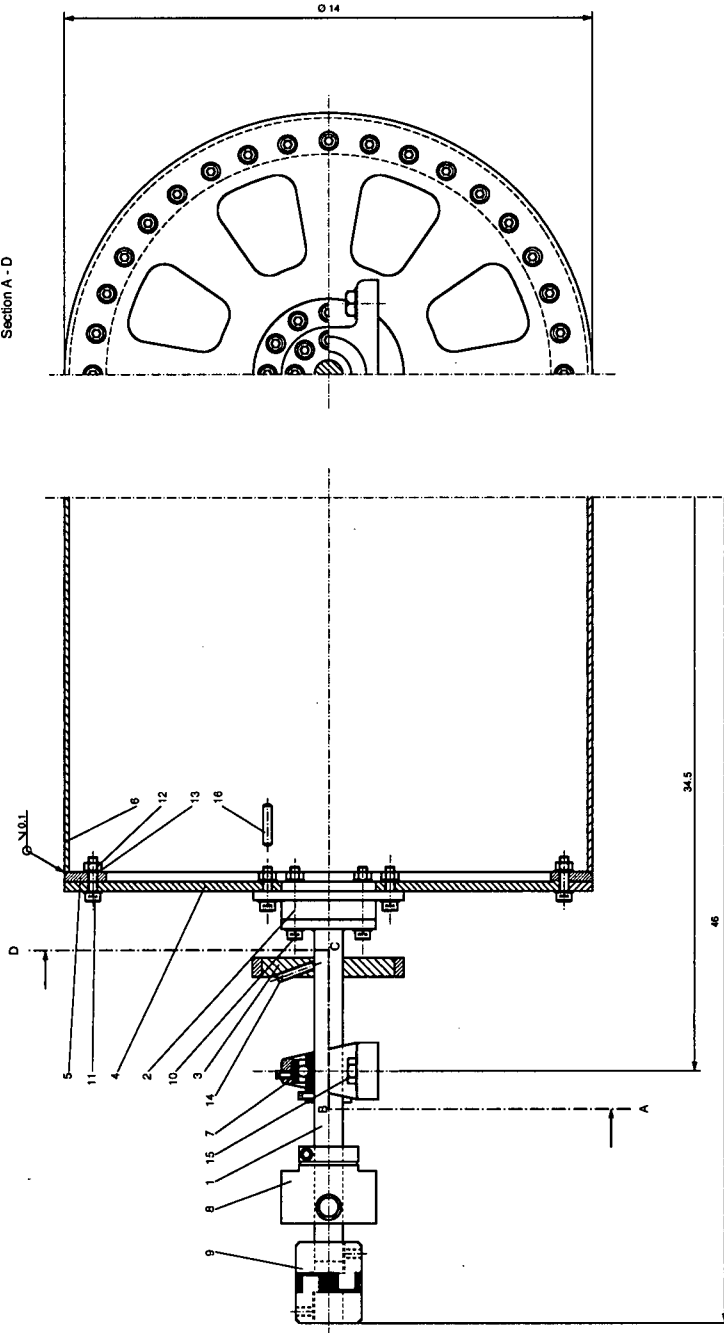
$$\Omega t = 300^\circ$$



$$\Omega t = 330^\circ$$

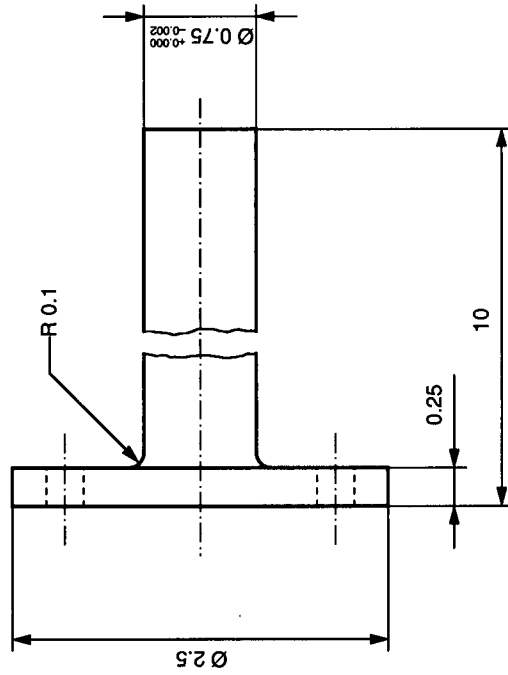
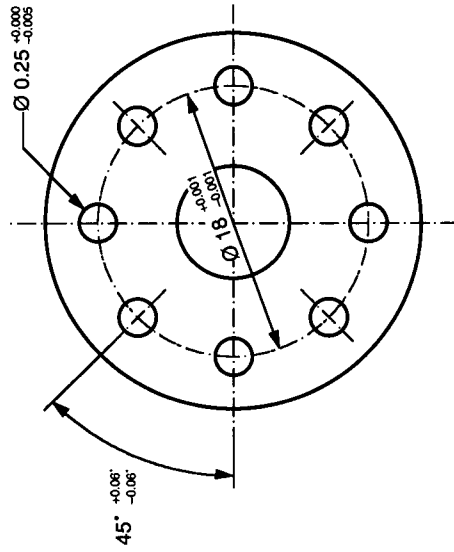


Section A - D



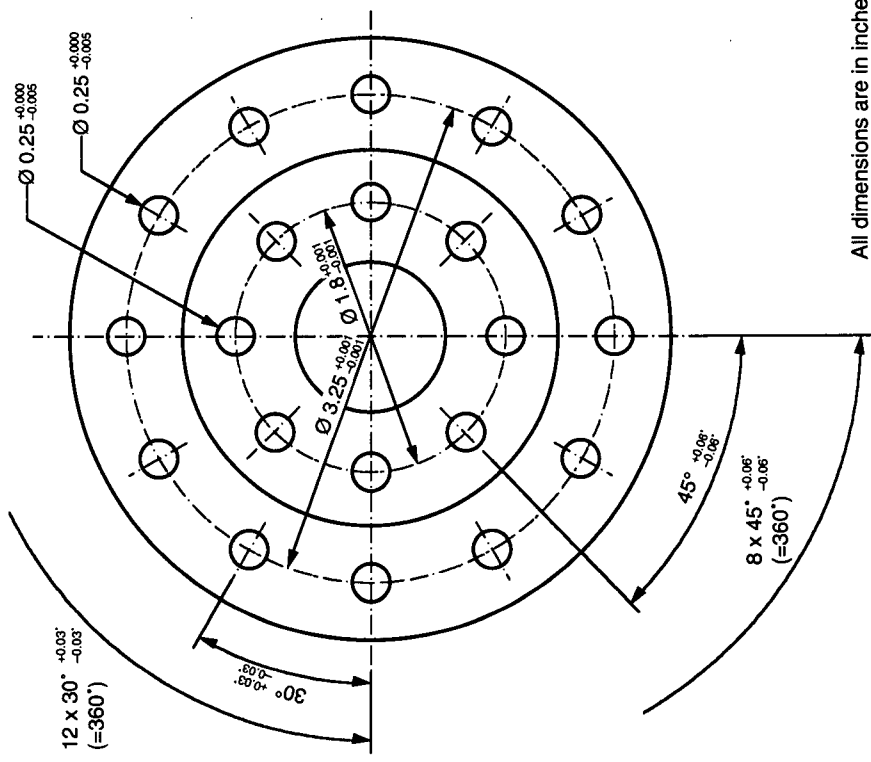
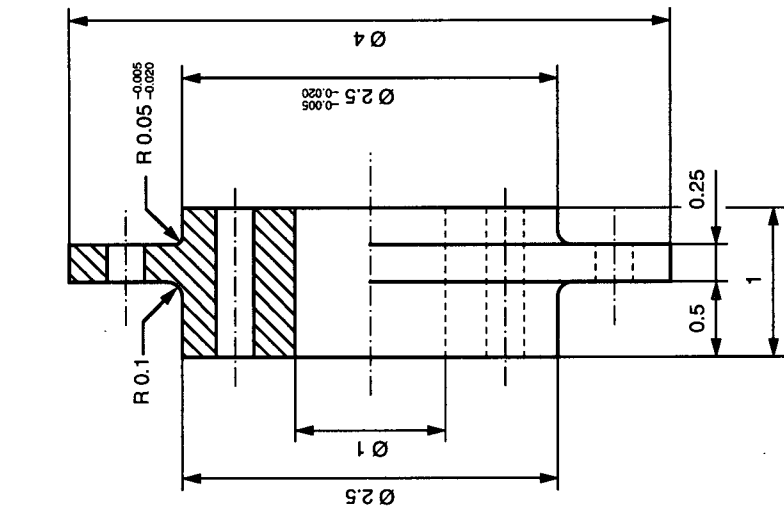
All dimensions are in inches.

Scale	1:2	Title	Rotor Specimen
Material	A1051-176	Class Number	1 - 00
Date	June 16, 2000	Author	USC - Mechanical Engineering
Drawn by	H. Kahrer		



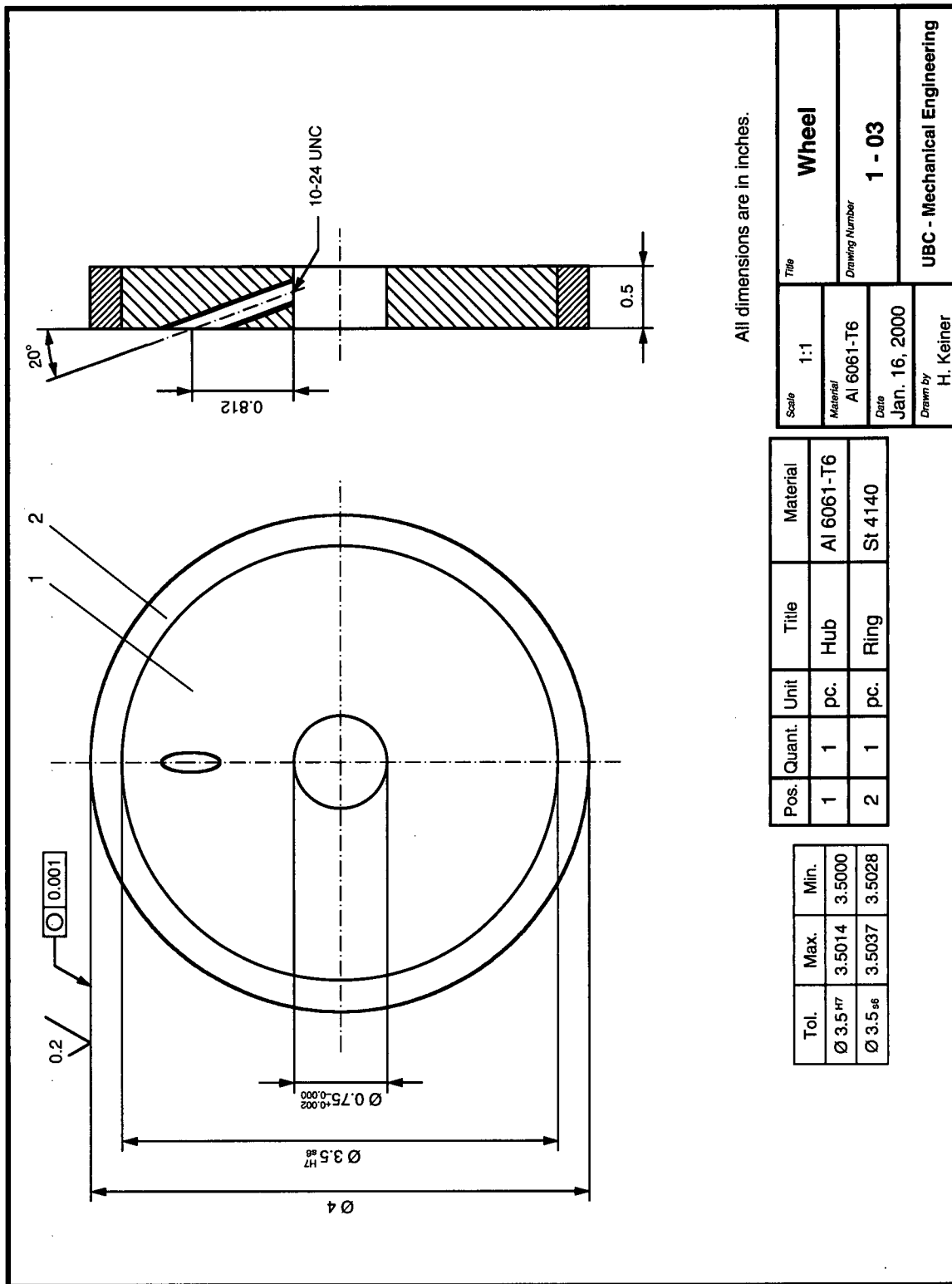
All dimensions are in inches.

Scale	1:1	Title	Shaft
Material	Al 6061-T6	Drawing Number	1 - 01
Date	Jan. 16, 2000	UBC - Mechanical Engineering	
Drawn by	H. Keiner		



All dimensions are in inches.

Scale	1:1	Title	Hub
Material	Al 6061-T6	Drawing Number	1 - 02
Date	Jan. 16, 2000	Drawn by	H. Keiner
UBC - Mechanical Engineering			

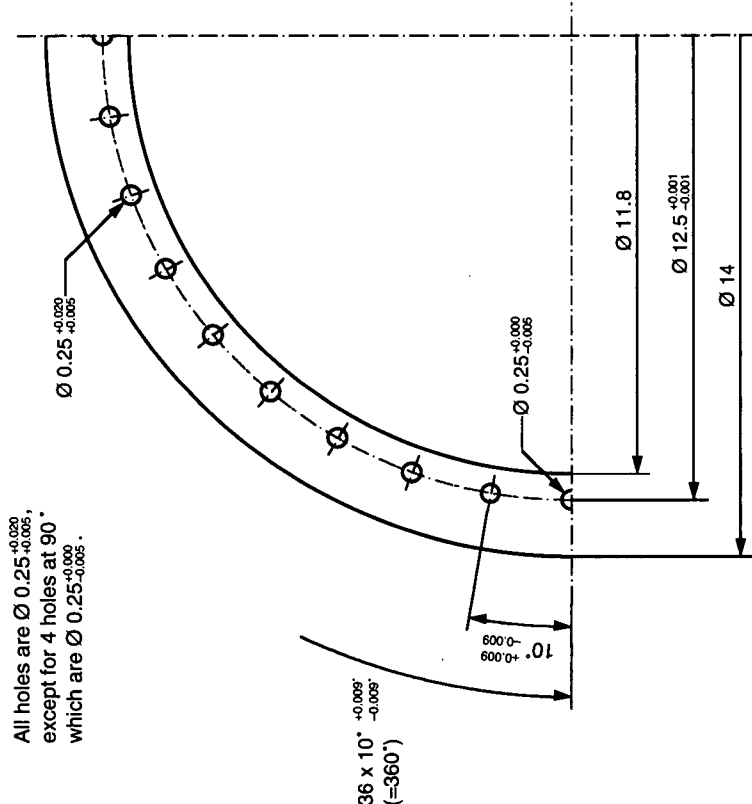
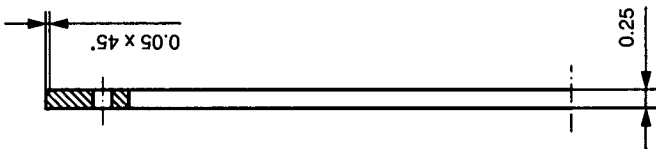


All dimensions are in inches.

Scale	1:1	Title	Wheel
Material	Al 6061-T6	Drawing Number	1 - 03
Date	Jan. 16, 2000	Drawn by	H. Keiner
UBC - Mechanical Engineering			

Pos.	Quant.	Unit	Title	Material
1	1	pc.	Hub	Al 6061-T6
2	1	pc.	Ring	St 4140

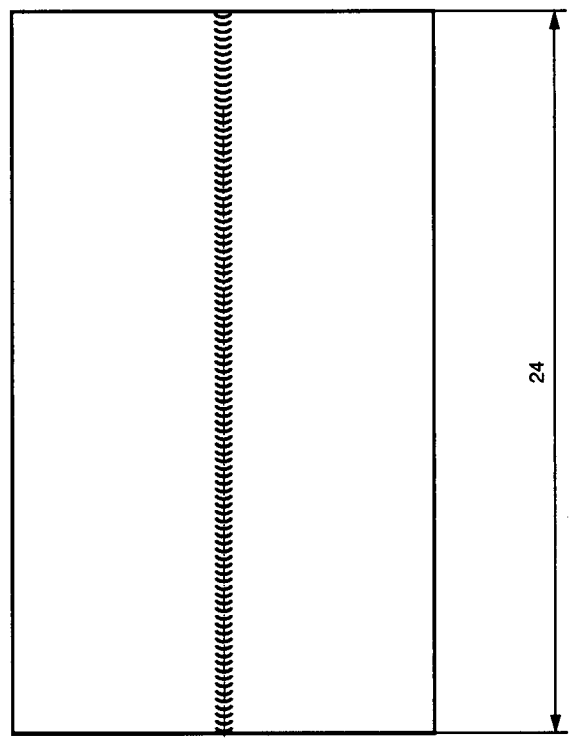
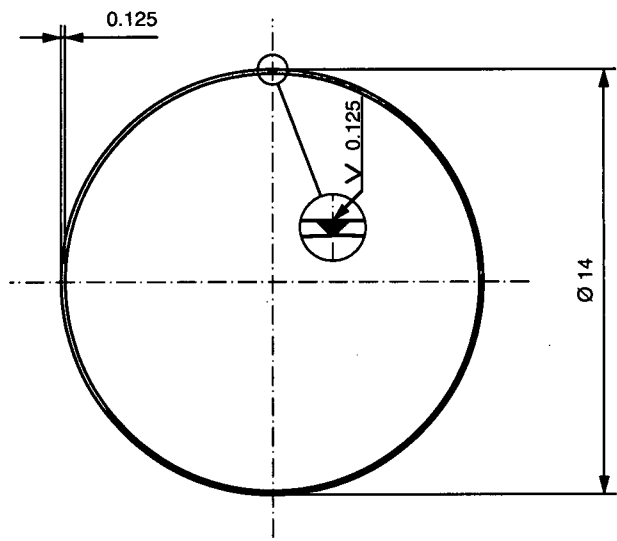
Tol.	Max.	Min.
$\varnothing 3.5_{H7}$	3.5014	3.5000
$\varnothing 3.5_{s6}$	3.5037	3.5028



All holes are Ø 0.25^{+0.005},
except for 4 holes at 90°
which are Ø 0.25^{+0.005}.

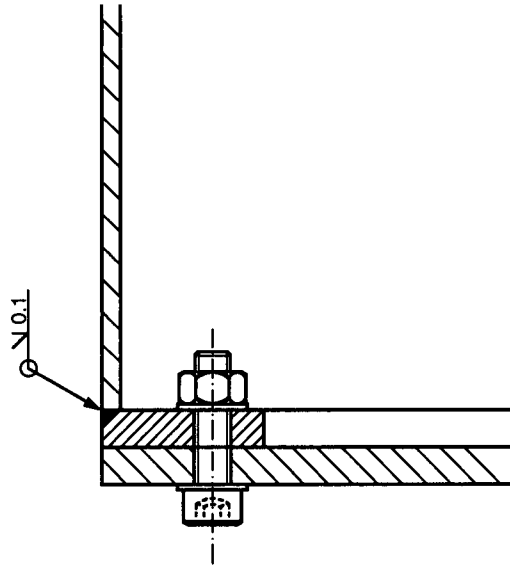
Scale	1:2	Title	Ring
Material	AI 5052-H32	Drawing Number	1 - 05
Date	Jan. 16, 2000	Drawn by	H. Keiner
UBC - Mechanical Engineering			

All dimensions are in inches.



Scale	1:5	Title	Drum
Material	Al 5052-H32	Drawing Number	1 - 06
Date	Jan. 16, 2000	Drawn by	H. Keiner
UBC - Mechanical Engineering			

All dimensions are in inches.



Scale	1:1	Title	Weld
Material	Al 6061-T6	Drawing Number	1 - 07
Date	Jan. 16, 2000	UBC - Mechanical Engineering	
Drawn by	H. Keiner		

B.2 Similarity analysis for the scaled-down pressure washer drum

Non-dimensional Analysis for a beam under bending load

$$E^* I^* w^{*''} = -M^* \quad (1)$$

$$\sigma^* = \frac{M^* R^*}{I^*} \Leftrightarrow M^* = \frac{\sigma^* I^*}{R^*} \quad (2)$$

$$\Rightarrow E^* I^* w^{*''} = -\frac{\sigma^* I^*}{R^*} \Leftrightarrow R^* E^* w^{*''} = -\sigma^* \quad (3)$$

Nondimensional variables:

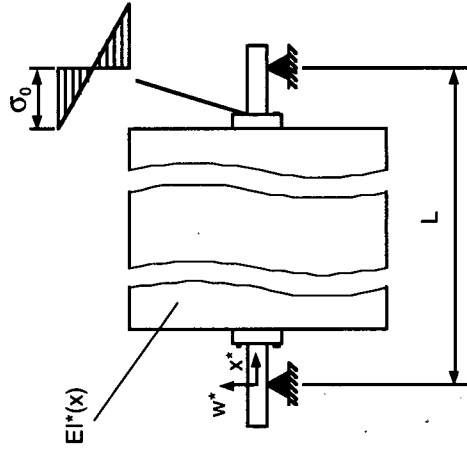
$$x^* = \frac{x}{L}, w = \frac{w^*}{L}, r = \frac{R^*}{L}, s = \frac{\sigma^*}{\sigma_0}, e = \frac{E^*}{E_0}$$

where:

L = length of rotor, σ_0 = nominal stress, E_0 = average Young's modulus

$$\frac{dw^*}{dx^*} = \frac{L}{L} \frac{dw}{dx} = w' \Rightarrow \frac{d^2 w^*}{dx^{*2}} = \frac{w''}{L}$$

where $\frac{E_0}{\sigma_0}$ is the non-dimensional constant $\left[\frac{\text{MPa}}{\text{MPa}} \right] = 1$.



Geometry

Geometric Scaling Factor ≈ 10

	Model	Real
R_shaft [mm]	10	150
R_hub [mm]	32	350
R_drum [mm]	178	2000
t_drum [mm]	3.5	20
L_shaft [mm]	125	420
L_hub [mm]	25	250
L_drum [mm]	520	8000
L [mm]	670	8670
I_shaft [mm ⁴]	7.854E+03	3.976E+08
I_hub [mm ⁴]	8.025E+05	1.148E+10
I_drum [mm ⁴]	6.201E+07	5.027E+11

Material Properties		
E_st [Mpa]	210000	
E_al [Mpa]	70000	

Nominal Young's Modulus		
E0 = (E(x))/l(x) [Mpa]	Model	Real
	209818	210000

Nominal Stress		
σ0 [MPa]	Model	Real
	80.93	81

Similitude		
E0 / σ0	Model	Real
	2.59E+03	2.59E+03

Res. Load	Model	Appl. Pressure	Real
-> F [N]	801	-> p [kPa]	31.95

B.3 Specifications of sensors and DAQ equipment

Proximity Probes: BENTLY 3300XL

Range	0 - 2 mm
Sensitivity	7.87 V/mm $\pm 5\%$
Repeatability	$\pm 0.01\%$ of full range
Output signal	0 - -24 V
Supply voltage	-24 V DC
Cable/Proximitator	5 m System

Angular Encoder: BEI-HS25F

Pulses per revolution	1024 = 0.352°
Signal steps with XOR-gate	4096 = 0.088°
Output signal	2 x 0-5 V, phaseshifted by 90°
1/rev. pulse	0 - 5 V pulse signal
Supply voltage	5 V DC

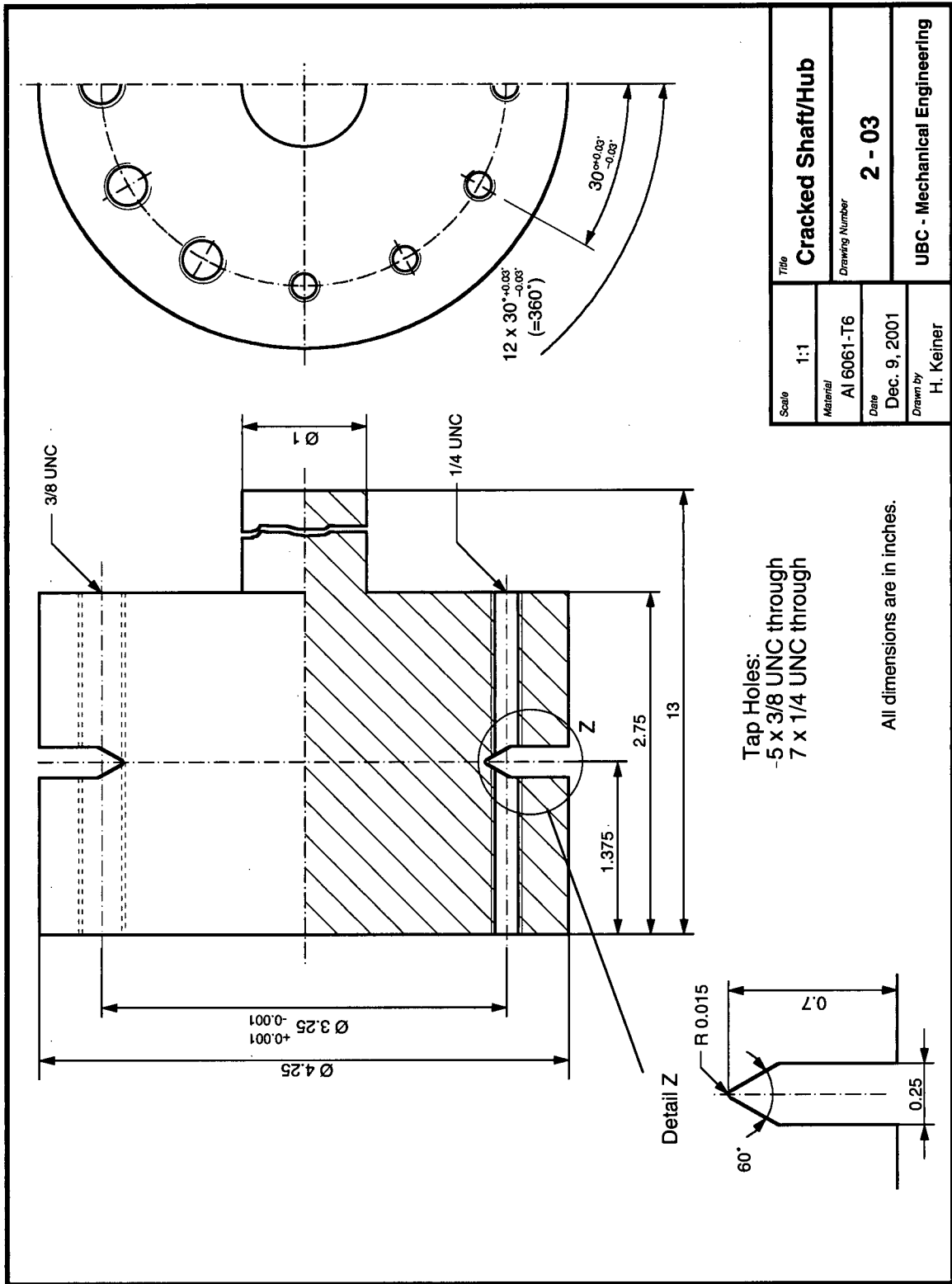
DAQ Board: IOTech DAQ-Board 2000

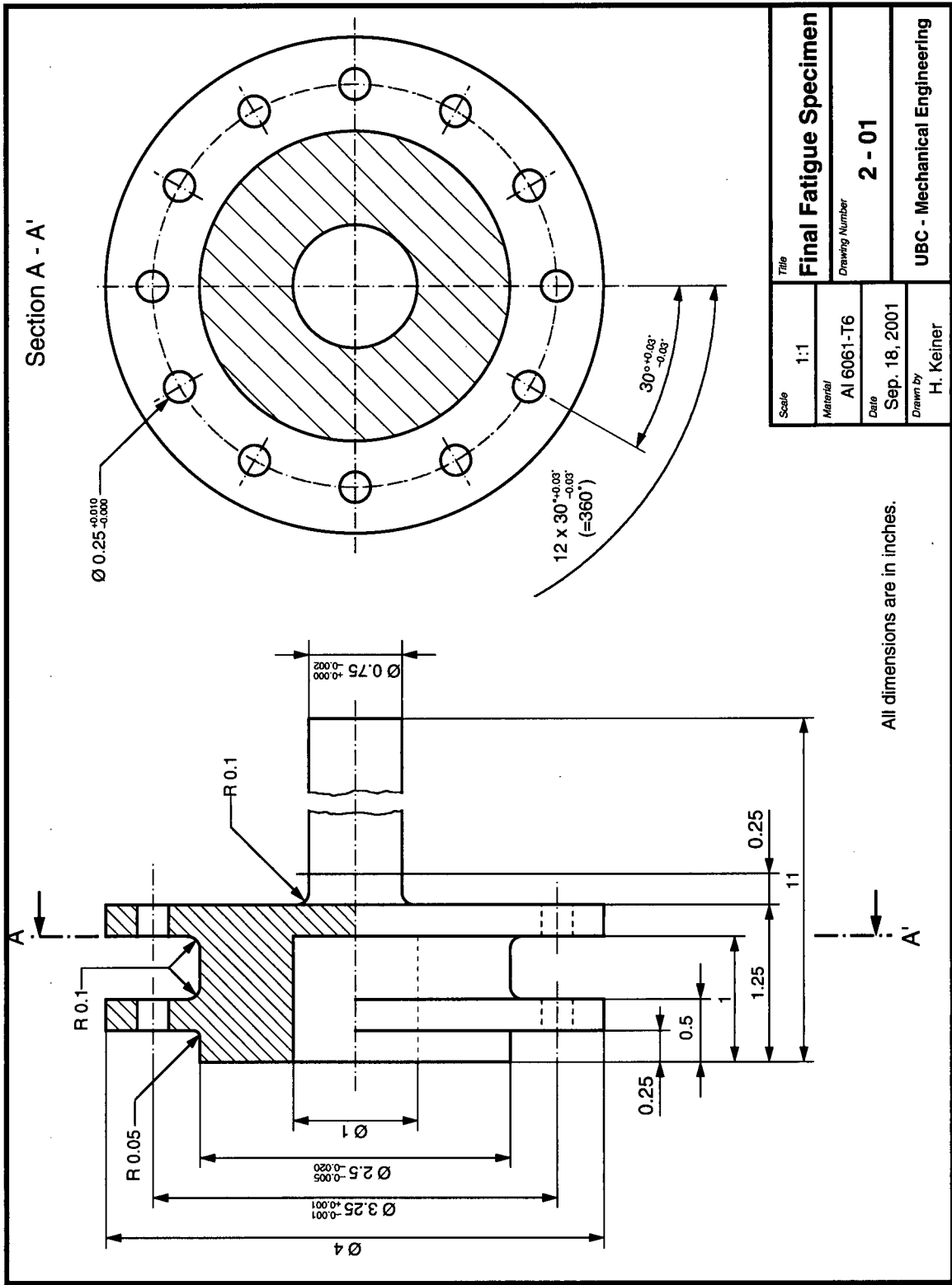
A/D converter	16 bit
Sample speed	200 kHz
Analogue input	$\pm 10V$, $\pm 5V$, 0-10V, 0-5V
Digital input	8 digital or 16 single ended inputs
Trigger	4 counters
Software drivers	analogue and digital
	C, Labview, Daqview

Low Pass Filter: IOTech DBK18

Filter characteristic	Butterworth
Cutoff frequency	5 Hz
Channels	4
Input voltage	$\pm 5V$
Error	$\pm 0.04\%$

B.5 Technical drawings of fatigue crack specimen



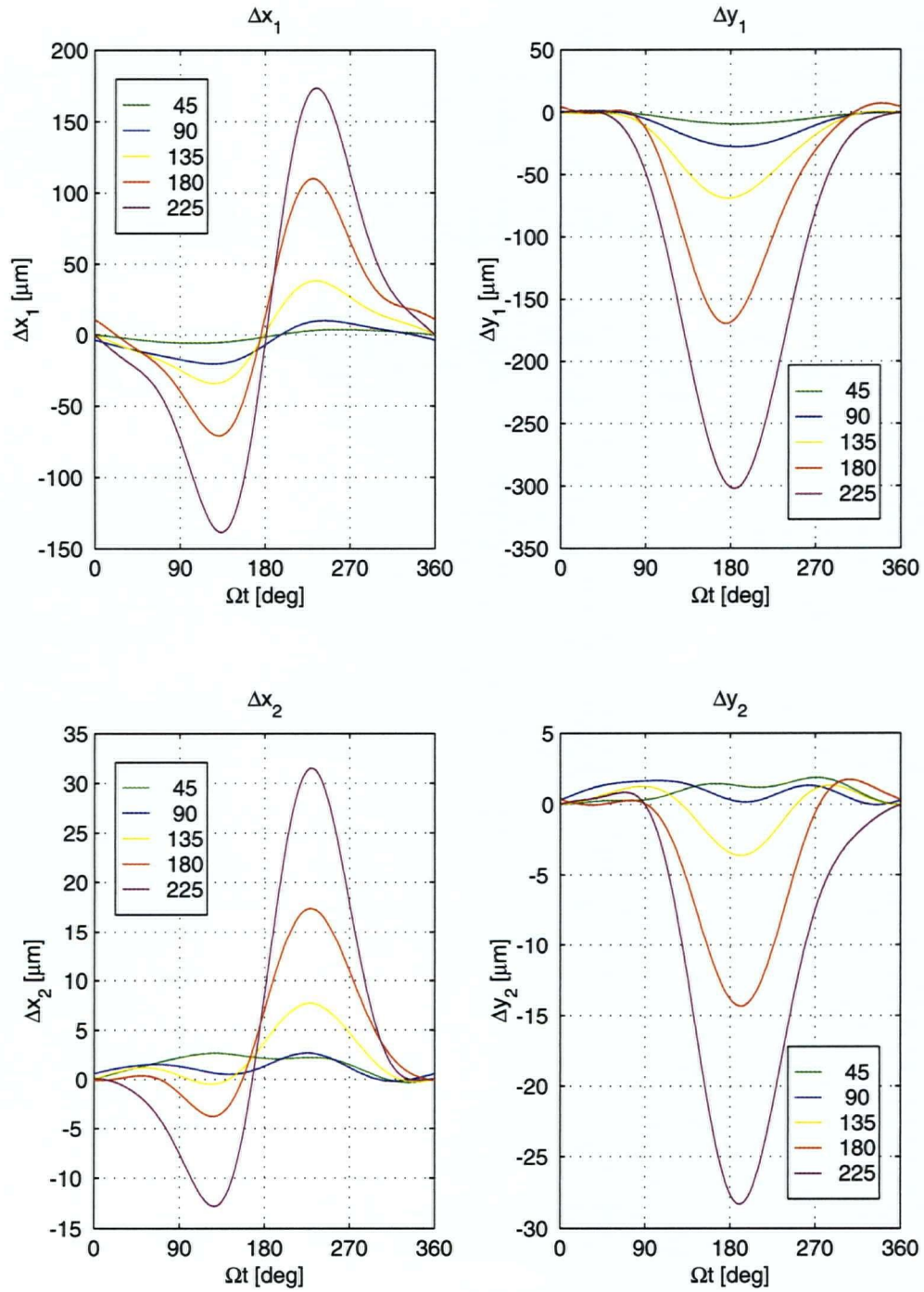


Scale	1:1	Title	Final Fatigue Specimen
Material	Al 6061-T6	Drawing Number	2 - 01
Date	Sep. 18, 2001	UBC - Mechanical Engineering	
Drawn by	H. Keiner		

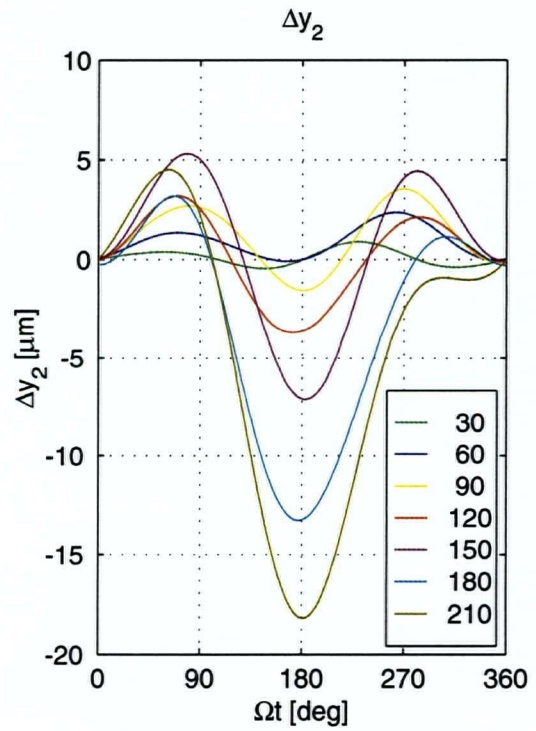
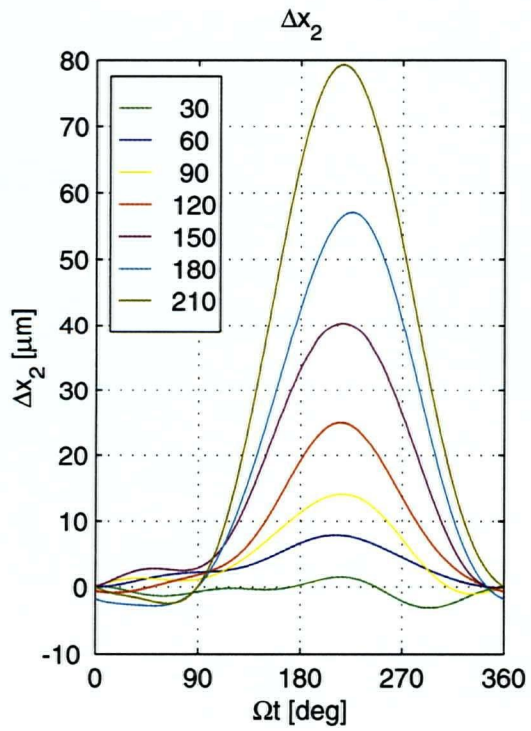
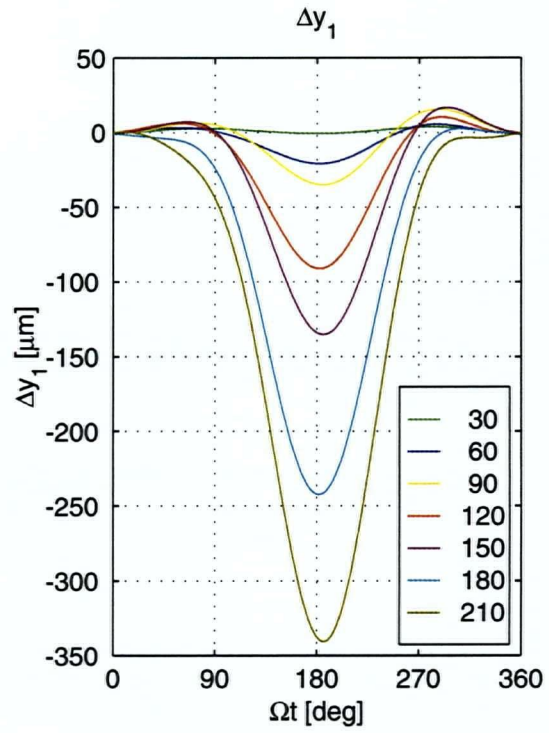
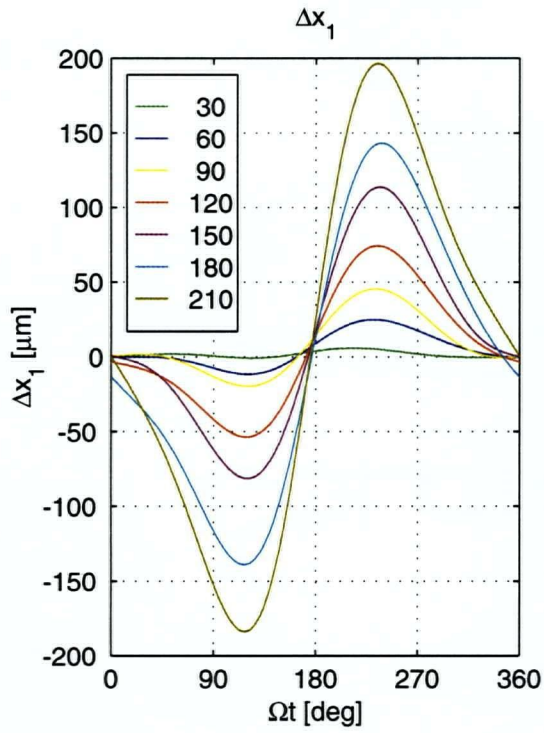
All dimensions are in inches.

B.6 Mean values of recorded vibration signals for a simulated crack using the bolt removal method

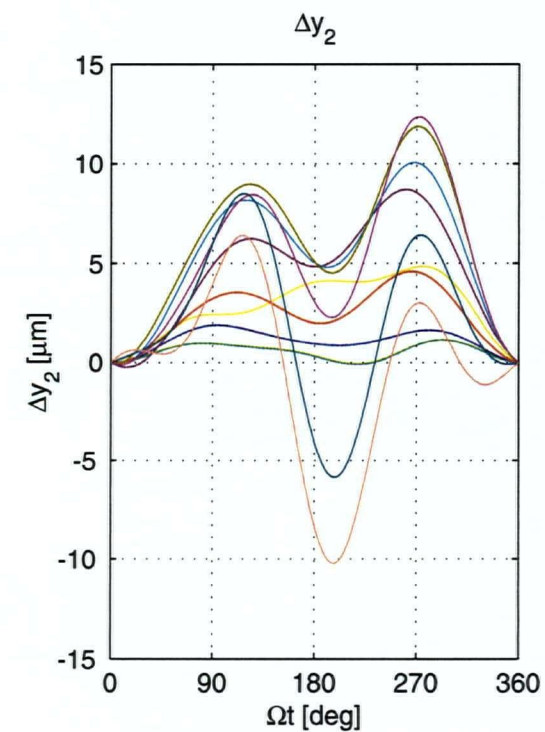
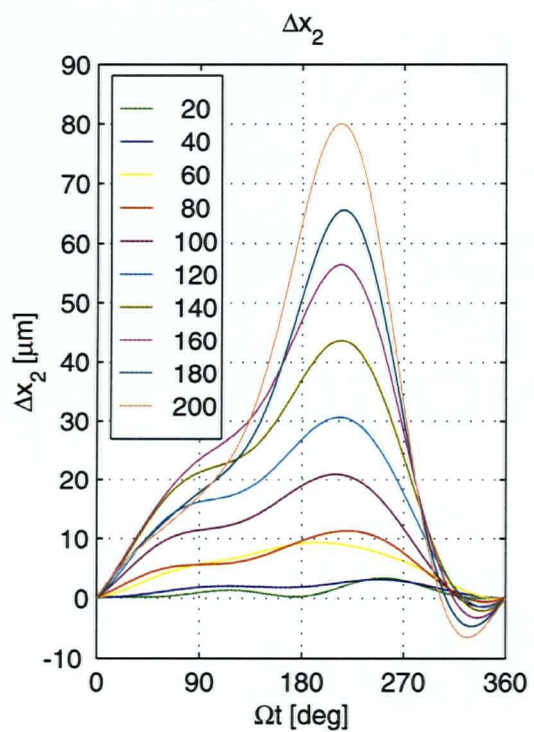
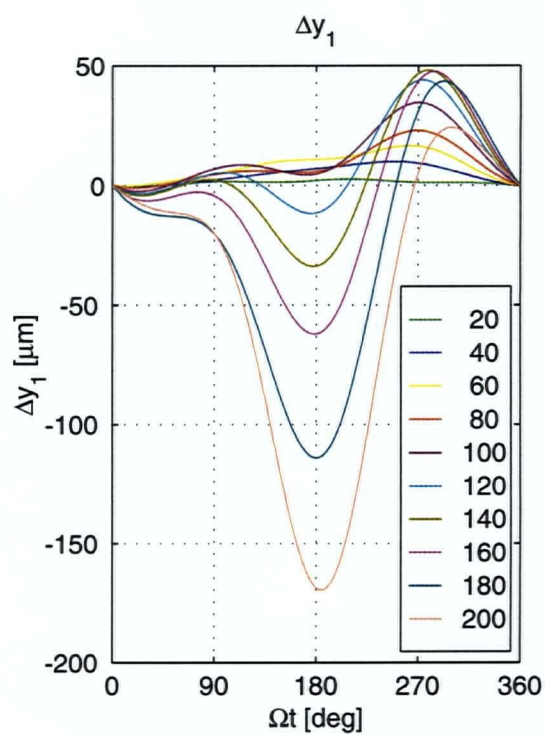
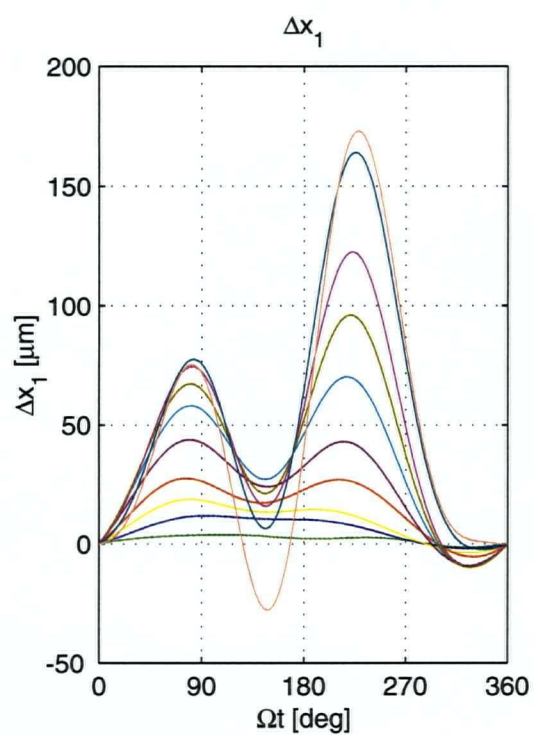
$L = 1$



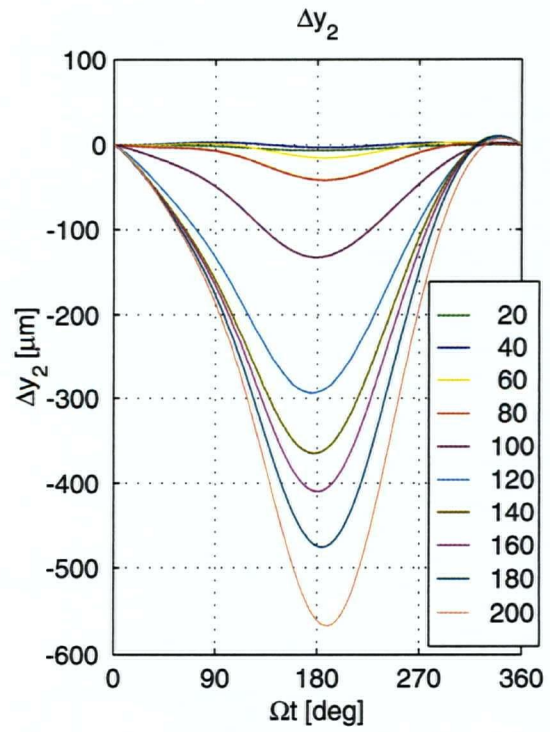
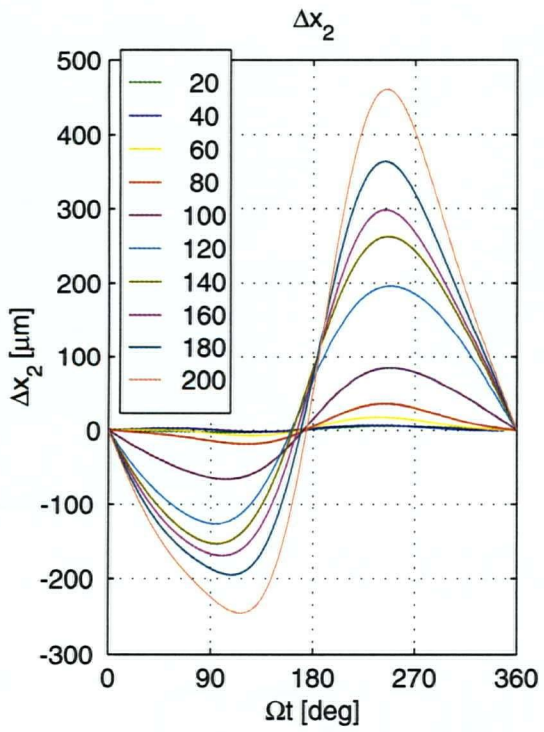
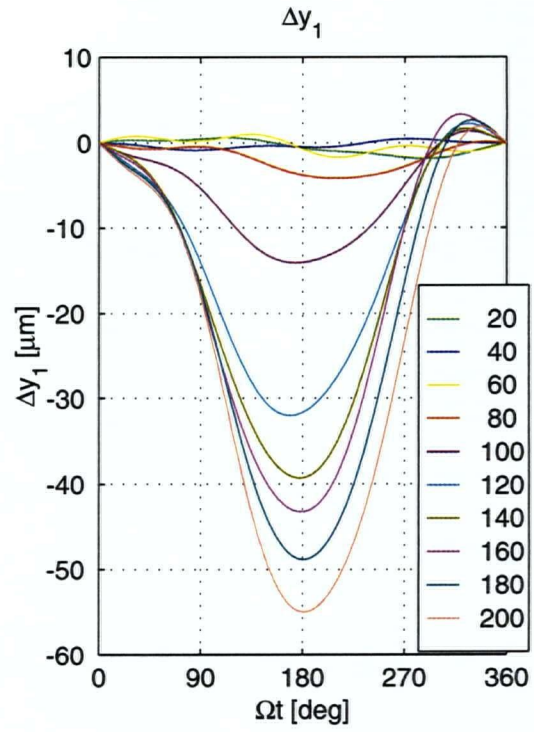
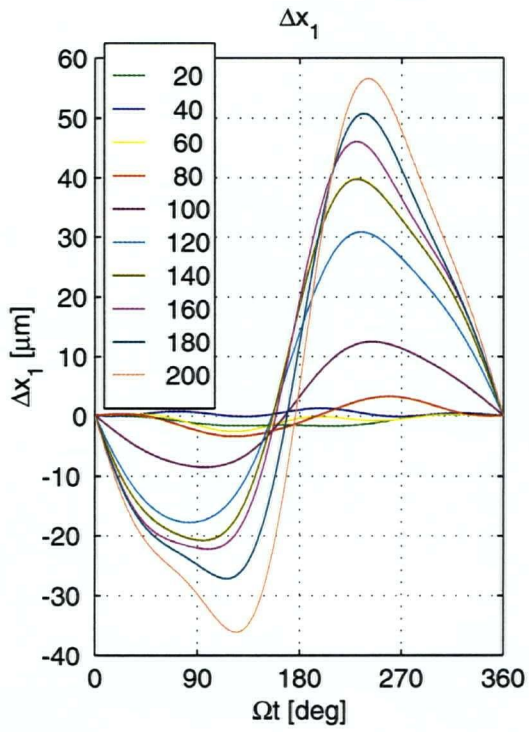
$L = 2$



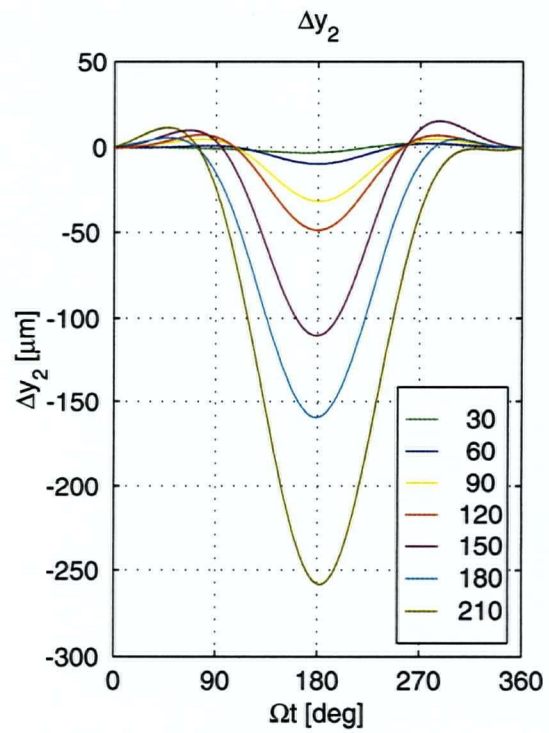
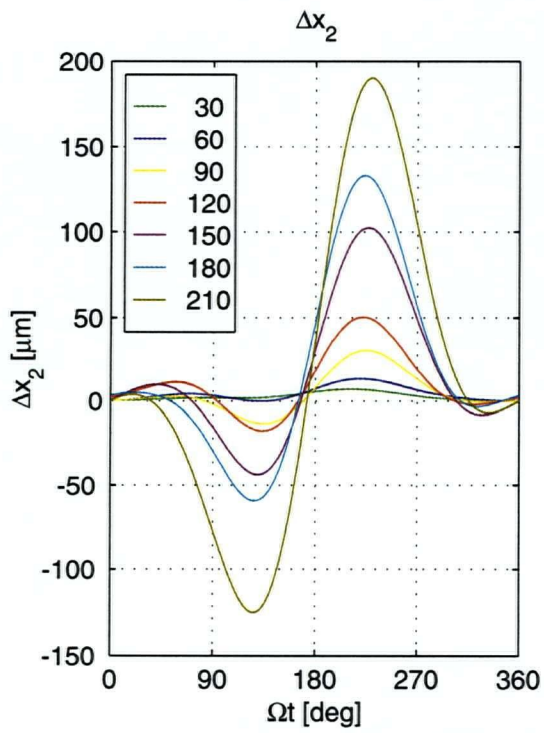
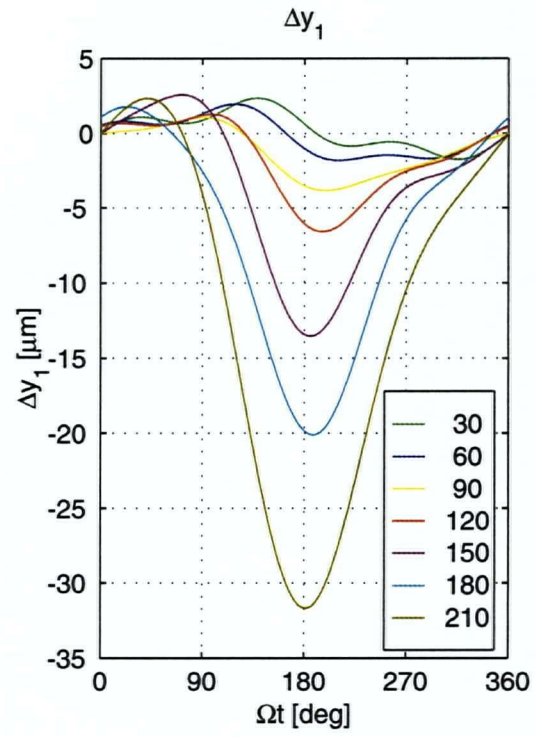
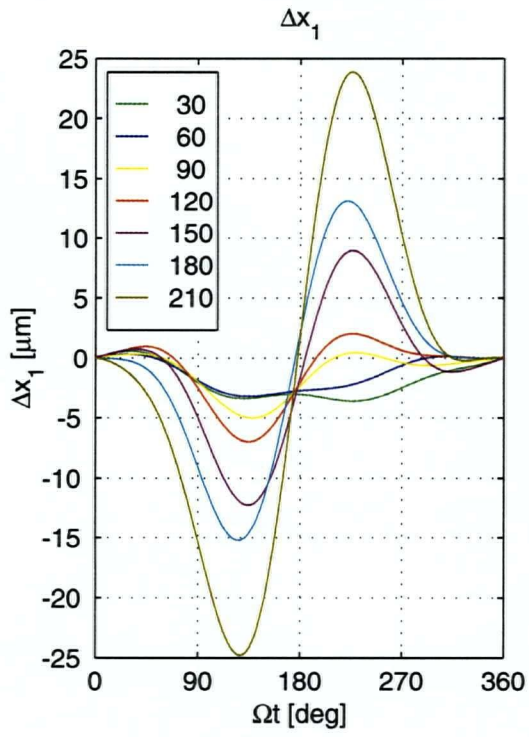
$L = 3$



$L = 4$



$L = 5$



APPENDIX C

C.1 Matlab function Powell1D

```
function [x_min,f_min,k,xHistory,fHistory] = Powell1d(fun,bounds,tol,varargin)

%
% [x_min,f_min,k,xHistory,fHistory] = Powell1d(fun,bounds,tol,p1,p2,...)
%
% Constraint minimization of a 1D function f(x) using Powell's method.
%
% Input:  fun          = function name (string)
%         bounds       = search interval [a b]
%         tol          = Convergence tolerance
%         p1,p2,...    = additional parameters to f(x) = f(x,p1,p2,...)
%
% Output: x_min        = minimum point
%         f_min        = value of f(x) at x_min
%         k            = number of iterations
%         xHistory     = convergence path of x
%         fHistory     = values of f(x) for xHistory
%
%
xHistory(1,:) = [bounds mean(bounds)];
parameters = varargin;
order = [ 0 0 0 ];

k = 1;
dx = abs(bounds(2) - bounds(1));

while dx > tol
    x = xHistory(k,:);
    for j = 1:3;
        if order(j) == 0 f(j) = feval(fun,x(j),parameters{:});
        else f(j) = fHistory(k-1,order(j)); end;
    end;
    fHistory(k,:) = f;

% Solve for parabolic coefficients
c = polyfit(x,f,2);

% Check if minimum
switch sign(c(1))
case 1 % Minimum
    x_min = -c(2)/(2*c(1));
    if x_min < x(3)
        if x_min <= x(1) x_min = mean([x(1) x(3)]); end;
        x = [ x(1) x(3) x_min ];
        order = [ 1 3 0 ];
    elseif x_min > x(3)
        if x_min >= x(2) x_min = mean([x(3) x(2)]); end;
```

```

    x = [ x(3) x(2) x_min ];
    order = [ 3 2 0 ];
else
    x = [ mean([x(1) x(3)]) mean([x(3) x(2)]) x(3)];
    order = [ 0 3 0 ];
end;

case {-1,0} % Maximum or Straight line
if f(1) <= f(2)
    x = [ x(1) x(3) mean([x(1) x(3)])];
    order = [ 1 3 0 ];
else
    x = [ x(3) x(2) mean([x(3) x(2)])];
    order = [ 3 2 0 ];
end
end

k = k+1;
xHistory(k,:) = x;
dx = abs(x(3)-x(1));
end

for j = 1:3;
    if order(j) == 0
        f(j) = feval(fun,x(j),parameters{:});
    else
        f(j) = fHistory(k-1,order(j));
    end
end

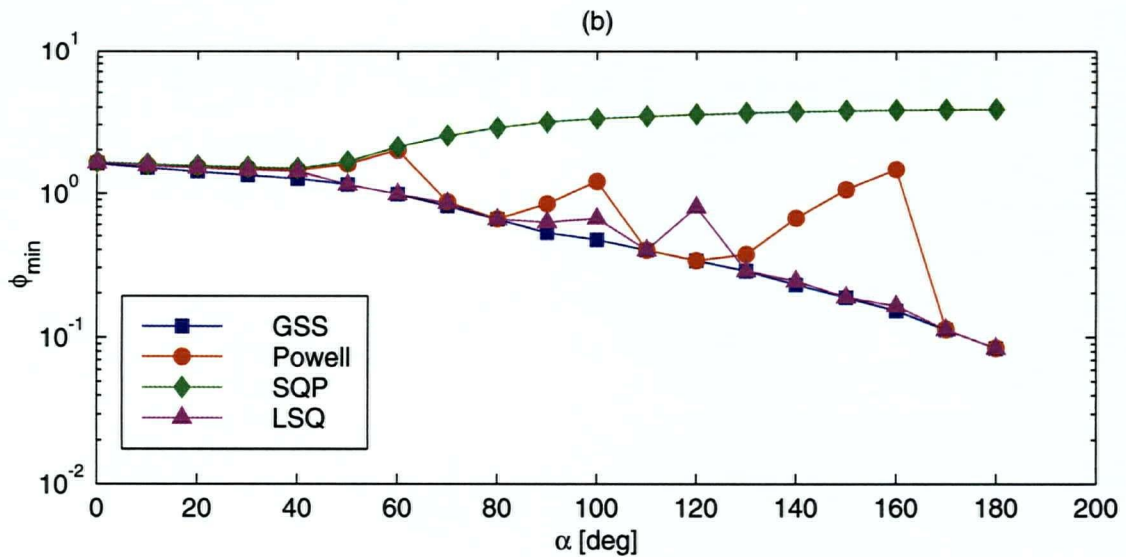
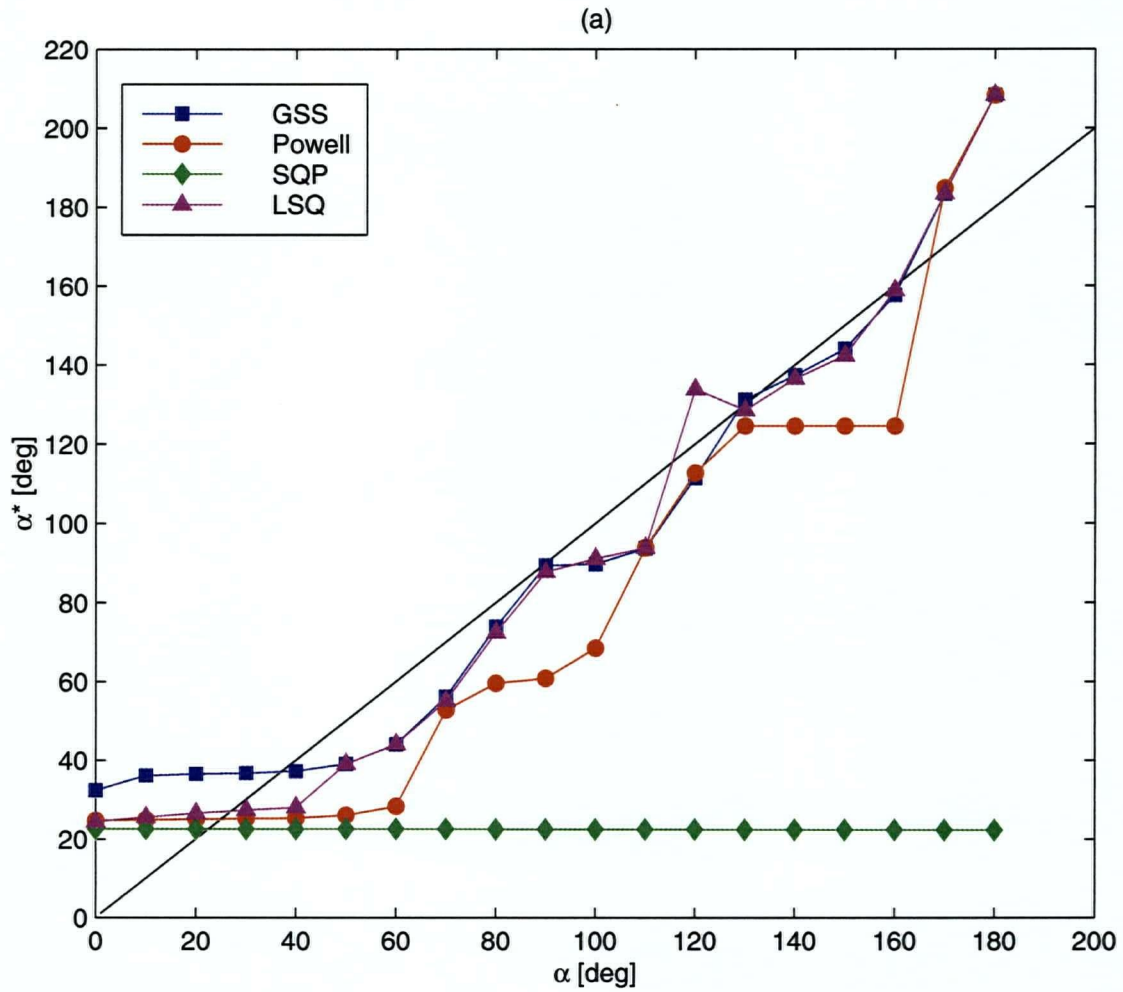
f_min = min(f);
index = find(f_min == f);
if length(index) > 1
    x_min = mean(x(index));
    f_min = feval(fun,x_min,parameters{:});
else
    x_min = x(index);
end

return;

```

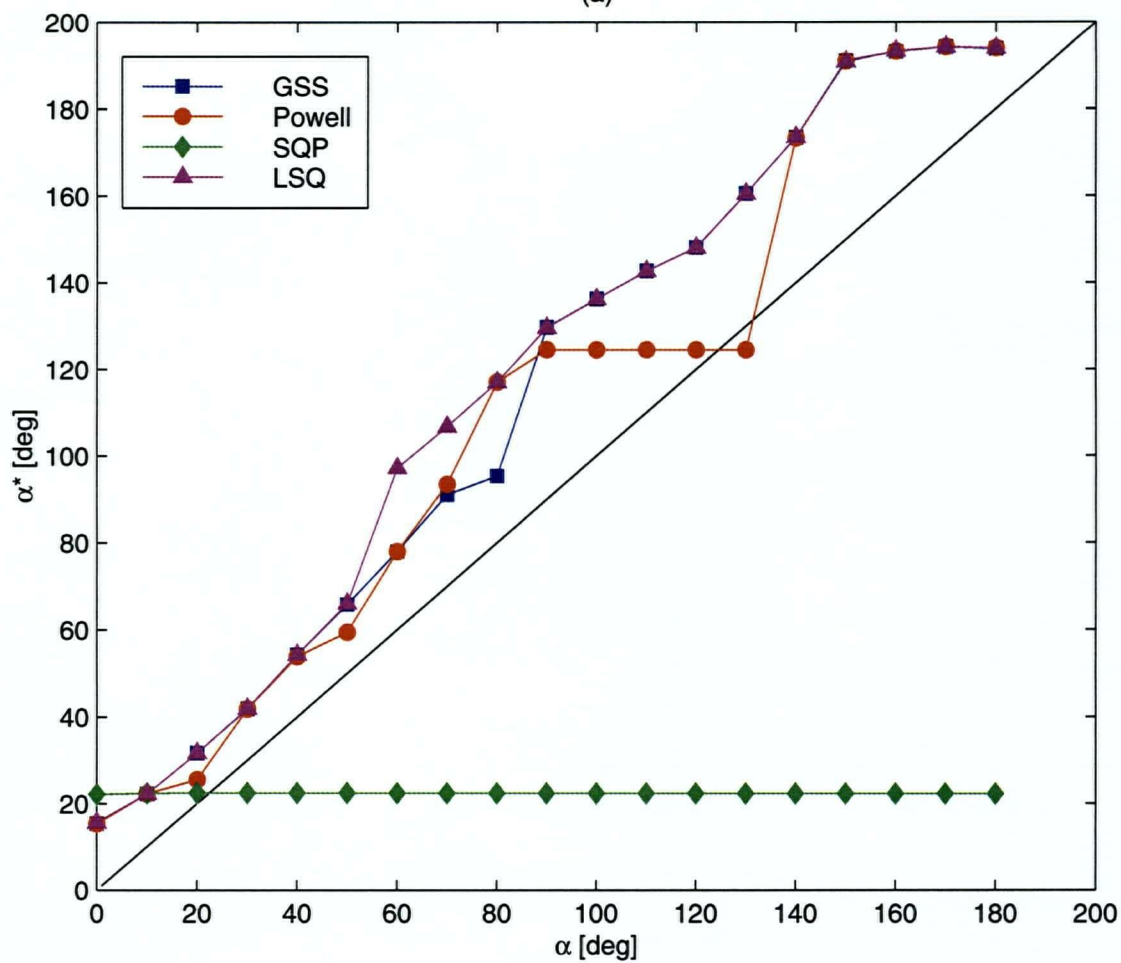
C.2 Inverse analysis results for a known crack location

$L = 1$

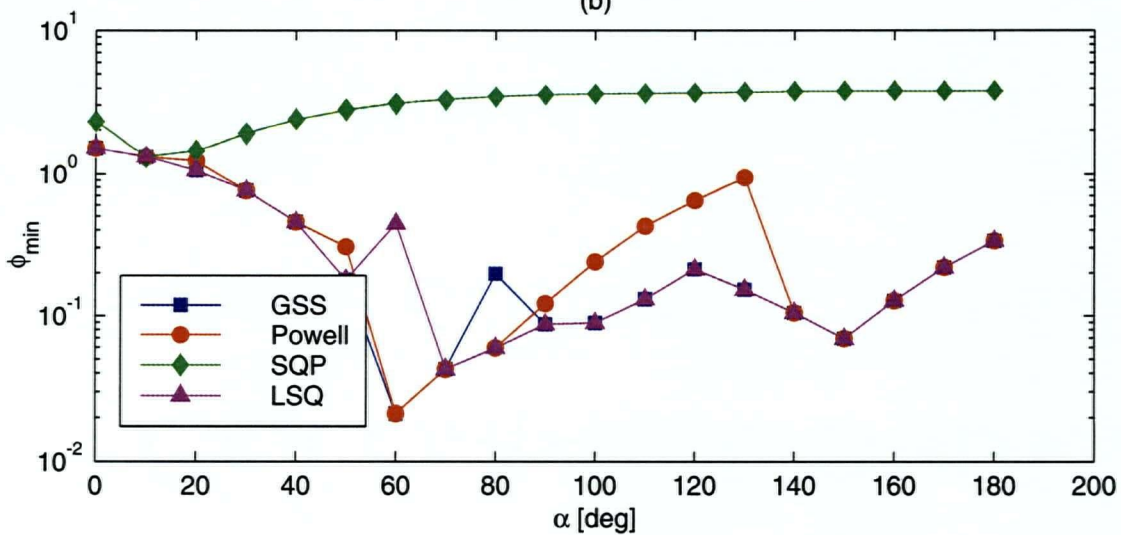


$L = 2$

(a)

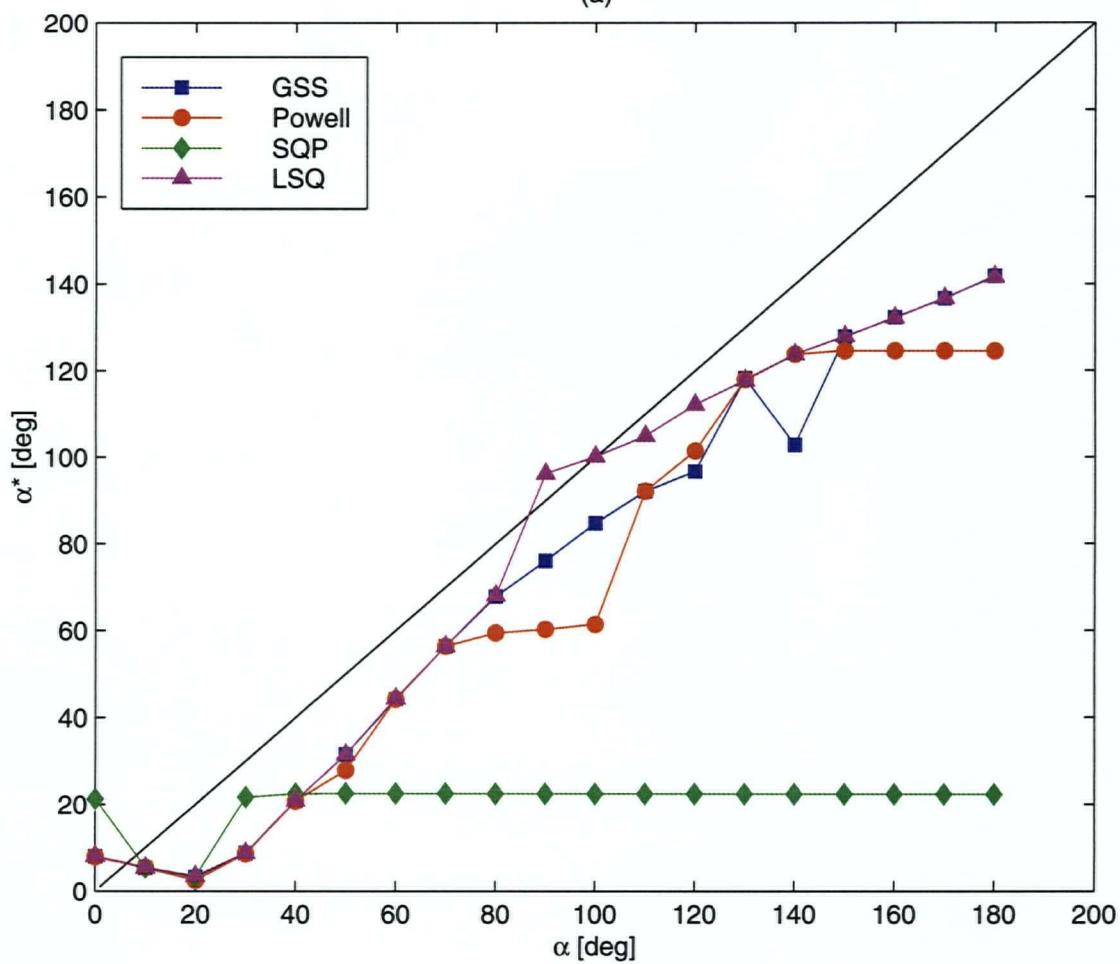


(b)

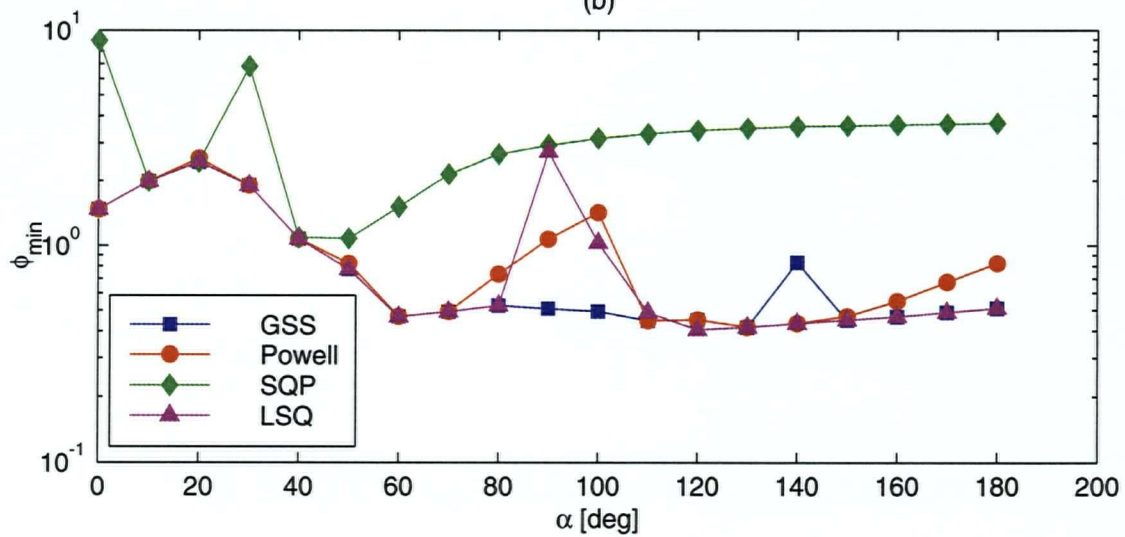


$L = 3$

(a)

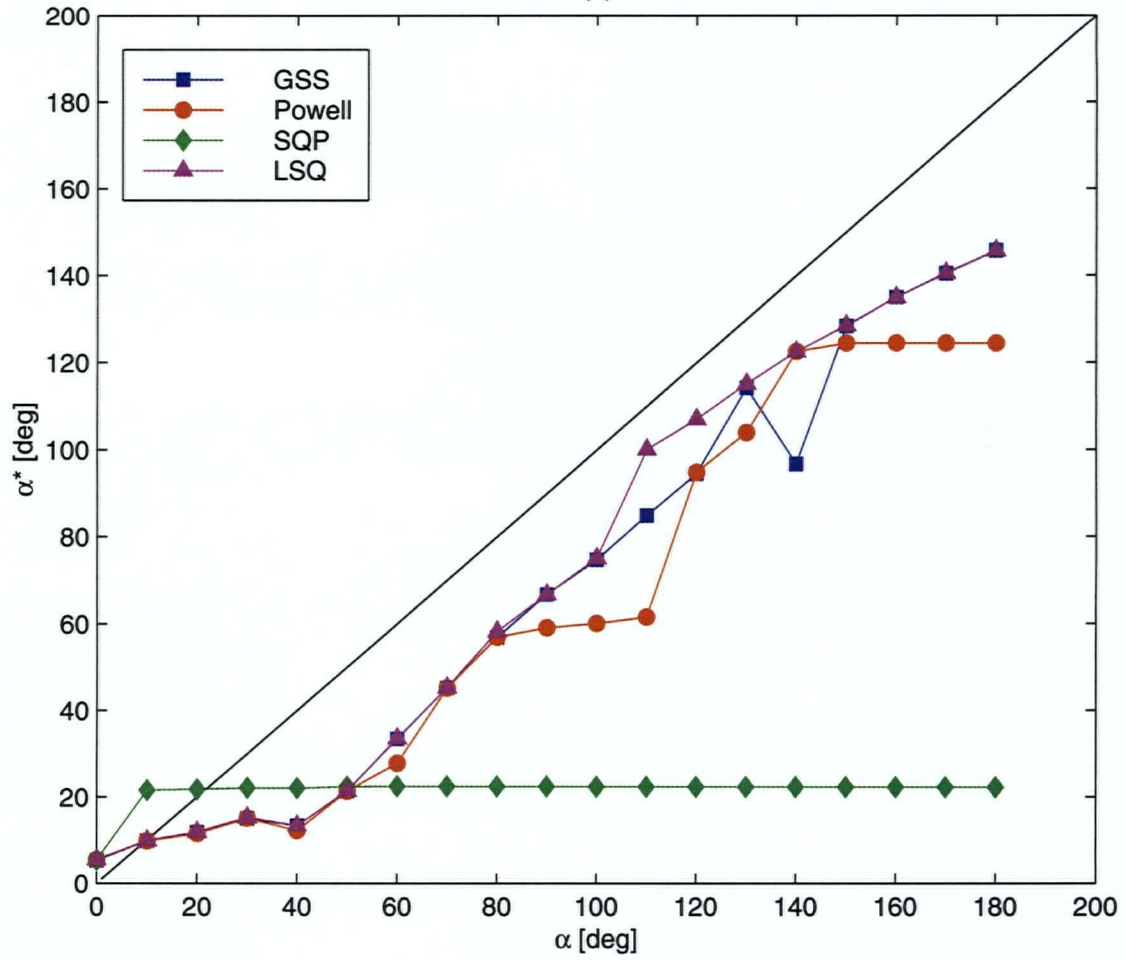


(b)

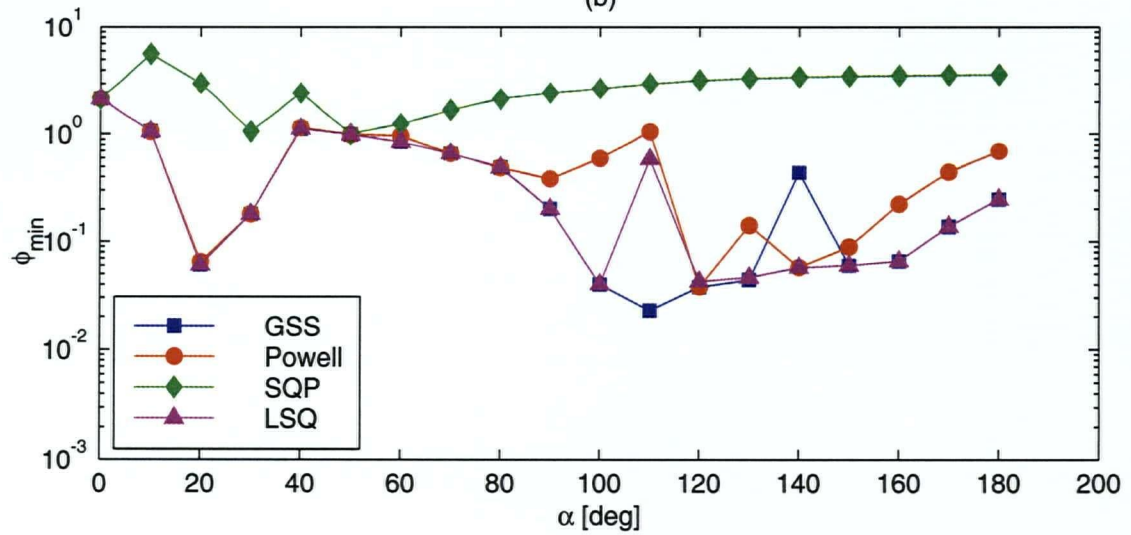


$L = 4$

(a)

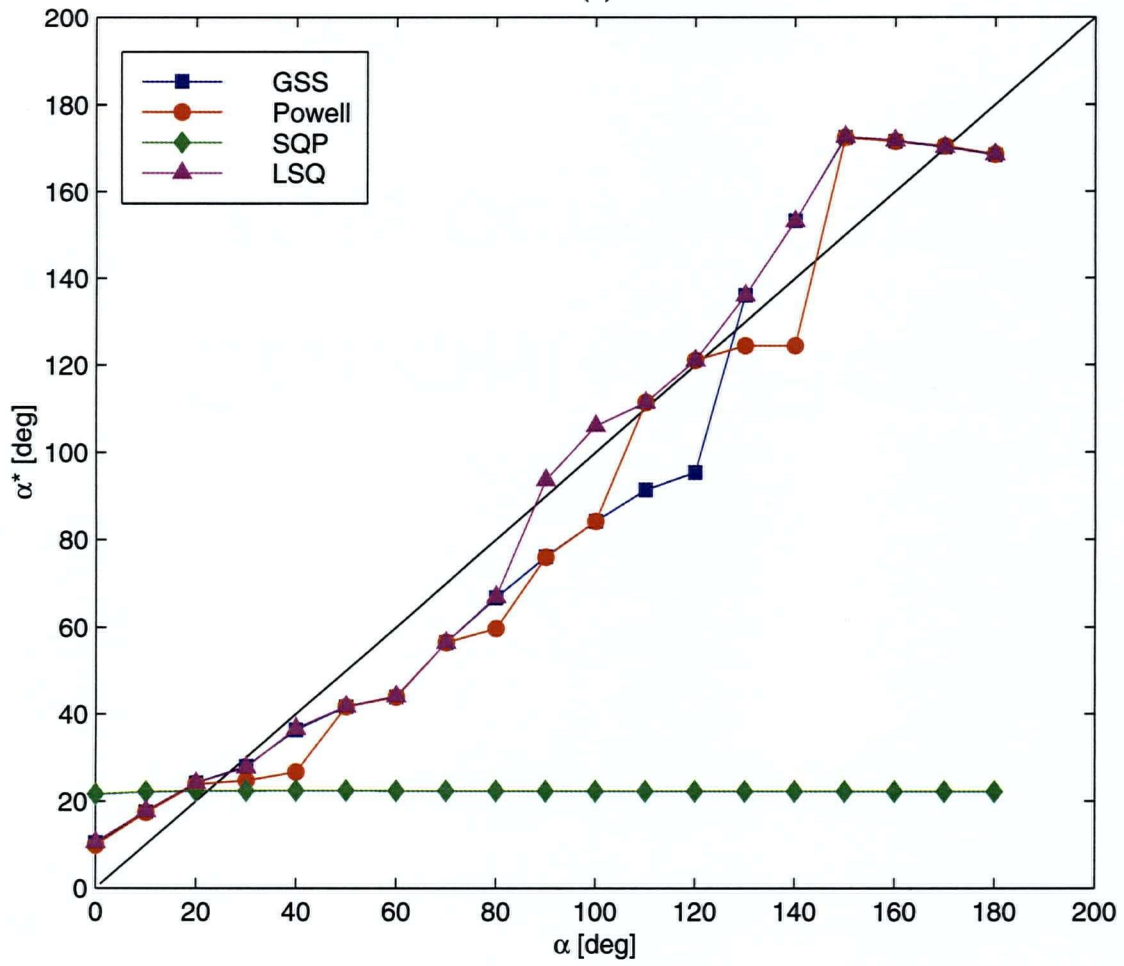


(b)

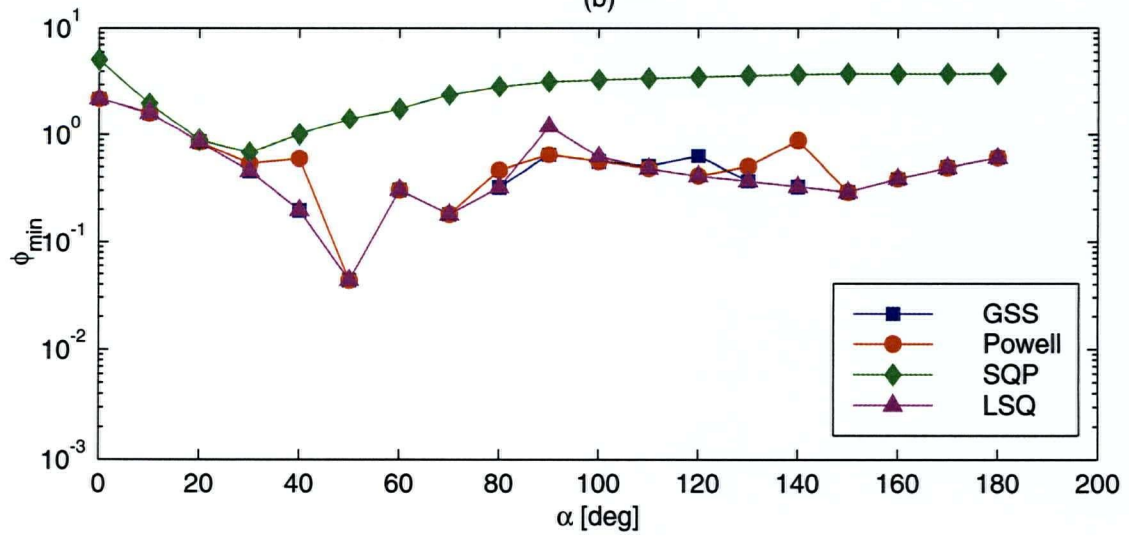


$L = 5$

(a)



(b)



C.3 Matlab function Powell2D

```

function [x_min,f_min,k,xHistory] = Powell2d(fun,bounds,tol,varargin)
%
% [x_min, f_min, k, xHistory] = Powell2d(fun,bounds,tol,p1,p2,...)
%
% Constraint minimization of a 2D function f(x), where x = [x1 x2] using
Powell's method.
%
% Input:  fun          = function name (string)
%         bounds       = search interval [a1 a2; b1 b2]
%         tol          = Convergence tolerance [tol1 tol2]
%         p1,p2,...    = additional parameters to f(x) = f(x,p1,p2,...)
%
% Output: x_min        = minimum point
%         f_min        = value of f(x) at x_min
%         k            = number of iterations
%         xHistory     = convergence path of x
%
% WARNING !!! There is no error catch programmed in this function

xHistory(1,:,1) = bounds(1,:);
xHistory(2,:,1) = [bounds(2,1) bounds(1,2)];
xHistory(3,:,1) = bounds(2,:);
xHistory(4,:,1) = [bounds(1,1) bounds(2,2)];

parameters = varargin;
k = 1;
delta = (bounds(2,:) - bounds(1,:));

while (delta>tol)*(delta>tol)'
    x = xHistory(:, :,k);

    dx = x(3,1) - x(1,1);
    dy = x(3,2) - x(1,2);

    x(5,:) = x(1,:) + [dx/2  0 ];
    x(6,:) = x(1,:) + [ dx  dy/2];
    x(7,:) = x(1,:) + [dx/2  dy ];
    x(8,:) = x(1,:) + [ 0  dy/2];
    x(9,:) = x(1,:) + [dx/2  dy/2];
    x(10,:) = x(1,:) + [dx/4  dy/4];
    x(11,:) = x(1,:) + [3/4*dx  dy/4];
    x(12,:) = x(1,:) + [3/4*dx  3/4*dy];
    x(13,:) = x(1,:) + [dx/4  3/4*dy];

    for j = 1:13
        X(j,:) = [ x(j,1)^2 x(j,2)^2 x(j,1)*x(j,2) x(j,1) x(j,2) 1 ];
        f(j,1) = feval(fun,x(j,:),parameters{:});
    end

    c = X \ f;

```

```

M = [ 2*c(1)  c(3)
      c(3)  2*c(2) ];

x_min = M \ (-c(4:5));

if x_min(1) < x(9,1)  x([2 3],1) = x([11 12],1);
elseif x_min(1) > x(9,1)  x([1 4],1) = x([10 13],1);
else  x(1:4,1) = x(10:13,1);  end;

if x_min(2) < x(9,2)  x([3 4],2) = x([12 13],2);
elseif x_min(2) > x(9,2)  x([1 2],2) = x([10 11],2);
else  x(1:4,2) = x(10:13,2);  end;

k = k+1;

xHistory(:, :, k) = x(1:4, :);
delta = x(3, :) - x(1, :);
end

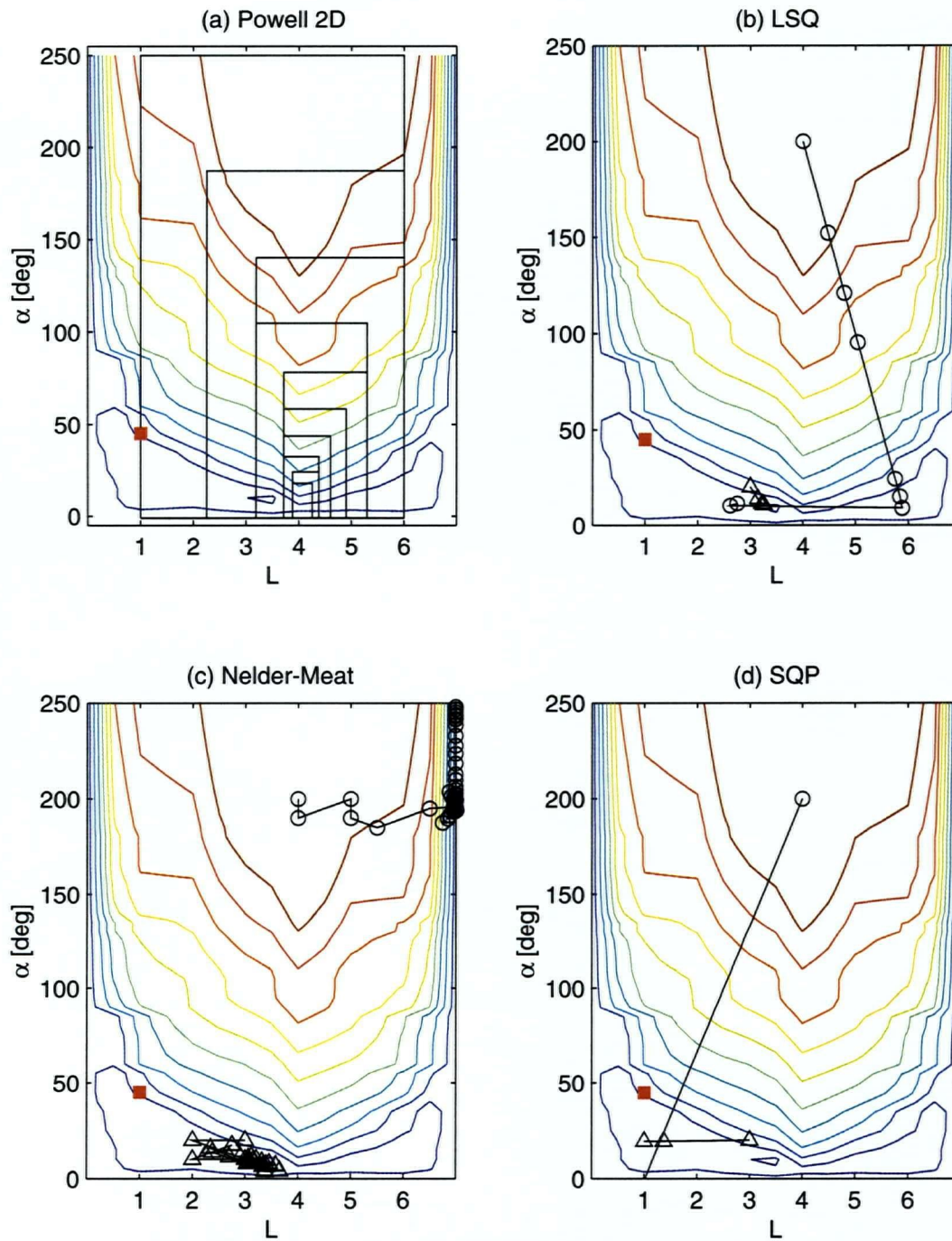
x_min = x_min.';
f_min = feval(fun, x_min, parameters{:});

return;

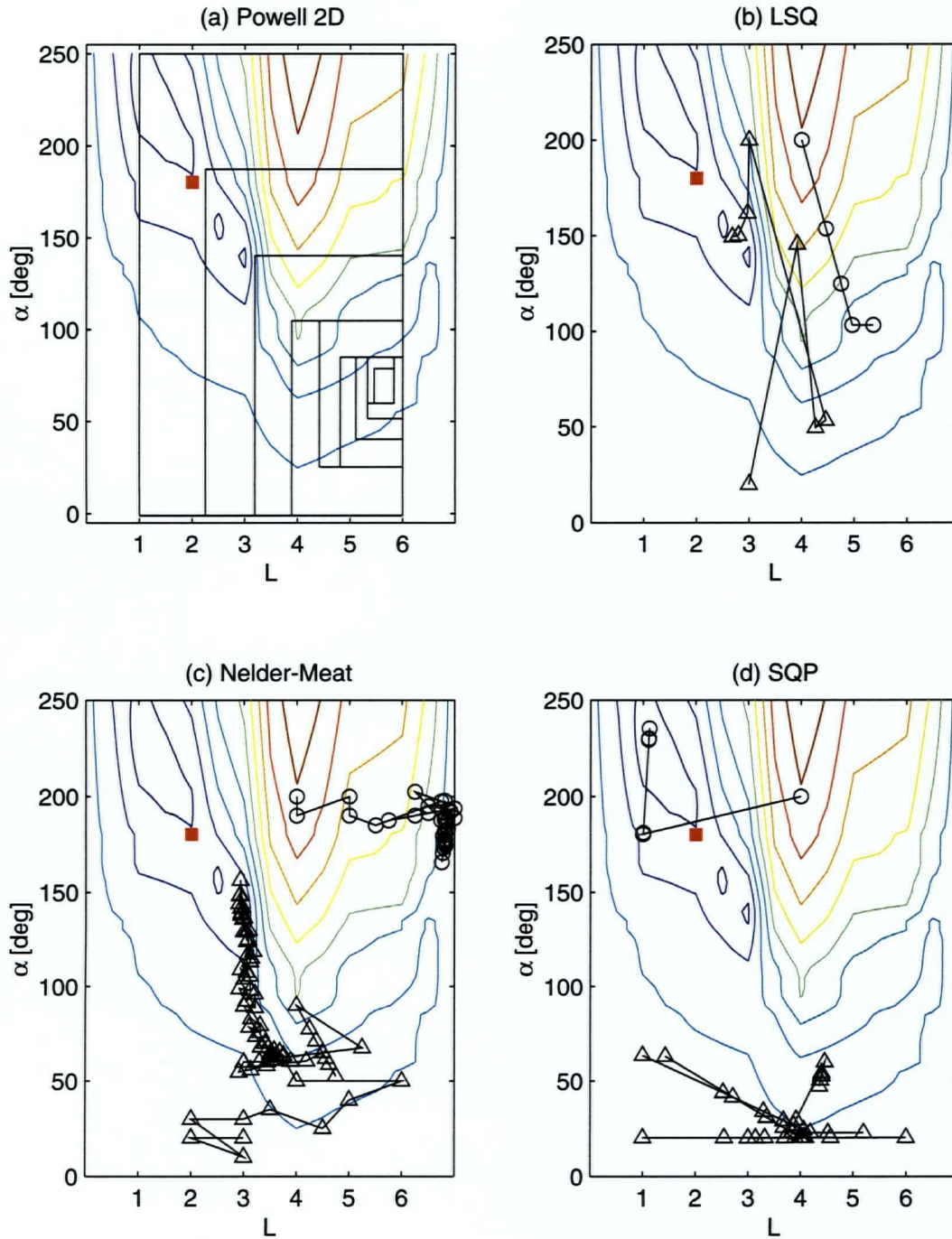
```

C.4 Multi-variable inverse analysis results

$$\alpha_{\text{true}} = 45^\circ, L_{\text{true}} = 1$$



$$\alpha_{\text{true}} = 180^\circ, L_{\text{true}} = 2$$



$$\alpha_{\text{true}} = 90^\circ, L_{\text{true}} = 4$$

